Stony Brook University

Imprinted Effects in The Brain: From The X Chromosome to Single Autosomal Loci

A Dissertation Presented

by

Eric Szelenyi

to

The Graduate School

In Partial Fulfillment of the

Requirements

for the Degree of

Doctor of Philosophy

in

Neuroscience

Stony Brook University

May 2017

Stony Brook University

The Graduate School

Eric Szelenyi

We, the dissertation committee for the above candidate for the
Doctor of Philosophy degree, hereby recommend
acceptance of this dissertation.

Pavel Osten, MD, PhD – Dissertation Advisor
Associate Professor
Cold Spring Harbor Laboratory

Josh Z Huang, PhD – Chairperson of Defense
Professor
Cold Spring Harbor Laboratory

Bo Li, PhD – Dissertation Committee Member
Associate Professor
Cold Spring Harbor Laboratory

David Talmage, PhD –Dissertation Committee Member
Professor
Department of Neurobiology and Behavior,
Stony Brook University

Cristina Alberini, PhD – Outside Dissertation Committee Member
Professor
Center for Neural Science
New York University

This dissertation is accepted by the Graduate School

Charles Taber
Dean of the Graduate School

Abstract of the Dissertation

Imprinted Effects in The Brain: From The X Chromosome to Single Autosomal Loci

by

Eric Szelenyi

Doctor of Philosophy

in

Neuroscience

Stony Brook University

2017

Proper brain functioning relies on “imprints” – epigenetic marks controlling gene expression in a parent-of-origin (PO)-specific manner. Early in development imprinting occurs upon the X-chromosome in females, and also in both sexes amongst ~100 known imprinted genes, such as *Growth factor receptor-binding protein 10* (*Grb10*). Uniquely, the control over gene dosage endowed by both forms of imprinting (X-chromosome inactivation, XCI, and genomic imprinting, respectively) outweighs the benefits of diploidy. Thus, their existence highlights a functional significance. Spatial arrangements of imprinted brain cells have implicated systems and circuit-level functions over behavior. However, until now we have lacked the means for adequate spatial analysis required to link imprinted brain patterns to specific behavioral functions. My dissertation targets this problem using advanced whole-brain microscopy and computational methods in combination with novel mouse genetics and behavior. Through these approaches, my dissertation provides results that 1) define XCI brain pattern dynamics in female mice, 2) determine its behavioral influence in an X-linked brain disease model, and 3) identify novel behavioral brain circuitry affiliated with the cellular imprint status of *Grb10*.

To determine whole-brain XCI dynamics, I quantified active X-chromosome (XCa) cell density on maternal (Xm) or paternal (Xp) XCa-GFP reporting mice. Whole-brain quantifications

revealed a modest but statistically significant ~10% maternal XCa bias amongst all brain areas. The overall individual variability observed in whole-brain XCI ratios, ranging as wide as 25%/75%, was found to strongly predict skewing across brain areas, suggesting brain XC imprinting occurs prior to differentiation of the neural germ layer. Together, these results suggested an Xm favoring of inherited X-linked behavioral traits and disease penetrance. To test this hypothesis, I examined behaviors of heterozygous fragile X syndrome (FXS) model mice. Disease penetrance was observed only in maternal FXS mice, which phenocopied the human female FXS symptoms of exploratory alterations, spatial memory deficits, and social avoidance accompanied with hyperarousal. To identify putative neural circuit correlates of the disrupted behaviors I used correlational analyses amongst healthy XCa cell density and behavioral scores across 740 brain regions. First, time of center exploration in an open field positively correlated with an integrated sensorimotor and arousal network of connected regions. Second, altered social exploration in a 3-chamber test negatively correlated to interconnected regions outlining a socio-spatial encoding network. Collectively, these results described the dynamics of brain XCI and its relationship to behavioral function in an X-linked disease state.

In the second part of my dissertation I examined the brain-wide distribution of *Grb10*'s imprint status with respect to systems of behavior. I generated non-gene disruptive allelic-reporter/Cre mouse lines that allowed me to map, trace, and manipulate the activity of neurons expressing *Grb10* maternal or paternal alleles. Dual color-assisted, PO-specific expression mapping in double transgenic mice revealed predominant and diffuse monoallelic paternal expression in subcortical stress centers and monoallelic maternal expression within non-neuronal cells of the vasculature. Novel biallelic neuronal populations were found in defensive subcortical nodes, including the ventrolateral PAG (vlPAG). The vlPAG biallelic population contained a mix of novel ovBNST-projecting VIP+ and midline thalamus and amygdala-projecting GAD2+ neurons. Acute (inhibitory DREADD) or chronic (Cre-dependent ablation) loss-of-function manipulations of these cells suggested a suppressive role in fear memory-specific freezing behavior. These results demonstrated brain system-specific roles of each *Grb10* allele in behavioral function.

In summary, my dissertation broadens the behavioral relevance of XC and gene-specific imprinting in providing novel systems-level regulation over behavior.

Dedicated to Dominick Stanisci

Table of Contents

List of figures

List of tables

"Imagination is more important than knowledge. Knowledge is limited. Imagination encircles the world"

-Albert Einstein

Acknowledgments

I am very grateful for the relationships formed through graduate school and in my scientific pursuits in general over the last 10 years. As they say, everything has its plan, and I have learned quite a lot that goes beyond the bench and textbooks. Many of these relationships, for the sake of scientific writing, can be classified into categories of purpose. In the fun category I want to acknowledge friends Matt Gardner, Dane Buenten, Rob Bronstein, and Jean Albrengues. In the ever-important supportive role category are Ramesh Palaniswamy, Yongsoo Kim, Tanvir Khan, Steve Shea, Jessica Tollkuhn, and Hillary Schiff. In the patience-lending and nurturing role category are Lauren Stephenson, Ralph Szelenyi, Diane Wimmer, Dominick Stanisci, and most importantly Catalina Lasso. Finally, I would like to thank my advisor, Pavel, for crafting my scientific eye and giving me the opportunity to complete the work that I have achieved in this thesis and beyond – let's put our flag on it.

Eric Szelenyi
194 Schaefer St, 1A, Brooklyn, NY 11207
(617) 840-1330 · eszeleny@cshl.edu

Education

Doctor of Philosophy (Ph.D.) in Neuroscience *May 17*
Department of Neurobiology and Behavior, Stony Brook University, Stony Brook, NY
Thesis Advisor: Pavel Osten, Cold Spring Harbor Laboratory

Bachelor of Arts; Major – Psychology, Minor – Biochemistry *May 06*
Shippensburg University, Shippensburg, PA

Honors/Awards

AAAS/Science Program for Excellence in Science, August 2014-2016
President's Award for Excellence in Teaching by a Graduate Student, Stony Brook University, May 2014
Special Act Award, United States Army Research of Environmental Medicine, 2010
Dean's List, Shippensburg University, spring 2002, fall 2003, spring 2004, fall 2004, spring 2005
Certificate of Student Research Achievement, Shippensburg University, 2003-2004, 2004-2005, 2005-2006

Professional Affiliations

The Society for Neuroscience
The New York Academy of Sciences
Psi Chi, National Honors Society in Psychology

Publications

Szelenyi ER, Matzko M, Barnes BR, Motch SM, Kremser J, Stout T, Blizard D, McCarter R, Hymer WC (2015) Short-term caloric restriction does not enhance spatial memory and has differential effects on the ghrelin-responsive growth hormone in hippocampus and pituitary gland. In-preparation.

Szelenyi ER and Urso ML (2012) Time-course analysis of injured skeletal muscle suggests a critical involvement of ERK1/2 signaling in the acute inflammatory response. Muscle & Nerve 45(4):552-61. (PMID: 22431089)

Urso ML, **Szelenyi ER**, Warren GL, Barnes BR (2010) Matrix Metalloprotease-3 and Tissue Inhibitor of Metalloprotease-1 mRNA and Protein Levels Are Altered in Response to Traumatic Skeletal Muscle Injury. European Journal of Applied Physiology 109(5):963-72. (PMID: 20349081)

Barnes BR, **Szelenyi ER**, Warren GL, Urso ML. Alterations in mRNA and Protein Levels of Metalloproteinases-2, -9 and 14 and Tissue Inhibitor of Metalloproteinase-2 post-Traumatic Skeletal Muscle Injury. Am J Physiol Cell Physiol, 2009 Dec; 297(6):C1501-8. (PMID:19794148)

Abstracts/Posters

Szelenyi E, Kim Y, Venkataraju KU, Pradhan K, Osten P. Quantification of whole-brain X-chromosome inactivation in healthy and X-linked disease states. Federation of European Neuroscience Societies Meeting, July 2016, Copenhagen, Denmark.

Szelenyi E, Palaniswamy R, Schiff H, Tucciarone J, Huang J, Li B, Osten P. Biallelic expression mapping of the imprinted Grb10 locus reveals novel fear-suppressive neurons in the periaqueductal gray. Society for Neuroscience Meeting, Oct 2015, Chicago, IL

Szelenyi E, Palaniswamy R, Schiff H, Osten P. Maternal *Grb10* Expression Defines a Novel Subpopulation of Periaqueductal Grey Neurons That Gate Fear Memory. Wiring the Brain Meeting, March 2015, Cold Spring Harbor, NY

Szelenyi ER, Palaniswamy R, Osten P. A Novel Genetic-based Strategy for Investigating Neural Circuits Defined by the Imprinted *Grb10* locus. Symposium in Neuroscience, September 2013, Stony Brook, NY

Szelenyi ER, Warren GL, Urso ML. Innate resolution of traumatic injury-induced skeletal muscle inflammation is initiated within 24 hours and involves MKP-1 induction, Hsf-1 disinhibition, and Hsp27 expression. Experimental Biology (EB) Meeting, May 2010, Anaheim, CA

Szelenyi ER, Barnes BR, Urso ML. Traumatic Skeletal Muscle Injury Activates the Erk1/2 Pathway and Down-Regulates Atrogene Transcription. Tissue Repair and Regeneration Gordon Research Conference, June and "Benchtop to Battlefield" Poster Symposium, July 2009, Natick, MA

Barnes BR, **Szelenyi ER**, Warren GL, FACSM, Urso ML. Traumatic Skeletal Muscle Injury Results in Dual Regulation of Myostatin through Binding Protein Inhibition and Diminished Expression. American College of Sports Medicine Meeting, May 2009, Seattle, WA

Matzko ME, Stout JT, Barnes BR, **Szelenyi ER,** Hymer WC, Motch SM, and McCarter RJ. Ghrelin as a Metabolic Signal of Caloric Restriction in Aging? XIXth IAGG World Congress of Gerontology and Geriatrics Meeting, July 2009, Paris, France

Urso ML, Barnes BR, **Szelenyi ER**, Nicholson RO, and Zambraski EJ. Utilization of Military-Relevant Muscle Injury Models to Identify Pharmacological Treatment Strategies. Army Science Conference (ASC), Dec 2008, Orlando, FL

Szelenyi ER, Urso ML, Nicholson RO, Barnes BR. Characterization of MMP-3 & TIMP-1 Protein Expression in Response to Skeletal Muscle Injury in Mice. Integrative Biology of Exercise IV Meeting, October 2008, Hilton Head, SC

Szelenyi ER, Haslach ER, Martey-Ochola CA. The effects of cigarette smoking on inducible nitric oxide synthase in normal human lung fibroblasts. American Chemical Society (ACS) Meeting & Exposition, March 2006, Atlanta, GA

Haslach EM, **Szelenyi ER**, Richardson JN, and Martey-Ochola CA. Analysis of Nitrite Using an Attenuated Total Reflectance Spectroelectrochemical Flow Cell. American Chemical Society (ACS) Meeting & Exposition, March 2006, Atlanta, GA

Haase S, Fisk G, **Szelenyi E**R, and Harkins J. Letter Detection and Identification: Conscious versus Unconscious Perception. Psychonomic Society Meeting, November 2005, Toronto, ON

Szelenyi E, Divito C, Dougherty D, Hubbard J, and Hale RL. Vagal Tone in Binge Drinking College Students. Eastern Psychological Association (EPA) Meeting, March 2004, Boston, MA

Greener S, **Szelenyi E**, Kessler J, and Hale RL. Vagal Tone in Binge Drinking College Students. EPA Meeting, March 2003, Washington, D.C.

Teaching/Supervisory Experience

LearningRX, Jericho, NY *Dec 13 – Aug 15*
Cognitive Skills Trainer
• Worked one on one with students to improve cognitive abilities through cognitive task administration while providing motivational support
• Completed 6-month training programs for three students: a 12 year old with learning/behavioral disabilities (ADHD, autism), a 14 year old looking to improve cognitive processing, and a 9 year old with minor learning disability.

Cold Spring Harbor Laboratory, Cold Spring Harbor, NY *July 12 – Present*
PhD Candidate in Neuroscience
•Supervised and trained Programs for the Future high school student Jonah Wu in molecular biology and cell culture (Jul 2016 – Present)
•Supervised and trained undergraduate Danielle Fisenne in mouse surgery and behavioral assays (Jul 2016 – Present)
•Supervised and trained visiting German Master's student in various molecular biology techniques and experimental design (Aug 2013 – July 2014)
• Trained rotating graduate student Alice Change in various molecular biology techniques (Nov 2012 – Feb 2013)
•Supervised and trained high school student Heather Schwartz in molecular cloning and DNA transfections in mammalian cell lines (Sep 2012 – May 2013)

Stony Brook University, Department of Neurobiology and Behavior, Stony Brook, NY *Sep 11 - Dec 11*
Teaching Assistant
• Instructed Animal Physiology laboratory class, composed of 30 pre-medicine undergraduate students weekly
• Taught lessons for laboratory session prior to the student's experiments
• Designed and conducted weekly quizzes

• Provided office hours allowing for feedback and in-depth discussions of key concepts in neurophysiology and biophysics
• Graded all laboratory reports and quizzes and provided feedback and assistance

Stony Brook University, Department of Neurobiology and Behavior, Stony Brook, NY *Jan 11 – May 11*
Teaching Assistant
• Instructed "Fundamentals of Scientific Inquiry in the Biological Sciences II" laboratory class, consisting of 30 biology
undergraduate students weekly for four hours
• Provided lessons for laboratory session prior to the student's experiments
• Conducted weekly quizzes
• Held weekly office hours allowing for feedback and in-depth discussions of key concepts in biological sciences (e.g. comparative anatomy, DNA, photosynthesis)
• Graded all laboratory reports and quizzes and provided feedback and assistance

Chapter I: Introduction: X-chromosome inactivation (XCI) and genomic imprinting in brain function

Mammalian traits are often thought to follow Mendelian's laws of inheritance: one copy of each gene is passed to offspring with gene to phenotype traits being shared amongst parents. For the most part, this is true: 99-99.9% of mammalian genes follow this trend (Butler, 2002). However, non-Mendellian forms of inheritance do exist and have evolved to shape biological functions that overshadow the benefits of diploidy. Two deviations from Mendelian inheritance – X-chromosome inactivation (XCI) and genomic imprinting – share a proposed common function of gene dosage regulation. Both phenomena are classified as "imprinting", in that epigenetic modifications mark, or "imprint", DNA to control gene expression. XCI is a proposed mechanism normalizing female (XX) sex chromosome transcriptional output by randomly silencing one X as compensation for male (XY) sex chromosome hemizygosity. The end result is mosaic patterns of active XC (XCa) choice in all cells of somatic tissue. Parent-of-origin (PO)-specific patterns of expression amongst ~150 genes on autosomal chromosomes in both sexes is accomplished separately through genomic imprinting, which results in allele silencing based on PO. This can occur in different configurations (i.e. paternal allele silenced in cell A, maternal active in cell B) across imprinted

loci with gene dosage adjustments controlling aspects of both growth and behavior (Wilkinson et al., 2007).

Many normal behavioral functions are dependent on imprinting (Davies, 2010). In XCI, spatial brain mosaic of XCa is proposed to affect broad and variable phenotypes seen in female X-linked disorders (Lee and Bartolomei, 2013). In genomic imprinting, stereotyped spatial expression patterning that outlines brain systems may indicate circuit level-based regulation of different typically innate behaviors (Wilkinson et al., 2007). My dissertation focuses on both forms of non-Mendelian inheritance, XCI and genomic imprinting on autosomal chromosomes, with a particular focus on the study of imprinted gene expression in the brain and its relevance for behaviors. In this chapter I present the relevant background for the developmental mechanisms of each form of imprinting. This introductory material is supplemented with brain imprinting-specific background, providing context for the specific aims of experiments listed in chapters 2, 3, and 4.

1. The process of XCI

Female mosaicism of paternal (Xp) and maternal (Xm) XCa cells is a result of orchestrated, epigenetic steps occurring in early embryogenesis (Figure1). Mouse studies have provided most of what is known about this process due to the genetic accessibility and ease of genetic manipulations in the mouse as an animal model. In humans, random XCI occurs but imprinted XCI remains controversial (Lee and Bartolomei, 2013). The first step of female XCI

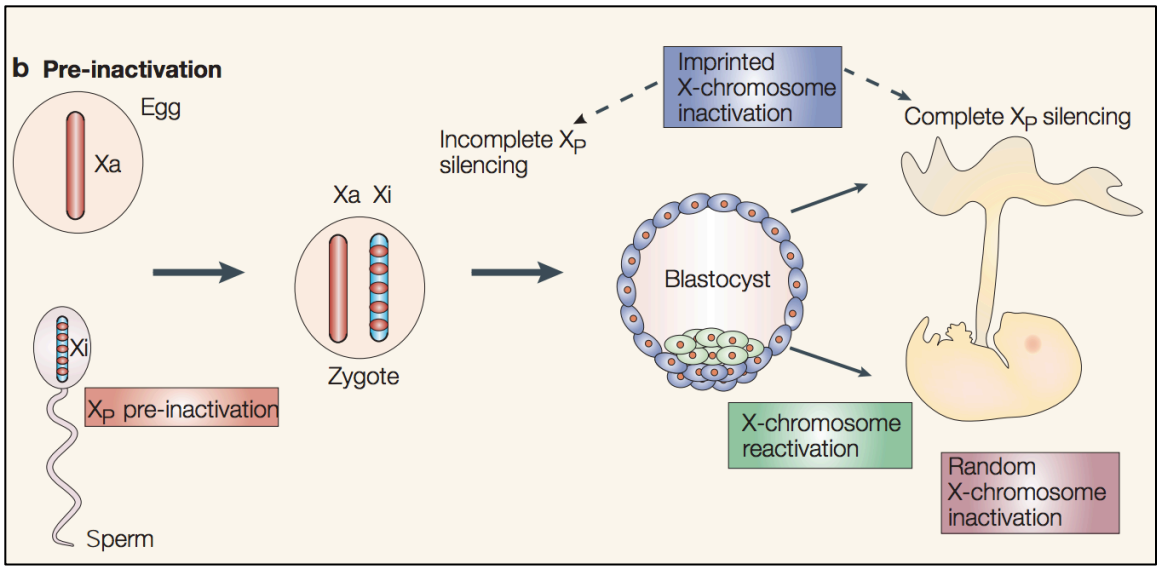

Figure 1. Xp-guided XCI (adopted from Huynh et al, 2005). In a simplified version of events, the XC in the father's germline is inactive due to MSCI. In the female zygote, partial inactivation progresses from repetitive element silencing to genic and then full Xp silencing in preimplantation development. Leftover chromatin marks from MSCI is thought to orchestrate this progression in the early embryo. All extraembryonic tissue retains the inactive Xp after implantation whereas reactivation of Xp followed by random XCI occurs in the inner cell mass and epiblast, respectively.

regulation begins in the father's germ line. X and Y chromosomes in sperm cells undergo "meiotic sex chromosome inactivation" (MSCI) during prophase of spermatogenesis. This state renders 85% of genes on the X transcriptionally inactive after the completion of meiosis (Namekawa et al., 2006). When zygotic gene activation commences at the 2-cell stage in female embryos, repetitive elements on the Xp are inactive and this is assumed to be marks left over from MSCI. This minor modification progresses into genic and eventually Xp chromosomal silencing (called imprinted XCI) over the course of embryonic preimplantation development (Namekawa et al., 2006; Namekawa et al., 2010). Maternal XC protection against preimplantation silencing has also been proposed to play a role in Xp-specific imprinted XCI. From this view, *Xist*, a long non-

coding RNA (lncRNA) responsible for coordination of epigenetic XC silencing in *cis*, is maternally imprinted in the zygote and therefore skews choice towards Xp (Tada et al., 2000). Therefore, pre-fertilization biases established in the male and female germ lines could both be responsible for imprinted XCI of Xp (Huynh and Lee, 2003). Once the embryo implants, tissue divergence occurs amongst XC silencing. Specifically, all extraembryonic tissue, consisting of the primitive endoderm and trophectoderm, keeps the Xp inactive, whereas the epiblast lineages reactivate Xp. Shortly after the reactivation at E4-5.5 (Okamoto et al., 2004) and around the time of gastrulation at E6.5 (Kojima et al., 2014), the cells of the epiblast undergo XCI in a random fashion. After the establishment of epiblast XCI, the choice of silenced XC is believed to be maintained in all clones of initial choice descendants. XCI is currently estimated to begin at E6.5 and end at E9.5 (Lee et al., 2011; Lee and Bartolomei, 2013; Tan et al., 1993). This time window also refers to the gastrulation of the embryo in which all germ layers are formed (Kojima et al., 2014).

The molecular mechanisms of XCI, in both imprinted and random forms, rely on the *cis*-acting control region called the X-inactivation center (Xic) (Brown et al., 1991b). This center has been mapped to a 100-500 kb region in Xq13 and contains the well-characterized *Xist* long noncoding RNA (lncRNA) (Brown et al., 1991a). Mentioned briefly before, *Xist* is the primary gene responsible for XCI. Its transcription occurs solely on the Xi and coordinates whole-chromosome silencing by “coating” the Xi with its presence during silencing initiation (Marahrens et al., 1997). Through binding with polycomb repressive complex 2

(PRC2) (Zhao et al., 2008), the epigenetic complex responsible for repressive H3K27me3 DNA marking, *Xist* coating translates into H3K27me3 modifications amongst 3,000 to 4,000 polycomb sites on the Xi. This results in the debilitated and dense XCi whose characteristics helped lead to the detection by Barr in 1949 (Barr and Bertram, 1949) and the subsequent discovery of XCI by Lyon in 1961 (Lyon, 1961). Other lncRNAs are located in the Xic, such as *RepA, Tsix, Xite, Jpx/Enox, Ftx,* and *Tsx*, with each being involved in different aspects of XCI control through *Xist* (Lee and Bartolomei, 2013). For example, *Tsix* controls XC pairing and counting choice (Bacher et al., 2006), whereby *RepA* (Zhao et al., 2010) and *Jpx* (Tian et al., 2010) directly regulates *Xist* transcription and spread of silencing. The XC's three-dimensional confirmation also seems to play a role in whole chromosomal silencing (Engreitz et al., 2013). *Xist* spreading initially locates to gene-rich regions on the XC, which after being silenced, locate to a silent nuclear compartment. *Xist* then moves on to the rest of the chromosome via proximity transfer.

Imprinted XCI appears to be predetermined based on XC marks set in each parent's germline. How does random XCI take place after the imprinted form is erased? A current model suggests control through the interaction of stem cell factors and *Xist* transcription (Schulz and Heard, 2013). Concomitant *Xist* upregulation in the ~E5.75 epiblast correlates with downregulation of factors including *Rex1* and *Prdm14* (Hayashi et al., 2011). The core pluripotency factors *Oct4*, *Nanog* and *Sox2*, do not seem to be affected. *Rex1* is a likely important candidate controlling random XCI onset. It targets the X-dosage sensitive Rnf12

ubiquitin ligase (Gontan et al., 2012) which remains the only factor whose overexpression leads to ectopic *Xist* upregulation in male cells (Pollex and Heard, 2012).

2. Genomic imprinting

PO-specific modifications of autosomal genes, like XCI, can be traced back to the parent's germ line. In the germ line, genomic imprinting begins at specific genomic locations called imprinted control regions (ICRs). These regions simultaneously regulate clusters of 3-12 genes through DNA methylation and histone modifications across 20-3,700 kb (Lee and Bartolomei, 2013). Clusters contain protein-coding genes and at least one non-coding RNA (ncRNA), which performs regulatory functions within a cluster in *trans* and/or *cis.* (Bartolomei and Ferguson-Smith, 2011). Out of the 20 clusters known, 16 maternally imprinted ICRs are located in promoters and four paternal ICRs are located within intergenic regions (Bartolomei and Ferguson-Smith, 2011). This suggests genomic patterns of ICR locations show PO effects. Additionally, it reflects that imprinting is more prevalent in the female germ line overall.

Somatic ICR imprints are retained throughout the lifetime of an animal, except in the case of cancer where imprints can be lost (Jelinic and Shaw, 2007). Germ line imprints are resistant to all early embryonic waves of genome-

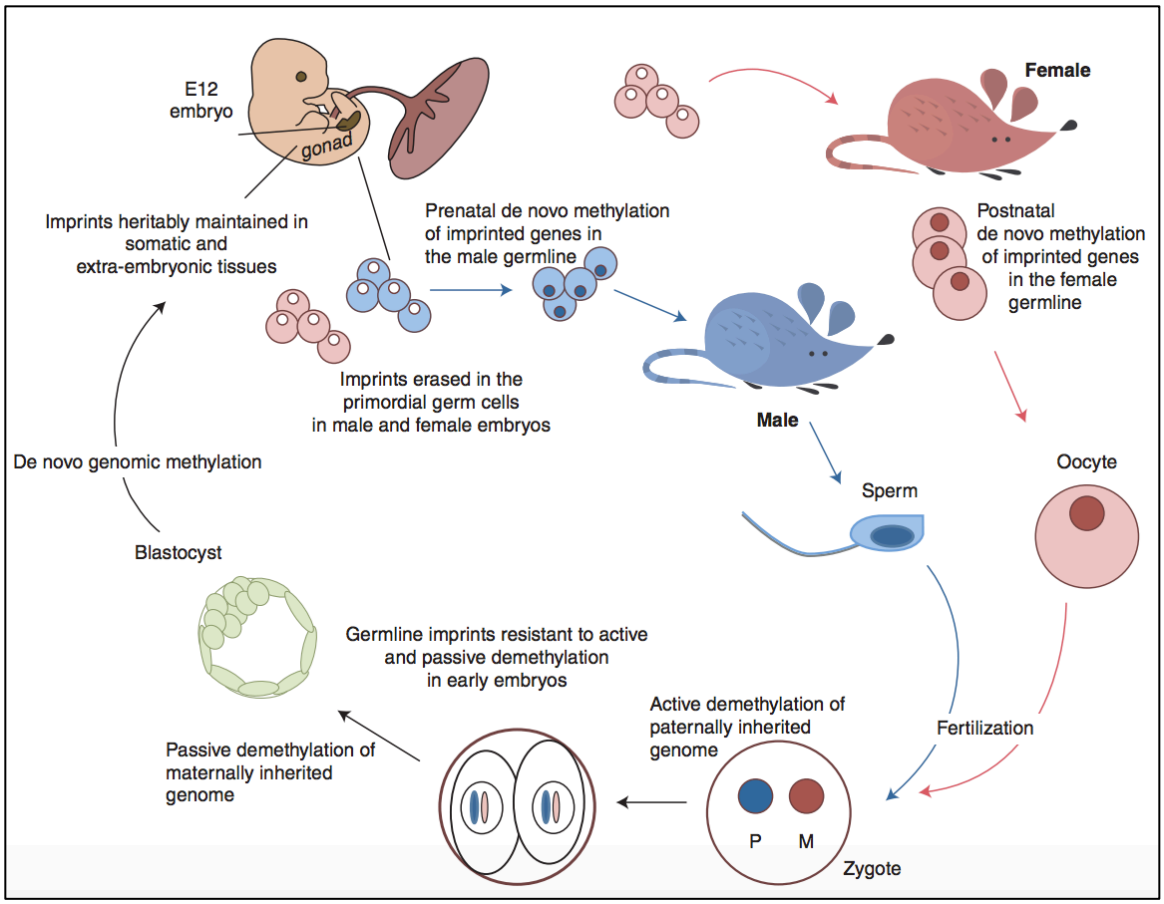

Figure 2. The cycle of genomic imprinting (adopted from Bartolomei and Ferguson-Smith, 2011). Sex-specific imprinting of ICRs occurs prenatally in the male germ line and postnatally in the female germ line. Propagation of imprinted DNA resists early embryonic forms of genome-wide epigenetic changes and incorporates into all somatic and extra-embryonic tissue. Primordial germ cells reset imprints around E12 after genital ridge migration is complete.

wide epigenetic changes and are incorporated into all somatic tissues. The cycle of imprinting begins with imprint erasure in post-migratory primordial germ cells (PGCs) at E12 (Figure 2) (Hajkova, 2011). After PGC differentiation, ICR methylation is imposed between mitotic arrest and birth in male prospermatogonia, and postnatally during the oocyte growth phase prior to ovulation (Davis et al., 1999). De novo germ line methylation at ICRs is then accomplished through the DNA methyltransferases, DNMT3A and DNMT3L

(Adalsteinsson and Ferguson-Smith, 2014). Once set and transmitted, all imprints are incorporated into somatic and extra-embryonic tissue of offspring, with resetting occurring in the PGCs.

ICRs control PO-specific modification of genes via an intermediary methylation at differentially methylated regions (DMRs), or somatic control regions. Methylation of DMRs can occurs simultaneously with germline ICRs or in a differentiation-dependent manner (Reik and Walter, 2001). Most DMRs are CpG islands, where methylation confers both inactive and active alleles depending on the gene. Indeed, imprinted cluster organization and the reading of imprinted genes is diverse across clusters (Reik and Walter, 2001). Much of this diversity arises from multi-gene lncRNA regulation in combination with conformational chromatin effects due to insulator and enhancer properties (Lee and Bartolomei, 2013).

Imprinted Grb10 regulation

Growth-factor receptor binding protein 10 (*Grb10*) is an imprinted gene characterized by unique tissue-specific regulation and function due to its genomic structure. On a functional level, Grb10 fulfills an adaptor protein role by interacting with many receptor tyrosine kinases and signaling molecules (Garcia-Palmero et al., 2017; Lim et al., 2004; Liu et al., 2014), enabling numerous cellular functions (Lim et al., 2004). According to germline knock out experiments, the physiological functions of each *Grb10* allele have been suggested to be different. Accordingly, the maternal allele is ascribed to growth

control over the body (Wang et al., 2007) and placenta (Charalambous et al., 2010), whereby the paternal allele may regulate social behavior (discussed in chapter 4) (Garfield et al., 2011).

The imprint status of *Grb10* alleles is regulated at multiple levels. An ICR controlling *Grb10* imprinting is located in the paternal *Grb10* promoter region which also contains the DMR (Shiura et al., 2009). Deletion of this ICR causes dysregulation of the neighboring *Cobl* and *Ddc* genes thereby inferring a three gene imprinted cluster is regulated and defined by *Grb10*'s ICR (Shiura et al., 2009). Separate promoter regions control maternal and paternal isoform transcription, whose gene products differ in the 5' untranslated (UTR) region and an alternatively spliced and uncharacterized maternal-specific exon 5 (Plasschaert and Bartolomei, 2015) (UCSB genome browser). Each promoter sits in a CpG island designated CGI1 for maternal and CGI2 for paternal transcription, respectively (Yamasaki-Ishizaki et al., 2007). K9/K20me3 methylation is found on the maternal DMR allele in most non-neuronal tissues, which corresponds to active 1A maternal transcription (Sanz et al., 2008)(Figure 3). In the same tissues, a CCTC-binding factor (CTCF) chromatin interaction and K27me3/K4me2 marks are found on the paternal DMR allele with repressed 1B1, 1B2, and 1C promoter activity (Plasschaert and Bartolomei, 2015). Neuronal differentiation changes CGI2 by releasing CTCF binding and K4me3 methylation from paternal DMR allele thereby allowing K9/27 acetylation of the promoter and associated transcription (Sanz et al., 2008). No changes are observed at the maternal CGI1 or CGI2 promoters in neurons. However, H3K27 histone

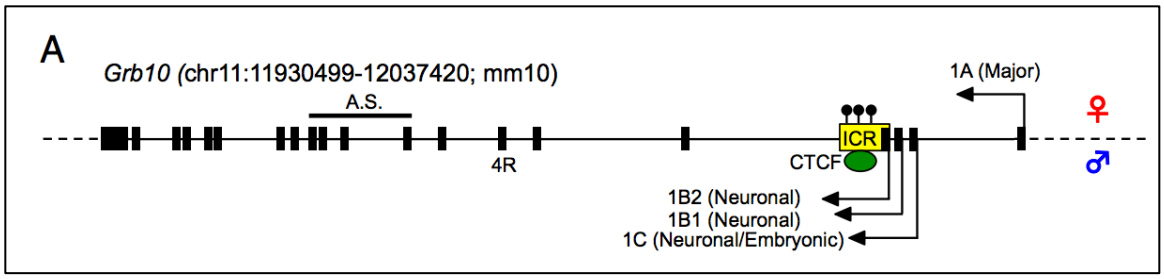

Figure 3. Schematic of *Grb10* imprinting correlated with major (1A) isoform transcription (adopted from Plasschaert and Bartolomei, 2015). In most non-neuronal tissues the maternal allele is transcribed in the presence of a methylated DMR, where the paternal DMR allele remains silent due to CTCF insulation. In this configuration, the maternal isoform (1A) is transcribed while all possible paternal isoforms (1B1, 1B2, 1C) are not. In the paternally active case, maternal DMR methylation remains and paternal methylation changes from bi- to monovalent with removal of CTCF binding.

modifications are found associated with the maternal promoter, corresponding to its allele-specific silencing (Yamasaki-Ishizaki et al., 2007).

3. Brain-specific imprinting effects

The molecular intricacies of imprinting are believed to have important physiological functions. The existence of many behavioral disease states related to imprinting demonstrates the necessity of imprinting for normal brain development (Curley, 2011; Kernohan and Berube, 2010), and disturbances in imprinting can be causes of schizophrenia and autistic spectrum disorders (Crespi, 2008; Wilkinson et al., 2007). Therefore, adjustments of gene dosage based on parent-of-origin is required for normal brain function (M. et al., 2004).

Initial importance of genomic imprinting in brain systems was demonstrated by pronuclear transfer experiments. In these experiments, Allen and colleagues transplanted reporter cells of uniparental inheritance (i.e. paternal or maternal disomic cells) into normal embryos (Allen et al., 1995; Keverne et al.,

1996). The resulting chimeric mice enabled visualization of each uniparental cell type's localization and developmental consequence in the brain. Cells only expressing paternal genes were shown to inhibit brain growth, localizing within the hypothalamus, septal nuclei, and pre-optic areas, whereas maternal gene-expressing cells contributed towards brain growth with neocortical occupancy (Keverne et al., 1996). These findings suggested that paternally expressed genes (PEGs) and maternally expressed genes (MEGs) function dichotomously within brain systems and neurodevelopment. Indeed, PEGs were shown to reside where primitive and autonomic behaviors are controlled (hypothalamus, septum), and MEGs seemed to occupy areas where more complex cognitive processes are generated (cortex). However, experimental progress made on an imprinted gene-by-gene basis has since questioned the potential claims of this pattern, with individual imprinted genes showing very dynamic profiles of expression.

Imprinting an allele effectively produces a haploid locus. Since the possession of two functional alleles serves advantages to an organism's fitness, having one allele imprinted should serve a specific purpose that outweighs the advantages of the diploid state. The biological processes controlled by imprinted gene function must therefore be sensitive to the gene dosage of the genes imprinted. Attempts made to understand these functions in the nervous system commonly reveal a regulation over distinct behaviors, shadowed by expression patterns throughout brain systems (Wilkinson et al., 2007). Therefore, imprinting

of dosage-sensitive genes may facilitate a mechanism to shape circuit activity underlying specific behaviors.

The convergence of both imprinting syndrome phenotypes and experimental evidence in animal models indirectly supports this, although direct experimental evidence has yet to be produced. The imprinting Prader-Willi syndrome (PWS) results from disruption of PEG expression in the imprinted gene cluster on chromosome 15 (Cassidy et al., 2000). Behaviorally, patients with PWS show complications to thrive during infancy, learning alterations, hyperphagia, and an unusual sociable disposition characterized by diminished negative-affect signals (Cassidy et al., 2000). Mechanistically, GABAergic interneurons in the forebrain (Kuwajima et al., 2006) and gonadotropin-releasing hormone (GnRH) neurons of the hypothalamus (Miller et al., 2009) seem to be dysfunctional. These defects are attributed to lack of PEG *Necdin* (Ndn) expression. The reciprocal syndrome to PWS, Angelman syndrome, results from MEG disruption in the same chromosomal region (Cassidy et al., 2000). Angelman patients show learning disabilities, ataxia, seizures and abnormal EEGs (Summers and Feldman, 1999). Loss of MEG *Ube3a* expression underlies these phenotypes as demonstrated in a mouse knockout model(Jiang et al., 1998), where it is monoallelically expressed amongst Purkinje neurons, the hippocampus, and mitral cells of the olfactory bulb (Rougeulle et al., 1997). Uniquely, *Ube3a* expression is biallelic in all other brain regions.

Aside from imprinting syndromes, separate lines of evidence from animal models also portray distinct expression patterns of imprinted genes that govern

very specific behaviors. The paternally expressed *Peg3* regulates aspects of maternal behavior including milk letdown and pup retrieval (Li et al., 1999). A pup's ability to suckle is also regulated by *Peg3* (Li et al., 1999). *Peg3* expression is most notable in oxytocin-producing neurons of the hypothalamus as well as neurons of the medial amygdala, bed nucleus of stria terminalis, and hippocampus (Li et al., 1999). The PEG *Gnasxl* also controls the pup's ability to receive maternal milk through suckling. This ability is ascribed through *Gnasxl* expression in the hypothalamus, the facial, hypoglossal, and trigeminal motor nuclei, as well as distinct nuclei in the pons, including the locus coeruleus and the laterodorsal tegmental nucleus (Plagge et al., 2004). Lastly, *Nesp55* is a MEG involved in risk-tolerance, localizing predominantly in the raphe nucleus and locus coeruleus (Plagge et al., 2005). Altogether, the spatial brain patterns of multiple imprinted alleles suggest coordination amongst brain systems and circuits of behavior.

The outcome of the epigenetic-driven XCI process leads to mosaic, or variegated, distributions of patXC- and matXC-active cells in somatic tissue. The XC is home to the most brain-specific genes in relation to other chromosomes (Nguyen and Disteche, 2006). Many of the genes, when mutated, give rise to mental disease such as X-linked mental retardation (XLMR) and autism (Marco and Skuse, 2006; Raymond, 2006; Skuse, 2005). Unlike the patterned stereotyped expression observed in genomic imprinting cases, the overall depiction of chosen XCa distributions is random (Wu et al., 2014). This fits with clinical studies in which female X-linked patients show broad and variable

behavioral phenotypes and penetrance (Lee and Bartolomei, 2013). Some reports suggest the existence of a small, maternal bias in XCa brain tissue (see chapter 2) (Gregg et al., 2010; McMahon et al., 1983; Wang et al., 2010), but the question of how this relates to all regions and systems of the brain has not yet been addressed.

4. Specific Aims

The organization of the brain can be divided up into its functional parts, consisting of hemispheres, systems, regions, and circuits. As explained in this chapter, both forms of imprinting hold valuable potential in the control of brain function, and especially at the level of brain systems and behavioral circuits*. The purpose of my thesis is to characterize imprinted brain patterns amongst XCI and Grb10 imprinting at whole brain and cellular resolution, and investigate how the identified patterns may affect behavior*. In **chapter 2** I aim to characterize whole-brain XCI patterns in female XCa-EGFP heterozygous mice. Quantifications in segmented whole-brain datasets via advanced whole-brain microscopy provide XCa descriptions amongst regions, hemispheres, and the whole-brain. **Chapter 3** aims to determine the behavioral correlates of XCI patterns observed in chapter 1 using double transgenic XCa-EGFP/fragile X syndrome model mice. PO effects and circuit-level dysfunction of behaviors are explained in relationship to the quantified XCI patterns. Lastly, in **chapter 4** I aim to create a novel genetic approach in order to characterize the brain distribution of *Grb10*+ cells based on allelic composition (e.g. paternal, maternal, biallelic). I describe expression

patterns amongst 3 general expression trends observed, and characterize a putative midbrain circuit module controlling conditioned freezing behavior identified by *Grb10*'s imprint status in a distinct population.

Chapter II: Quantification of XCI dynamics at multiple levels of the brain

1. Rationale

The “random” nature of XCI determines the degree X-linked traits and mutations influence organ function in females. The timing of XCI, starting progenitor pool amount it occurs in, and selective forces acting upon initial choice of XCI can contribute towards this randomness and final distribution of XCa in a given tissue. The brain—from systems and regions down to individual neurons—enables behavior in part through the interdependencies of its spatial, working units. It is therefore crucial to quantitatively capture XCI distributions across the brain’s many functional compartments in order to understand the ways by which X-linked traits and mutations can shape behavioral output.

Previous mouse studies have partially explored the nature of brain XCI, mainly by investigating XCa ratios from crude tissue sources with conventional resolution. Gregg et al performed RNAseq in brain areas of F1 hybrid mice to indirectly assay XCI (Gregg et al., 2010). Using SNPs to identify PO, they identified an 11 and 19% maternal XCa bias in the medial prefrontal cortex (mPFC) and preoptic area (POA) of the hypothalamus, respectively. This bias was stronger for the mPFC and the results were supported by counting cortical only Xm-biased EGFP+ cells in separate experiments using a transgenic XCa-reporting mouse line (Gregg et al., 2010; Hadjantonakis et al., 2001). Using a similar F1 hybrid mouse-RNAseq approach to track the XCa parent-of-origin

(POI), an Xm-active bias was also found in mouse neonate whole brains, concluding that the degree of preferential paternal XC inactivation averaged across all brain regions and cell types was at ~6% (Wang et al., 2010). E12.5 neuroectoderm tissue lysate was shown to contain an 8.5% maternal XCa bias (McMahon and Monk, 1983). PGK isoform western blot densitometry (PGK is an X-linked gene) of PGK isoform hybrid mice lysates was used for XCI determinations. Tissue from other germ players (mesoderm and endoderm) positively correlated with the neuroectoderm and averaged a total 8.9% maternal XCa bias. Using an XCa *LacZ*-reporting mouse subsequent studies failed to replicate the bias in early embryos (Tan et al., 1993), though low sample size and resolution of assay leaves room for more studies. One human study determined XCI ratios across autopsy tissues representing the 3 germ layers (Bittel et al., 2008). Using the androgen receptor assay, a PCR-based XCI assay based on the polymorphic X-linked androgen receptor (Gale et al., 1996), the authors found that germ layer XCI status was correlated but did not show any bias in XCa (Bittel et al., 2008).

The studies above collectively point towards a small maternal XCa brain bias and perhaps in other tissues as well. However, the data do not define the cell amounts contributing towards ratios of allelic transcription or protein expression, which in most cases was what was measured. The ratio of measured transcription or protein expression per allele may or may not linearly reflect the amount of active Xp or Xm cells in a given sample. Directly measuring XCa from cell counts would provide more interpretable results. Finally, XCI ratios may vary

depending on brain system, region, or cell type. More studies are needed to understand if XCa choice is reflected similarly at all levels or in previously undefined compartmentalized ways.

The purpose of my experiments is to quantitatively determine paternal versus maternal arrangements of XCa choice at varying spatial scales (depicted in Figure 4) of the brain. My approach relies on high-resolution whole-brain imaging in the mouse and computational methods (see Material and methods) developed in the Osten laboratory (Kim et al., 2015; Ragan et al., 2012), in combination with an XCa EGFP-reporting knock-in mouse line. Using these methods, in addition to fluorescence-activated cell sorting (FACS) of defined cortical cell types, I determine XCI ratios with single-cell resolution across the whole-brain and its corresponding regions and hemispheres.

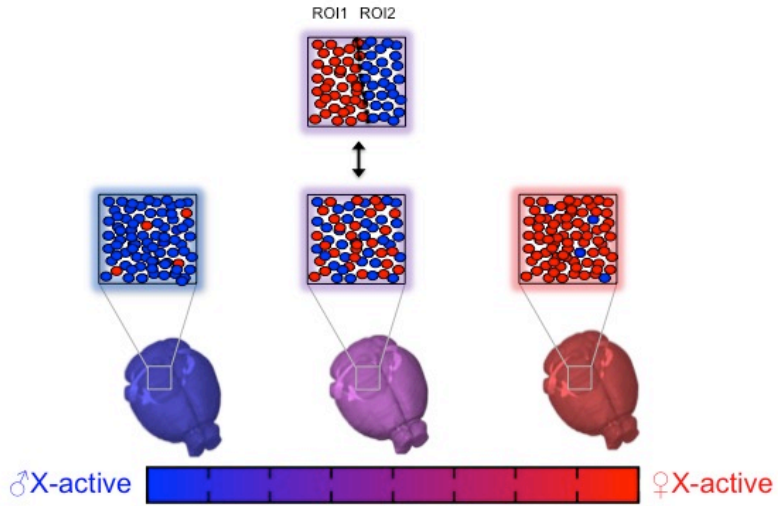

Figure 4. Theoretical XCa brain distributions. On a scale of paternal (100%, left) to maternal XCa active (100%, right), degrees of population bias or mixing could be found at the whole-brain and regional (shown) levels, as well as systems and left-right axis levels (not shown), each contributing towards influence of X-linked behavioral traits and mutational effects.

2. Materials and Methods

Subjects

Adult mice (8-10 weeks old) were used for whole-brain imaging experiments and 5-7 week old mice used for FACS studies. All animals were housed under a 12-hour light/dark cycle (0600 ON, 1800 OFF), had access to food and water *ad libitum*, and were housed with littermates. All experimental procedures were performed in accordance with CSHL Animal Care and Use Committee Guidelines. Mice were maintained on a C57Bl6/J background. For single-cell fluorescent XCa reporter mice, we chose the MeCP2-GFP mouse line obtained from the Jackson laboratory (stock # 014610). MeCP2 is a gene located at chromosomal position X A7.3 and is subject to XCI. Developed in the laboratory of Adrian Bird, this mouse line contains an in-frame EGFP knock-in cassette at the 3' UTR of the MeCP2 locus (Brown et al., 2016; Linhoff et al., 2015; Lyst et al., 2013; McLeod et al., 2013). Driven and regulated by the endogenous MeCP2 promoter/enhancers, MeCP2-GFP expression leads to normal MeCP2 levels and subcellular localization of MeCP2 protein that is fused at the C-terminus with EGFP Expression of the fusion allele does not alter neuronal physiology (McLeod et al., 2013), and mice are successfully bred to homozygosity without behavioral or reproductive complications. In addition, strong expression of MeCP2-GFP favors neurons of many types (Schmid et al., 2008), thereby circumventing biased effects of XCI determinations based on expression profile. Therefore, I believe that the reporter allele used for my experiments enables faithful and reliable tracking of the XCa with known PO. Maternal or paternal XCa-reporting female mice were obtained in separate

heterozygotes by crossing homozygous females ($MeCP2^{GFP/GFP}$) or hemizygous males ($MeCP2^{GFP/Y}$), respectively, with wild-type C57Bl6/J mice. Homozygous reporter mice were obtained by crossing homozygous females ($MeCP2^{GFP/GFP}$) with hemizygous males ($MeCP2^{GFP/Y}$). For FACS and imaging studies of XCI within defined cortical cell-types, the Fezf2-2A-CreER (unpublished; kindly provided by Huang laboratory, CSHL) Cre driver line was used to inducibly label layer V-VI pyramidal neurons, a subset of excitatory neurons. Parvalbumin (PV)-2A-CreER (JAX stock # 028580; kindly provided by Huang laboratory, CSHL) was used to inducibly label a subset of inhibitory cortical neurons and PV-IRES-Cre mice were used for imaging studies only and constitutively label the same cells as the PV-2A-CreER line. Ai14 (JAX stock #007914) mouse line was used as the Cre reporter mouse, which expresses CAG-driven tdTomato upon Cre expression and recombination at the Cre reporter allele located in the Ros26 locus. XCa was visualized within Fezf2 and PV+ cortical neurons in triple transgenic mice containing MeCP2-GFP, cell-type specific Cre driver, and Ai14 Cre reporter alleles. The triple transgenic mice were generated by first crossing homozygous female or hemizygous MeCP2-GFP mice with Ai14 homozygous mice. Resulting double transgenics were inbred to generate double homo- or hemizygous MeCP2/Ai14 mice. Males were crossed into female Cre-driver lines to label active Xp and females were crossed into males to label active Xm in Fez2 or PV+ neurons. Inductions of CreER to allow tdTomato labeling of Fezf2 (n=13; 4 maternal XCa-reporting; 9 paternal) and PV-expressing cells (n=15; 11

maternal XCa-reporting; 4 paternal) were performed by administering intraperitoneal (I.P.) injections of tamoxifen (2mg) at P21 and P28.

Brain preparation

Animals were euthanized via transcardial perfusion under ketamine/dexmedetomidine anesthesia. Dissected brains were post-fixed overnight in 4% paraformaldehyde at 4 C, incubated for 48 h in 0.1 M glycine/0.1 M PB for auto fluorescent quenching, and then stored in 0.05 M PB until imaging. Prior to imaging, brains were embedded 4% oxidized agarose in 0.05 M PB using custom molds and holders to maintain consistent embedding position. Embedded brains were crosslinked in 0.2% sodium borohydrate solution for 3h at room temperature or overnight at 4 C.

Serial Two-Photon Tomography (STPT)

The Tissuecyte1000 instrument was used for all imaging experiments (Tissuevision, (Ragan et al., 2012)). This system combines a high-speed multi-photon microscope with a fully integrated vibratome for automated z-sectioning and image acquisition throughout the entire whole-mount sample. Embedded sample brains were imaged with a 20x objective in 270 serial sections at 50 um z-resolution (13.5 mm total z-length), with each section comprised of a 12 (x-axis, 700 um) by 16 (y-axis 700 um) field of view mosaic. Images were acquired with laser scan settings of 1 um/pixel at an integration time of 1 us. For optimal MeCP2-GFP+ excitation and detection, we used 910 nm laser wavelength with a

power of ~322 mW at the end of the objective. Constant laser settings, PMT detector settings, and a 50 um Z- step sample imaging depth was used for all samples.

Automated XCa-GFP cell counting

Raw image tiles for each brain was illumination corrected, stitched in 2D with Matlab and aligned in 3D using Fiji software (Ragan et al., 2012). For reliable automated MeCP2-GFP detection from full brain datasets, we implemented convolutional networks (CNs) (Turaga et al., 2010). CN training for detection of MeCP2-GFP+ cells in the STPT datasets was accomplished as in previous studies from the Osten lab (Kim et al., 2015), with CN training performed on human marked-up ground truth data (biological expert identified MeCP2-GFP+ nuclei) of MeCP2-GFP brains. CN performance was determined based on F-score calculations (F-score = the harmonic mean of the precision and recall, where precision is the ratio of correctly predicted cells divided by all predicted cells and recall is ratio of correctly predicted cells divided by ground truth positive cells; ~1800 MeCP2-GFP+ cells were marked/expert/brain). Composite F-scores for MeCP2-GFP CN was obtained by determining F-scores in 8 FOVs (400 (X) um by 400 (Y) um) representing different cellular density and imaging content in 3 separate heterozygous MeCP2-GFP brains (24 FOVs total). Stable precision and recall was seen for all regions analyzed, delivering a composite F-score of 0.84 (Figure 5). In the CN output images, signal smaller than 10 μm^2 was removed as noise. We did not analyze MeCP2-GFP+cells in the

cerebellum due to a high false negative rate in homozygous reporter brains due to a cellular autofluorescence specific to this brain region (data not shown). In order to normalize the performance of CN for each brain, the brightness of MeCP2-GFP+ signal for each sample was normalized by the mean and standard deviation of tissue autofluorescence signal from a coronal section corresponding to bregma position of +0.20 mm.

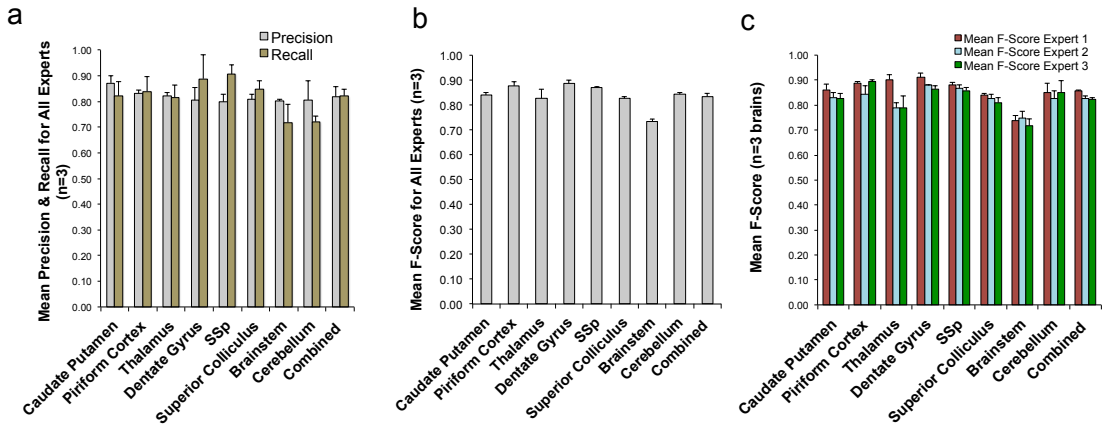

Figure 5. *MeCP2-GFP*+ nuclei CN F-score performance. a) Mean precision and recall of 8 regions and regional average (combined) from 3 experts b) Mean F-score from precision and recall values of a) averaged by experts c) Mean F-score of 3 brains with each individual expert's scoring shown for every region (all values + SEM)

3D brain registration and anatomical segmentation

Registration of individual brains to a standardized reference space was computationally achieved as published by the Osten lab (Kim et al., 2015). In short, affine transform was calculated using 4 resolution levels and B-spline with 3. Advanced Mattes mutual information (Mattes et al., 2003) was the metric used to measure similarity between moving and fixed images. Image similarity function is estimated and minimized for a set of randomly chosen samples with each

image in a multi-resolution and iterative fashion (Ragan et al., 2012). Entire warping of whole-brain images is done using elastix (Klein et al., 2010). Anatomical segmentation of Allen Brain Atlas (ABA) labels onto sample brains was made possible also as previously published (Kim et al., 2015). Briefly, ABA labels are transformed into the reference space each individual sample is registered to. Cell counts throughout the brain are segmented by labels/regions of multiple hierarchies. For the experiments in this thesis, 741 regions were used for analysis.

2D-3D cell count correction and density measurements

Detected 2D cell count values were transformed by a stereological 3D conversion factor obtained by the following way. First, counting boxes of 200 um x 200 um x 50 um (xyz) were acquired in 6 regions of a heterozygous MeCP2-GFP brain at 2.5 um z resolution. Optical imaging depth spanned 50 um around the normal 50 um depth (i.e. 25-75 um below the tissue surface). Second, MeCP2-GFP CN was run on the middle optical section corresponding to the 50 um depth. Third, manual markup of MeCP2-GFP+ nuclei was performed in each counting box using the stereological counting rules of Williams and Rakic (Williams and Rakic, 1988). Lastly, a conversion factor for each region was calculated by dividing manual 3D counts by 2D CN count of the middle section. This factor was averaged over the 6 regions reaching a final conversion factor of 2.6. (Figure 6). Cellular density was obtained by 1) transforming ABA labels onto

individual brains, 2) converting ROI assigned pixels to mm3, 3) dividing mm3 values by 2.5 um Z-corrected absolute cell counts to arrive at cells/mm3.

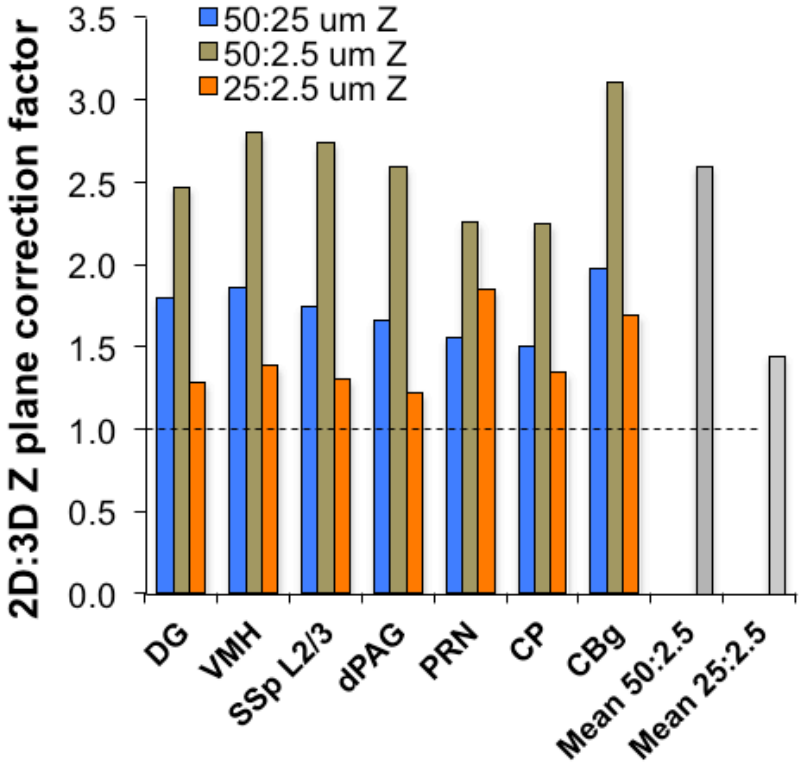

Figure 6. 2D: 3D cell counting conversions. Cell count conversion factors for 50:25, 50:2.5, and 25:2.5 um Z resolution were measured across 7 regions of the brain. For more details see Materials and Methods section of this chapter (DG = dentate gyrus, VMH = ventromedial hypothalamus, SSp L2/3 = primary somatosensory cortex layer 2/3, dPAG = dorsal periaqueductal gray, PRN = pontine reticular nucleus, CP = caudate putamen, CBg = cerebellum, granule layer).

Cortical dissociations and FACS

Unilateral cortical hemispheres were used for cell-type specific XCI studies. Cortical dissections were performed from freshly decapitated mice brain in Hibernate-A (GIbco; A11473DJ) media supplemented with glutamax (Gibco; 35050) and B27 supplement (Thermo Scientific; 17504001). Single hemispheres

were minced briefly with a razorblade, transferred to a new tube and incubated in pre-activated papain (10 U/ml; Worthington-biochem; LK003716) diluted in 10 ml Hibernate-A supplemented with glutamax for 15 minutes at 37 C. At 5 minutes of incubation, 2 ug of DNase I (Roche; 10104159001) was added to solution to prevent cell clumping. 3 triturations were performed over the 15 minutes to facilitate single-cell suspensions. Suspensions were then carefully transferred to an Opti-prep (Sigma;D1556) density gradient column diluted in hibernate-A (with B27) and spun for 15 minutes at 800 rcf. Optiprep media was removed and neuronal pellet was resuspended in fresh 5 ml hibernate A (with B27) and respun at 200 rcf for 5 minutes. Cell pellets were resuspended in 1 ml PBS (20mM HEPES, pH 7.0; 1 % FBS) and mesh filtered to remove debris. Unstained controls were independently stained and samples were co-stained with 1 uM DAPI (to mark damaged cells) and DRAQ5 (Cell Signaling Technology; 4084) (to label viable cells) for at least 10 minutes prior to sorting.

Cell analysis and sorting was performed using a FACSAria II SORP (BD Biosciences, San Jose, CA) at 25psi with the 100 um nozzle. Fluorescent parameters included DAPI, DRAQ5, GFP and tdTomato. DAPI was excited by the 355nm UV laser and its emission was collected with a 450/50 filter. The 633nm red laser was used to excite the DRAQ5 and its emission collected with the 780/60 filter. tdTomato was excited by the 561nm yellow/green laser and emission collected with the 582/15 filter. Lastly, GFP was excited by the 488nm blue laser and emission was collected with the 530/30 filter. Unstained and single color controls were used to set PMT voltages and eliminate spectral overlap

between fluorescent channels. Experimental samples were first gated on DAPI-/DRAQ5+ populations. This gate was then applied to a scatter plot for elimination of debris and then doublet discrimination. Single cells were viewed in a dot plot of GFP-A (x-axis) and TdTomato-A (y-axis). Both the tdTomato+/GFP+ and tdTomato+/GFP- populations were then sorted to 5000 cells/group. Total tdTomato+/GFP+ and tdTomato+/GFP- detected events out of 100,000 total detection events were used to determine XCa ratios.

Immunohistochemistry and confocal imaging

Cell-type specific expression (neuronal versus non-neuronal) of the MeCP2-GFP allele was studied though immunostaining and confocal imaging procedures. 100 um vibratome-processed, free-floating coronal sections of a homozygous MeCP2-GFP reporter mouse brain were processed. Sections were washed 3 times in PBS followed by blocking for 1 h at room temperature in PBS-T (PBS, 0.2% Triton-X 100) containing 5% donkey serum. Sections were then incubated overnight at 4 C in blocking solution containing rabbit anti-NeuN (Millipore, ABN78) primary antibody at 1:1000. After washing, NeuN-stained sections were incubated with anti-rabbit AlexaFluor-568-conjugated secondary antibody (Thermo-Scientific, A10042) diluted 1:500 for 1 h at room temperature. After washing excess secondary antibody, sections were mounted, DAPI-counterstained, and coverslipped for imaging. Confocal images were acquired with a Zeiss LSM780 confocal microscope using a 561 laser and corresponding dichroic and filter sets. Images were captured with a 40x oil immersion objective.

Total cell amounts for MeCP2-GFP+/NeuN-, MecP2-GFP+/NeuN+, and MeCP2-/NeuN+ for each FOV (212 um X x 212 um Y) were manually detected and quantified using Fiji image processing package.

Statistics

Whole-brain absolute cell count and densities and whole-hemisphere densities were compared amongst Xm-active (n=10) and Xp-active (n=12) brains using an unpaired Mann-Whitney U non-parametric t-test (bimodal distributions for each genotype were observed). Left-right whole-hemisphere comparisons for each genotype (Xm-active, Xp-active, XmXp-active) were statistically analyzed using paired Wilcoxon signed-rank tests. A two-way ANOVA was applied to compare cell density amongst MeCP2-GFP genotype and ROIs. Sidak multiple comparison-corrected post-hoc tests were used to analyze genotype across individual ROIs. Relationships amongst whole-brain and regional cell density measurements were tested by Pearson correlations. The same two-way ANOVA approach was used for hemispheric XCa cell density comparisons. Cell-type specific XCa ratios were compared with paired Wilcoxon signed-rank tests, and XCa comparisons between cell-types were compared using Mann Whitney U t-tests. Correlational analyses amongst whole-brain and individual ROI cell density was performed with Pearson's correlation. Alpha was set at 0.05 for all tests. All statistical testing was performed with Graphpad Prism software version 7.0.

3. Results

To understand the cell type identity of the *MeCP2-GFP*+ nuclei detected by our methods, I first quantified double labeling of NeuN (neuronal marker)-stained homozygous MeC2P-GFP in serial brain sections (Figure 7). Sampling from 10 regions (939 cell counts total) of a homozygous MeCP2-GFP reporter brain, the majority of NeuN+ neurons (91%) counted expressed also MeCP2-GFP. In addition 68% of MeCP2-GFP cells were quantified as NeuN+ neurons thereby leaving 32% of cells expressing the *MeCP2-GFP* reporter allele as non-neuronal – glial and possibly also endothelial cells.

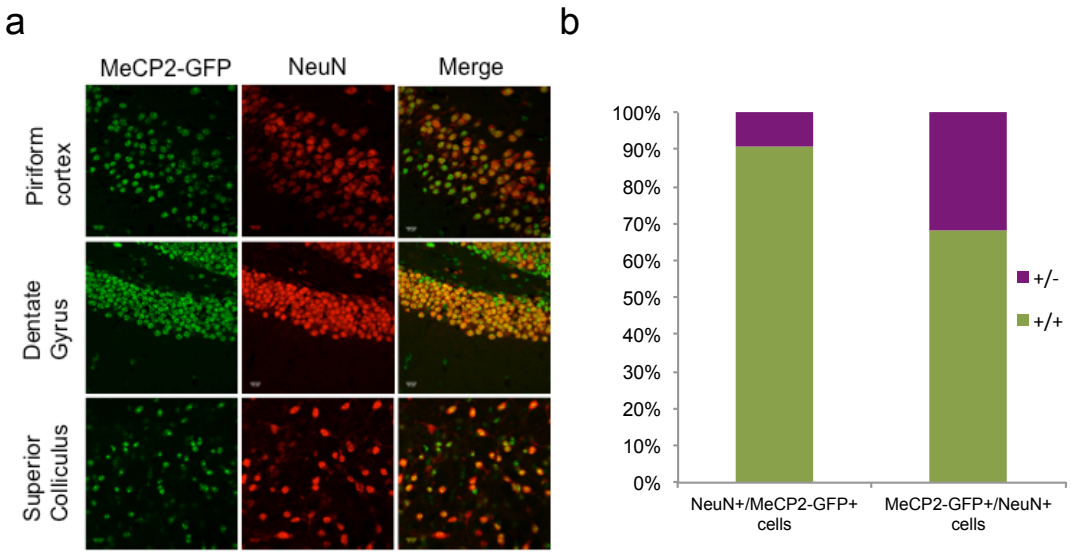

Figure 7. Assessment of neuron-specific MeCP2-GFP reporter allele expression. a) Representative confocal images of NeuN-stained sections from 3 areas of the brain (scale bar = 15 um). b) Quantification of neurons (NeuN+) expressing MeCP2-GFP (left bar) and MeCP2-GFP+ cells that are neurons (right bar).

Whole-brain XCa quantification

Reciprocal *MeCP2-GFP* reporter allele transmission allows PO-specific XCa reporting in separate groups of mice (schema in figure 8).

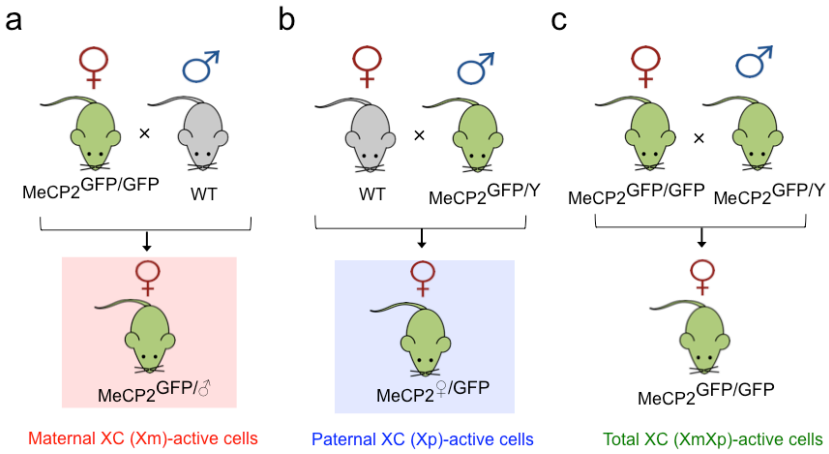

Figure 8. Breeding strategy to track PO XCa with MeCP2-GFP reporter mice. a) Maternal or b) paternal Xca cells (bottom left and middle) were visualized and measured by crossing homozygous females ($MeCP2^{GFP/GFP}$) or hemizygous males ($MeCP2^{GFP/Y}$), respectively, with wild-type or C57Bl6/J mice c) For 100% control comparisons, homozygous reporter mice (bottom right) were obtained by crossing homozygous females ($MeCP2^{GFP/GFP}$) with hemizygous males ($MeCP2^{GFP/Y}$)

The distribution of the *MeCP2-GFP*+ cells in maternal (n=10), paternal (n=12), and homozygous (n=6) MeCP2/XCa-GFP reporter brains was first analyzed at the whole-brain (organ) level (Figure 9). We measured (mean ± SD) $2.2 \times 10^7 \pm 4.5 \times 10^6$ maternal, $1.7 \times 10^7 \pm 5.3 \times 10^6$ paternal, and $3.9 \times 10^7 \pm 2.5 \times 10^6$ homozygous cells in total (Figure 9b), which represents cell density of $5.9 \times 10^3 \pm 1.4 \times 10^4$ maternal, $4.7 \times 10^4 \pm 1.4 \times 10^4$ paternal, and $10.7 \times 10^4 \pm 6.9 \times 10^3$ homozygous cells/mm3 (volume-normalized cell counts) (Figure 9c). As expected the total cell counts in the heterozygous brains were approximately half of that of the homozygous brains. Both at the total cell count and volume-normalized cell density level the measurements of the maternal XCa cells were

significantly higher than the paternal XCa cells: 21%; maternal median = 5.9 x 10^3, paternal median = 4.4 x 10^3); U(20) = 29, p = 0.0426) than the paternal XCa-measured brains. Normalizing by the homozygous (100% control) cell counts, I conclude that in the heterozygous brains the mean maternal values were 55% (Max - 70%, Min- 36%; Range -34%), while paternal values were 45% (Max - 67%, Min- 26%; Range - 41%) (Figure 10).

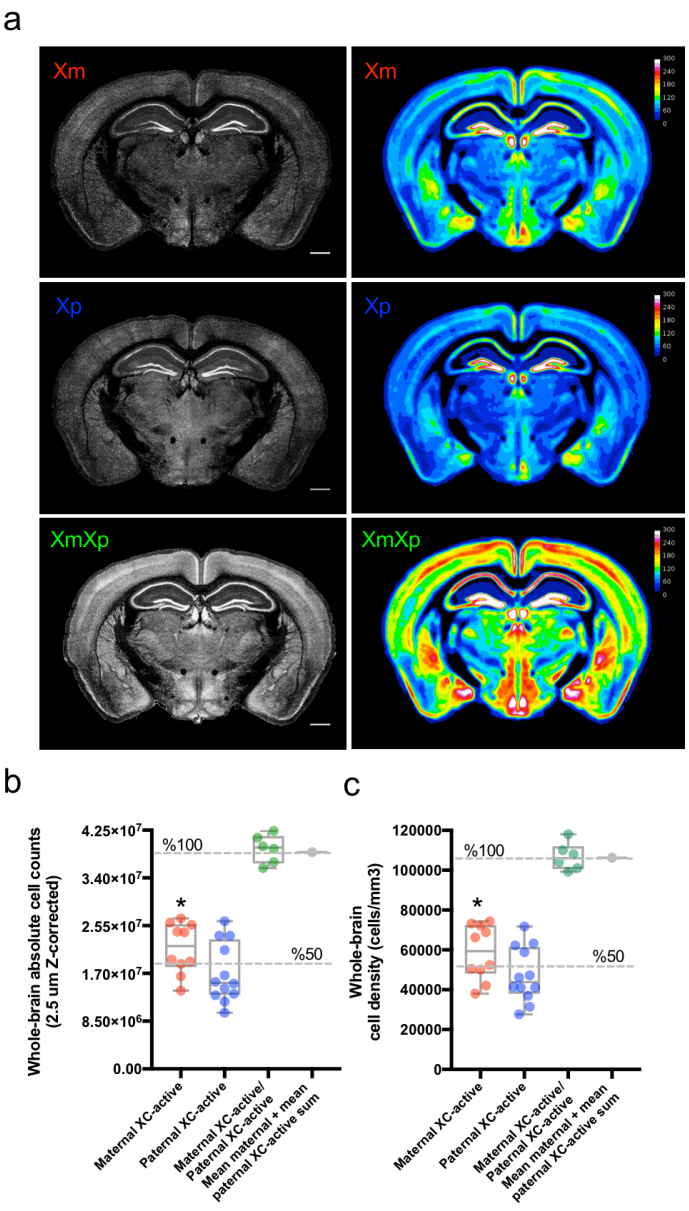

Figure 9. Whole-brain XCa quantification. a) Representative STP-generated coronal images (left - grayscale) of maternal (Xm, top), paternal (Xp, center), and homozygous (XmXp, bottom) MeCP2-GFP reporter brains (scale bar = 750 um). Warped mean cell counts of each genotype for corresponding sections in a) are visualized as a heat map in voxelized space (right). Heat map color legend of each example is shown to the right on a 16-color gradient scale from white (max; 300 cells/voxel), yellow (middle; 150 cells/voxel), to black (0 cells/voxel). b) 2.5 um Z-corrected cell counts and c) cell densities of maternal (red), paternal (blue), and homozygous (green) MeCP2-GFP reporter whole-brains. Data is shown as box and whisker plots displaying individual sample values as dots, min/max values as whiskers, and median at line within the box. The mean sum of heterozygous groups are plotted on far right with a dashed line indicating 100% (top) or 50% (middle) total possible counts or density based on this value. *p<0.05 versus paternal XC-active.

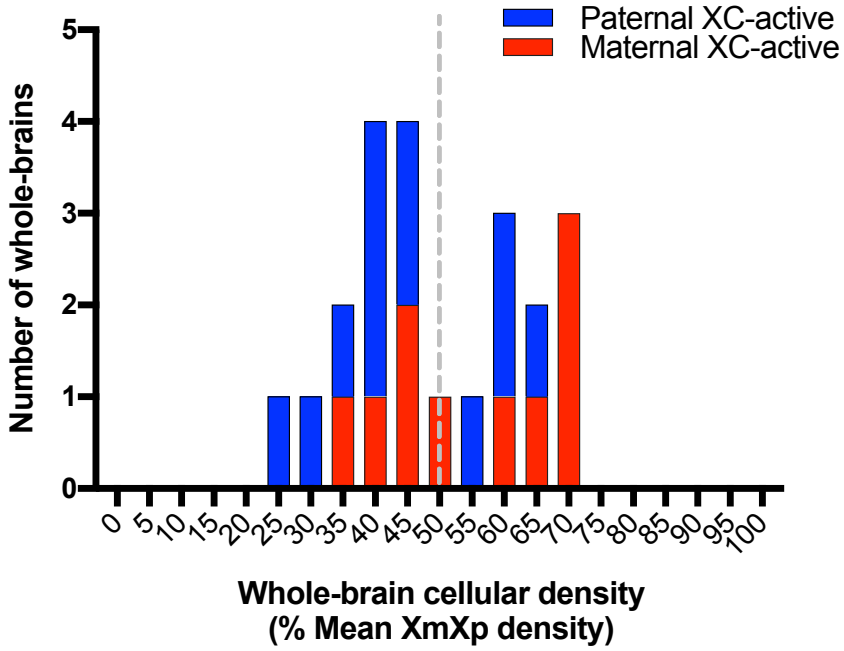

Figure 10. Whole-brain density frequency histogram. Individual whole-brain densities from maternal XC-active (red) and paternal XC-active reporters (blue) are normalized to the mean XmXp-active reporters and plotted in 5% bins. Dotted line is placed at 50%.

Brain-wide regional XCa quantification

I next explored XCa distributions within 740 regions of the brain. Using a two-way ANOVA, mean density comparisons revealed a significant maternal bias

main effect ($F(1, 14940) = 2021$, $p < 0.0001$) with a mean ROI percent difference of 19% (Figure 11, b-d). No trends for paternal XCa biases were observed amongst any ROI examined. Sidak-corrected post-hoc testing of individual ROI XCa comparisons found 7 ROIs (ORBm2, AOBgr, POST ASO, NC, PVp, PMv) containing significantly more maternal XCa cells than paternal (Fig 11, e). Next I asked how the XCa distribution at the organ level pertains to its regions. Is the whole-brain status the same as all its parts or is it merely an average of variable distributions throughout all regions? For this purpose, Pearson's correlational analysis amongst whole-brain and individual ROI cell density was performed for all 22 heterozygous brains imaged. As shown in figure 11, all ROIs showed positive correlations (i.e. R^2 values 0-1) with the central tendency of values falling at a strong correlational value of 0.8 (Figure 11, f). With the exception of 2 ROIs (TMv, LRNp), all 740 ROIs cell density assayed were significantly correlated with whole-brain cell density (figure 11,g). I conclude that the female mouse brain contains a modest 12.5% bias in maternal XCa/paternal XCi cell density that is distributed evenly throughout the brain. Furthermore, whole-brain XCa status determines its regional profile with high correlation.

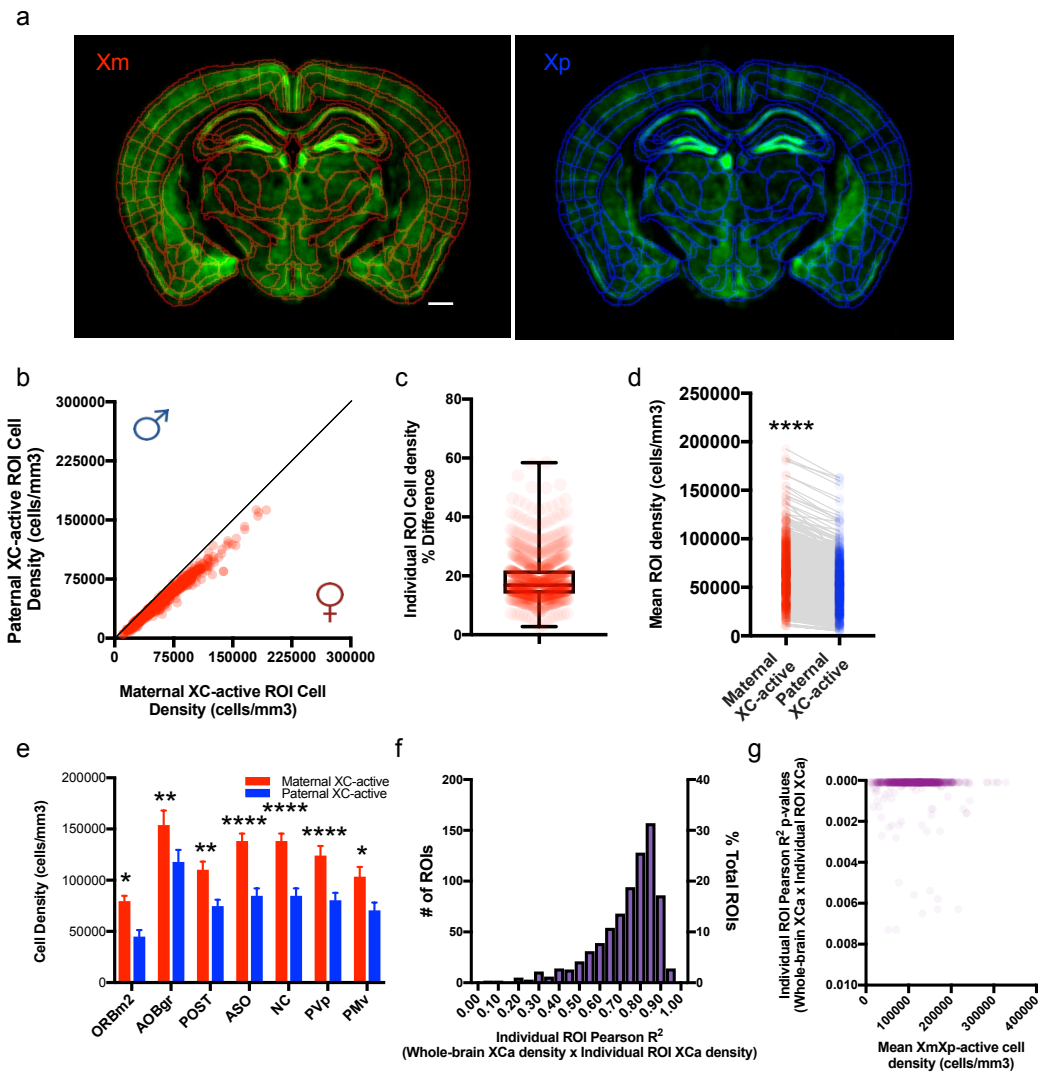

Figure 11. Brain-wide regional XCa quantification. a) Representative cell count-voxelized coronal images of Xm-active (left) and Xp-active (right) reporting brain with ABA label segmentation skeletonized and overlaid on each example (scale bar = 750 um). b) XY scatterplot of mean Xp-active versus Xm-active ROI density values, with a theoretical perfect trendline shown to mark boundaries of ROIs favoring paternal (left) or maternal (right) bias. c) Box and whisker plot of individual ROI percent differences of Xm- versus Xp-active cell density ROIs. Whiskers mark max/min values and box line indicating median value. d) Results of 2-way ANOVA main effect of PO XCa with each dot representing mean ROI cell density. e) 7 ROIs containing significantly more Xm-active cells than Xp-active identified by Sidak-corrected post-hoc test f) Frequency histogram of individual ROI Pearson R^2 values obtained from Pearson correlation analysis amongst whole-brain XCa and individual ROI XCa cell densities. g) Individual ROI p-values from acquired Pearson correlational analysis in panel plotted against mean ROI XmXp-active cell density (Panel e values = mean + SEM). ****p<0.0001, **p<0.01, *p<0.05

Unilateral hemisphere and regional XCa quantification

Since random XCI and left-right patterning occurs within the same developmental time window during gastrulation (E6.5, and E7.5, respectively) (Kojima et al., 2014; Lee and Bartolomei, 2013), I next sought to understand the dependencies of XCa-choice amongst brain hemispheres. Whole-hemisphere comparisons amongst XCa reporter densities displayed similar maternal bias trends for both hemispheres (24% maternal left bias; U(20) = 30, p = 0.0503; 16% right maternal bias; U(20) = 32, p = 0.0692) (Figure 12). Individual ROI cell density comparisons amongst left or right XCa active and individual ROIs were made using a two-way ANOVA. As with bilateral ROI XCa comparisons, no

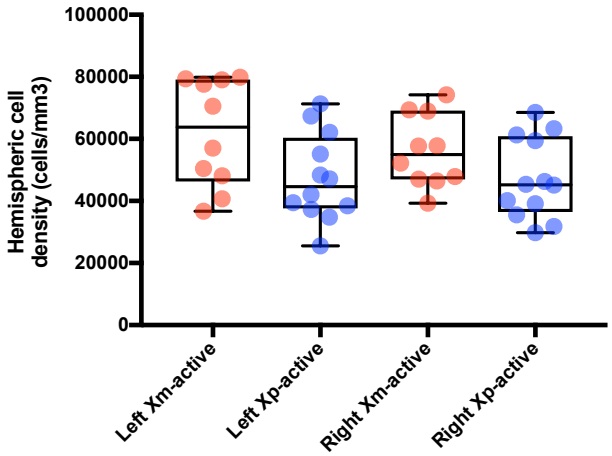

Figure 12. Whole-hemisphere XCa quantification. Box and whisker plots displaying individual sample hemispheric cell density as dots, min/max values as whiskers, and median at line within the box

paternal-biased ROIs were observed (Figure x, c, e). In both left and right hemispheres, a strong main effect of PO XCa was found (left: (F(1, 14820) = 2054, p < 0.0001; right: F(1, 14820) = 1480, p < 0.0001) (Figure 13, d,f) indicating similar maternal XCa preferences for each side. Sidak-corrected multiple comparison post-hoc testing of hemispheric ROI XCa comparisons

found significant unilateral maternal-biases for left (Figure 13, g) and right hemispheres (Figure 13, h). Percent Xm-Xp differences for significant left hemisphere regions were 53% (CNIam), 46% (ORBm2), 32% (PVp), 26% (AOBgr), 22% (MOBmi), 21% (MOBipl), and 16% (islm). For the right sides were 43% (ASO and NC), 39% (AVP), 37% (POST), 36% (PMv), 33% (PVHmpv), 29% (ENTmv3), 27% (SCH), 28% (DMHv), and 26% (PVHmm). All bilateral significant regions (i.e. combined left and right sides) were also significant in unilateral analyses indicating uneven hemispheric influences over bilateral results in these regions. These results suggest the maternal XCa bias persists in both hemispheres of the brain.

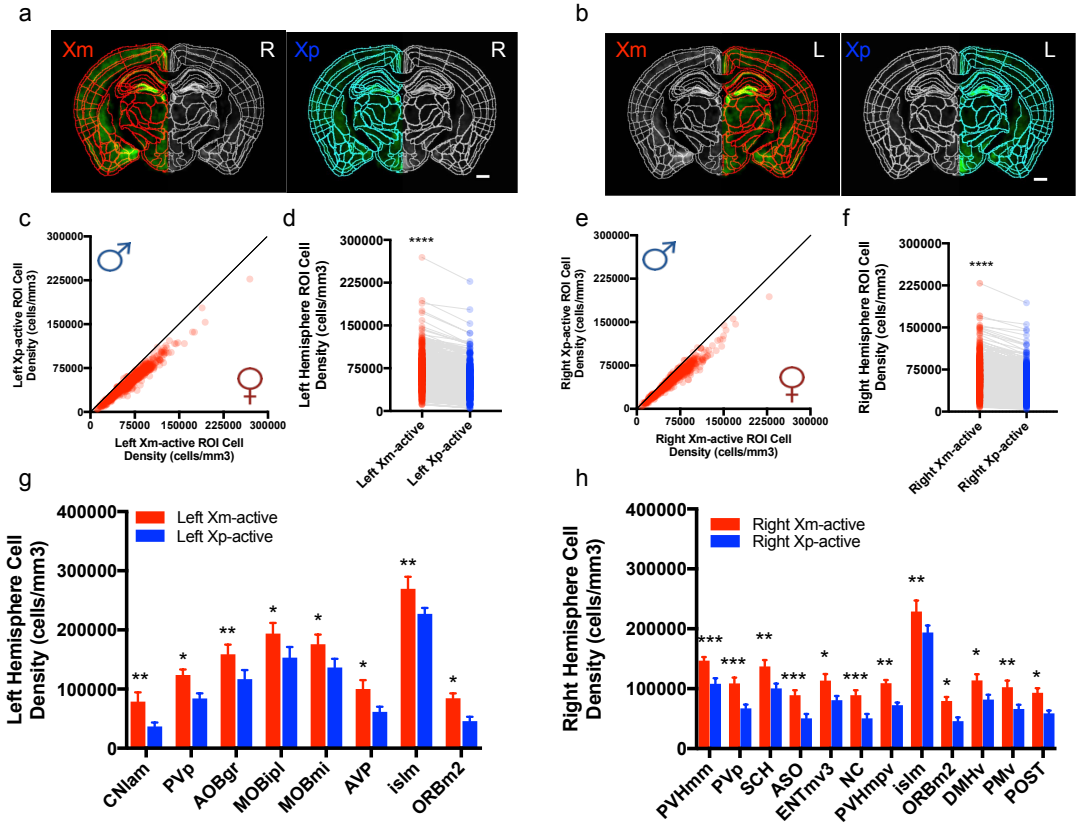

Figure 13. Brain region-segmented XCa quantification amongst hemispheres. a, b) Representative cell count-voxelized coronal images of Xm-active (left) and Xp-active (right) reporting brain with ABA label segmentation skeletonized and

overlaid on each example for a) right and b) left hemispheres (scale bar = 750 um). c) Left and e) right XY scatterplot of mean Xp-active versus Xm-active ROI density values, with a theoretical perfect trendline shown to mark boundaries of ROIs favoring paternal (left) or maternal (right) bias. Main effect summary of PO XCa cell density in d) left and f) right hemispheres, ****p<0.0001. g, h) Significant maternal XCa-biased ROIs identified in Sidak-corrected post-hoc tests for g) left and h) right hemispheres, *p<0.05, **p<0.01, ***p<0.005. CNlam: granular lamina of the cochlear nuclei; PVp: posterior periventricular nuclei; AOBgr: granule layer of the accessory olfactory bulb; MOBipl: inner plexiform layer of the main olfactory bulb; MOBmi: mitral layer of the main olfactory bulb; AVP: anteroventral preoptic nucleus; islm: major island of calleja; ORBm2: medial layer 2 of orbital area; PVHmm: Paraventricular hypothalamic nucleus, magnocellular medial; PVp: posterior periventricular hypothalamic nucleus; SCH: suprachiasmatic nucleus; ASO: accessory supraoptic group; ENTmv3: layer 3 medial ventral entorhinal area; NC: nucleus circularis: PVHmpv: medial ventral parvicelluar paraventricular hypothalamic nucleus, DMHv: ventral dorsomedial hypothalamus; PMv: ventral premammilary nucleus; POST: postsubiculum

Left-right asymmetric quantification

I next asked if left and right hemispheres follow the same XCI bias displayed throughout the whole-brain and regional level. Whole-hemisphere left-right comparisons displayed a trend for left hemisphere biases in Xm-active (9%), Xp-active (1%), and XmXp-active (2%) brains (Figure 14, figure 15, a). Wilcoxon matched-pair signed rank tests did not find these differences to be significant (Xm-active left median: 63802, right median: 54941; W = -37, p=0.0645; Xp-active left median: 44592, right median: 45243; W = -12; p = 0.6772; XmXp-active left median: 100779, right median: 99111; W = -9, p=0.4375). Individual ROI cell density comparisons amongst left and right hemispheres for each genotype were made using a two-way ANOVA. For all genotypes tested, a significant main effect for hemisphere was found (Xm: (F(1, 14820) = 2054, p < 0.0001; Xp: F(1, 16302) = 27.58, p < 0.0001); XmXp: F(1, 13338) = 280.4, p <

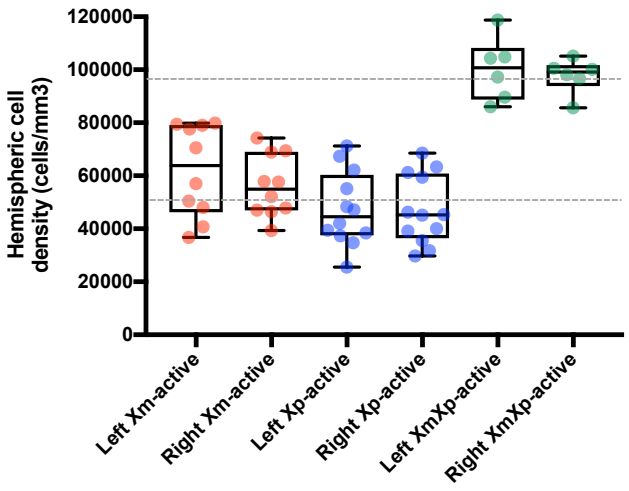

Figure 14. Whole-hemisphere asymmetry comparisons. Box and whisker plots displaying individual sample hemispheric cell density as dots, min/max values as whiskers, and median at line within the box. 100% and 50% control densities based on homozygous means are indicated in dashed lines.

0.0001), indicating an overall pattern of greater cell density in the left hemisphere independent of genotype (Figure 15, c). Sidak-corrected multiple comparison post-hoc testing amongst hemispheric ROIs found significant left and right biases in Xm-active and XmXp-active reporting brains, with left-biased asymmetric ROIs only found in Xp-active brains (Figure 15, d). Accordingly, significant asymmetric left-biased ROIs found in all genotypes included, the subfornical organ (SFO), medial mammillary nucleus, median part (Mmme), and major island of calleja (islm). Significant left-biased ROIs specific to genotype included the following, Xp-active: anterior periventricular nucleus of the hypothalamus (PVa) and subgranular zone of the dentate gyrus (DG-sg); Xm-active: bed nuclei of stria terminals, dorsal (BSTd); XmXp-active: rostral linear nuclei raphe (RL); Xm-active and XmXp-active: Edinger-Westphal nucleus (EW). Significant right-biased ROIs were found only in Xm-active and XmXp-active brains and included the pyramidal layer of field CA2 (CA2sp; both genotypes), and the accessory

supraoptic group (ASO), nucleus circularis (NC), and layer 2 of the ventral retrosplenial cortex (RSPv2) for XmXp-active group only. P-values for all ROIs can be found in Figure 15. In sum, the left hemisphere contains a higher density of cells, regardless of reporter genotype.

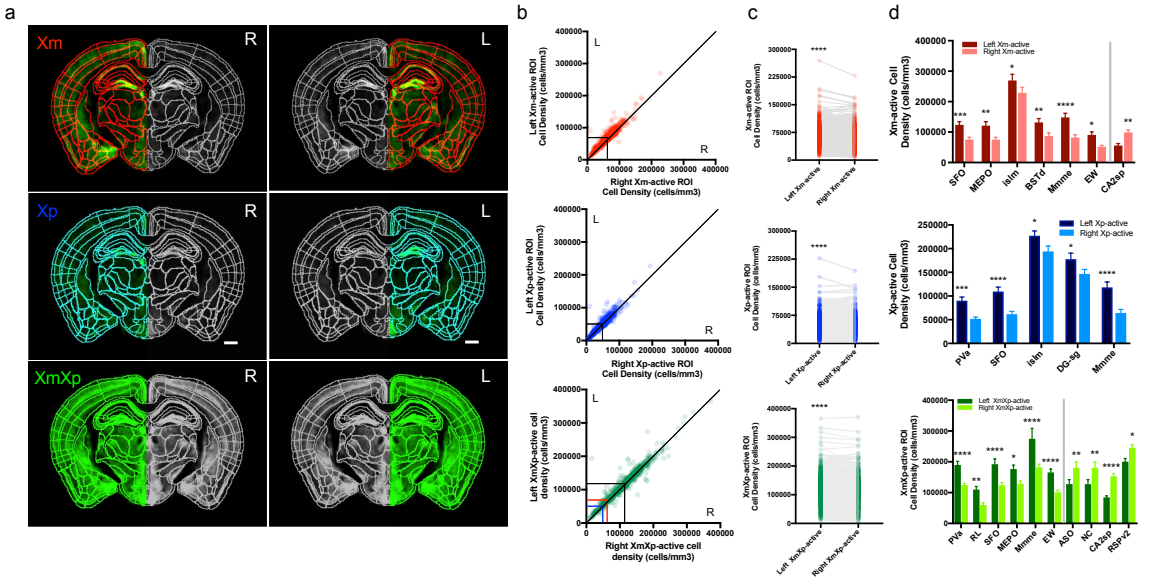

Figure 15. Brain region-segmented left-right asymmetry quantification. a) Representative cell count-voxelized coronal images of Xm-active (top), (middle) Xp-active (bottom) XmXp reporting brains with ABA label segmentation skeletonized and overlaid on each example for right and left hemispheres (scale bar = 750 um). b) XY scatterplot of each genotype plotting left versus right mean cell density overlaid by a perfect linear trendline for comparison. Intersection of boxed lines indicate mean values for each group c) Main effect summary from two-way ANOVA analyses of left-right cell density analyses for each genotype. ****p<0.0001. d) Significant ROIs identified in Sidak-corrected post-hoc tests. ROIs plotted to left of line = left biased ROIs, right of line = right biased ROIs, *p<0.05, **p<0.01, ***p<0.005. ROI abbreviation names are supplied in main text.

XCa quantification in defined cortical cell-types

The brain contains a vast number of neuronal cell types that are derived from different lineages of the neuroectoderm. XCI choice could be affected cell type but has not been previously tested. For this purpose, we next discerned potential cortical neuron XCa effects amongst an excitatory cell sub-type, defined

by FezF2 expression, and an inhibitory subtype, defined by parvalbumin (PV) expression. 2-channel STP-imaged brains for each genotype confirmed robust XCa PO reporting/identification using the MeCP2-GFP allele within both CreER driver lines induced to express tdTomato by Ai14 allelic recombination (Figure 16). FACS quantification in both cell-type/XCa-reporting samples revealed balanced XCI ratios in FezF2 excitatory cells (maternal median XCa 53%, paternal 47%; W = -19; p=0.5305) and PV+ inhibitory cells (maternal median XCa 44%, paternal 56%; W = 36; p=0.3235) (Figure 17,a). Between-group

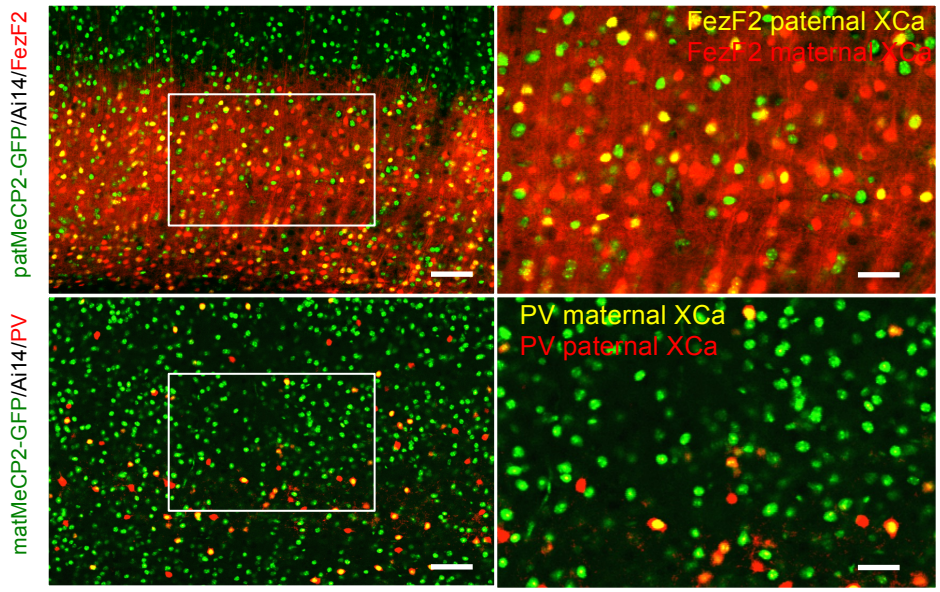

Figure 16. XCa-reporting in defined cortical cell-types. STP-imaged representative example images of paternal and maternal MeCP2-GFP XCa-reporting in Fezf2+ (red; top) and PV+ (red; bottom) neurons, respectively. Example images are cropped from layer 5 of the posterior parietal association area. Scale bars: 50 um, left; 25 um, right.

cell-type comparisons of maternal/paternal XCa showed no differences in cell-type selection of XCa (Figure 17,b). A notable 60% (ns) of all PV-defined samples displayed paternal-XCa biases (Figure 17, c).

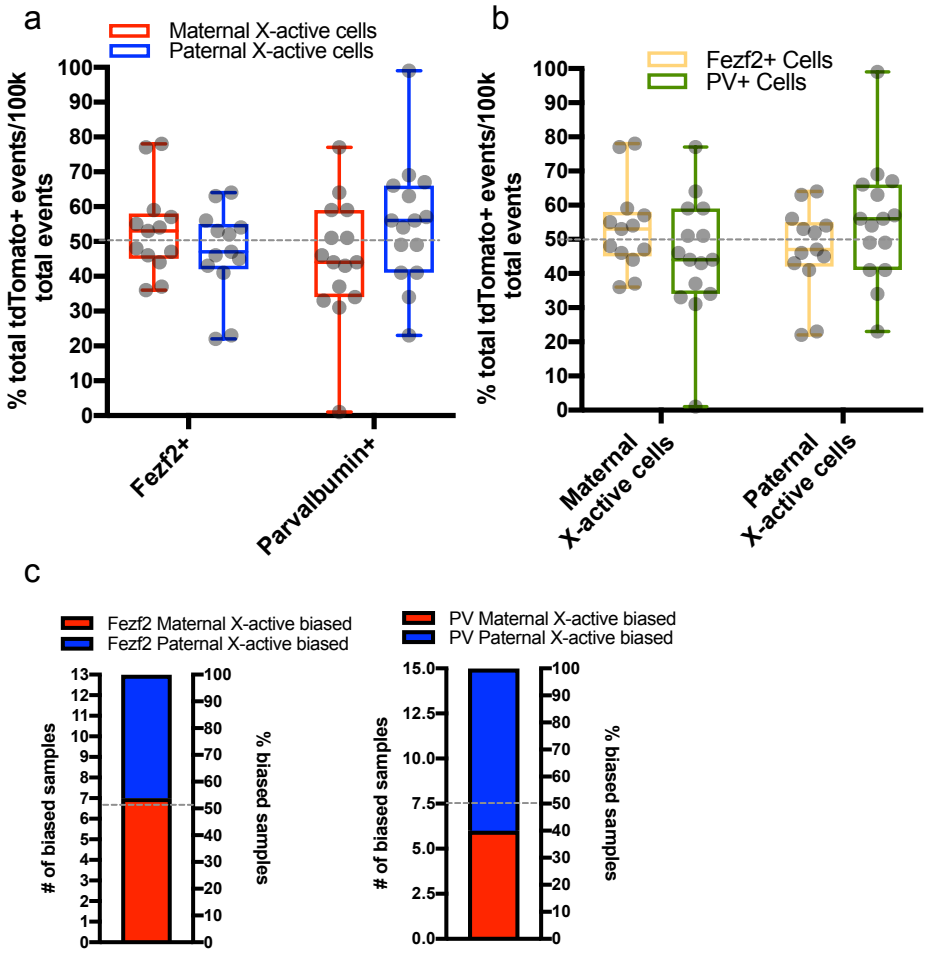

Figure 17. XCI ratio determinations in defined cortical cell-types. % XCa are expressed as % total tdTomato+ events from 100,000 detected events during sorting. a) XCa comparisons amongst cortical cell-types. b) Between cell-type comparisons within chosen XCa c) Classification of samples based on maternal or paternal bias for each cell-type based on % XCa falling below/above theoretical 50% balance of choice. Box and whisker plots display individual sample % XCa values as dots, min/max values as whiskers, and median at line within the box.

4. Discussion

The experiments listed in this chapter describe brain XCI dynamics from a high-resolution cell-counting approach with complete spatial information retained. Overall, our results highlight an approximately 12.5% maternal XC-active bias

that is distributed evenly across all regions and hemispheres. In addition to this average bias, individual XCa status at the organ level was found to predict status of all regions. These results expand the current knowledge of female X-linked gene inheritance patterns of brain expression based on our quantitative descriptions provided.

Previous attempts to discern XCI nature in mouse brain used F1 hybrid-based PO identification followed by analysis of transcription or protein expression ratios (Gregg et al., 2010; McMahon et al., 1983; Wang et al., 2010). These studies reported a small maternal XCa bias of 6-19% using indirect RNAseq and protein measurements. Our direct approach of whole-mount XCa cell counting confirms the previous findings at the single cell resolution level; whereby we also observed an estimated 55% Xm-active/45% Xp-active split in mean XCI ratios. Taken together, we conclude that XCI has a significant, though modest, maternal bias in the mouse brain. Importantly, our dataset provides minimal caveats of XCI ratio derivations that was encountered by the previous studies, such as tissue source sampling effects, cell heterogeneity, and unnormalized cell amounts contributing towards measurements. Furthermore, I am currently working on determining XCI ratios in liver (mesoderm) and heart tissue (endoderm) using FACS of *MeCP2-GFP* heterozygous mice tissue. Thus I expect that my work will provide a comprehensive overview of XCI distribution per all three tissue origins, the neuroderm, mesoderm and ectoderm. These results will importantly reveal if maternal-biased XCa is specific to the brain (i.e. after gastrulation) or all germ layers (i.e. before gastrulation).

Left-right patterning of the embryo occurs close to the time of random XCI onset (E7.5 and E6.5, respectively) (Kojima et al., 2014). It is not known exactly how long XCI takes to complete, however working estimates indicate the time window to be from E6.5 - E9.5. The continuation of XCI into the left-right patterning period is supported by reports examples of full and/or incomplete left-right XCI asymmetries across individual to multiple brain regions (Wu et al., 2014). This supports a hypothesis that the XCI onset continues well into the time of the left-right patterning phase of embryogenesis. Our unilateral analyses revealed the XCa distribution observed for whole-brain and regions is undisturbed across the left-right axis as the maternal XCa bias persisted on both sides. Subtle differences in this bias were seen for some regions in which significance was reached in either left (CNIam, PVp, AOBgr, MOBipl, MOBmi, AVP, islm, ORBm2) or right (PVHmm, SCH, ASO, ENTmv3, NC, PVHmpv, islm, OBRM2, DMHv, PMv, POST) sides. This suggests potential asymmetric left-right influence over Xm expression and regional regulation of behaviors; especially those involved in olfaction and hypothalamic-controlled processes. Regardless of XCa, our left-right analyses also uncovered an overall left-sided bias in cell density. This finding supports human brain estimate data (Marner et al., 2003; Tang et al., 1997) that estimates more cellular density in the left hemisphere, however, the relevance of this in regard to X-linked effects is unclear.

My whole-brain XCI profiling data establishes an organ to regional XCI correspondence implying that lineage or cell-type-specific XCI preferences should not exist. However, the possibility has not been examined before so I

explored this question next within the cortex. Excitatory (glutamatergic) and inhibitory (GABAergic) neurons represent the two major classes of neurons in the cerebral cortex. Within these populations further sub-types exist based on lineage and physiological differences (Butt et al., 2005; Markram et al., 2004; Neske et al., 2015). Our FACS analyses amongst sub-type-specific excitatory (FezF2+) and inhibitory (PV+) cells found balanced XCI ratios in each population. Although not statistically significant, the trends of XCI ratios found are worth mentioning. Similar to our pan-neuronal whole-brain results (55% maternal/45% paternal), FezF2+ populations had a tendency for maternal XC-active preference (53% maternal/47% paternal). In contrast, PV+ cells showed a trend towards paternal preference (45% maternal/55% paternal). Inhibitory neurons comprise 20% of all cortical neurons (Sahara et al., 2012), thereby leaving the remaining 80% presumptive excitatory cells. Therefore, the major class of cortical cells supports the same maternal XC-active bias trend observed whereby the minor class does not, suggesting potential lineage-specific XCI ratio differences. Interestingly, estimate timing of random XCI at E6.5 occurs prior to fate specification of each class of neurons. GABAergic cells are specified from subpallium transcription factor patterning events occurring at E9.5 (Hoerder-Suabedissen and Molnar, 2015) and the first excitatory progenitors arise in the preplate at ~E10.5 (Super et al., 1998). In addition, PV+ interneurons appear first at E13.5 in the medial ganglionic eminence and Fezf2+ cells can be seen as early as E8.5, or the time of neurulation (Hirata et al., 2004). Since the fate-specifying timing events are different across cell-types and lineages, a more

thorough examination of XCI ratios across major classes and other lineages are required to understand the generality of the trends we present. It will be of great interest to examine if chosen XCa affects lineage-specific proliferation or differentiation, potentially explaining ours and other non-random XCa events not analyzed.

Given our result of an approximatelly 12.5% Xm-active bias in mouse brain, it is important to consider the origination and consequences of this attribute. Progressive and complete inactivation of the Xp occurs in mouse development at the 2-cell stage up until embryo implantation (Huynh and Lee, 2003; Lee and Bartolomei, 2013). This effect seems to be guided by repetitive element Xp epigenetic marks remnant from post-meiotic silencing in spermatocytes (Lee and Bartolomei, 2013). After embryo implantation, all cells of the epiblast erase these imprints and transition into “random” XCI 1 day post-implantation (Kojima et al., 2014). Considering our results of preferential inactivation of the paternal XC, incomplete erasure of Xp marks found during pre-implantation could contribute towards the small but favorable inactivation during somatic cell XCI onset. Alternatively, pre-implantation Xp marks are completely erased, but Xp inactivation preference is guided instead during XCi choice through another mechanism. Lastly, another source of bias could be due to pro-proliferation or differentiation effects caused by cis-acting factors or genes of the Xm only. This could lead to favored Xm-active cellular lineages. The existence of Xm-only brain-expressed genes (paternally imprinted XC genes) (Raefski and O'Neill, 2005) supports this possibility, however, our functional understanding of

these genes is very limited. Since all three scenarios remain possible, future efforts are warranted to understand the mechanisms of XCI in more detail.

Finally, random XCI provides an epigenetic mechanism by which parent-specific X-linked traits and mutations are buffered in females in their contribution towards phenotypic outcome. Our results propose that such a buffer contains a slight but potentially functional maternal preference. The XC out-contributes all other chromosomes in its expression of brain function-specific genes (Nguyen and Disteche, 2006) and plays a crucial role in mental functioning (Skuse, 2005). Therefore, Xm or Xp-active cell amounts found in the brain should indicate the phenotypic penetrance of behavioral traits, or brain dysfunction when an XC is diseased. A 5%, or by our measurements, a 2.5 million cell (out of 51 million total cells measurable in the mouse brain) advantage of maternal XC expression may be influential in these characteristics. Several human studies have attempted to characterize the relationship of XCI ratio and behavioral phenotype primarily in diseased states (Alvarez-Mora et al., 2016; Amir et al., 2000; Echevarria et al., 2016; Fieremans et al., 2016; Lossi et al., 1999; Vazna et al., 2010; Winchester et al., 1992). However, XCI determinations in most studies rely on genomic DNA assays from peripherally available cells (e.g. leukocytes, lymphocytes). The translation of peripheral cell XCI findings to that of unmeasured brain tissue remains questionable requiring more validation in different experimental settings (Gibson et al., 2005).

In conclusion, our XCI experiments suggest moderately biased selection of XCa in the brain. In the next chapter, I provide experiments addressing the

extent by which this bias under normal conditions influences brain XCI and behavioral effects in a mouse model of Fragile X syndrome.

Chapter III: XCI influence over phenotypic penetrance in a mouse model of fragile X syndrome

1. Rationale

In the previous chapter I have described brain XCI dynamics from a cell-counting whole-brain perspective. Observations of an ~10% brain-wide maternal XCa bias prompted further investigations into its influence amongst behavioral outcomes in an X-linked disease state. Towards this goal, I chose to study a mouse model of fragile X syndrome (FXS). FXS is the most commonly inherited form of mental retardation (prevalence of 1:2-4000 males; 1:5-8000 females) and is caused by an X-linked monogenic mutation in the gene FMR1 (fragile x mental retardation 1) (Lyons et al., 2015; Rinehart et al., 2011). Loss of the RNA-binding FMR1 gene product, FMRP, leads to a variety of cellular changes relating to ion channel (Ferron et al., 2014; Lee et al., 2011) and synaptic protein translation defects (Chen et al., 2014). I hypothesized that maternal inheritance of the FXS mutation would cause a more prevalent and/or more severe level of penetrance than paternal inheritance. This hypothesis predicts that the maternal-biased XCa brain pattern remains the same in FXS mice as in wild type mice. I further predicted that in either the maternal or paternal inherited case, the percentage of the “diseased cells” with the mutant FMRP allele on the XCa - defined by the XCI

ratios in female brains - should predict the severity of the FXS mouse model phenotype(s).

FXS mouse models present a range of clinically relevant behavioral phenotypes. Well-characterized, strain-dependent phenotypes can broadly be found amongst motor, anxiety, social, memory, sensory, and maintenance behaviors (Kazdoba et al., 2014). It is generally accepted that human FXS phenotypes are sexually dimorphic in that males are more severely affected than females due to XC hemizygosity in males and XCI in females (Marco and Skuse, 2006). Therefore, all male cells will lack FMRP expression whereas roughly half of female cells are spared due to the expression of the healthy FMRP allele in the heterozygous state. In order to observe robust phenotypes in FXS mouse studies, most of the research has been focused on FXS hemizygous males. In one study female homozygous mutant mice were compared against males hemizygous mice (Baker et al., 2010). The authors concluded that there are generally no sex differences in FXS-related behaviors in FMR1 homozygous or hemizygous null mice. However, cases of human FXS in females have only been documented for heterozygous conditions (Nolin et al., 1996).

Clinical studies have described several female FXS cases, with some authors probing the relationship between the disease phenotype and XCI. Inconsistent patient-to-patient outcomes as well as non-specific behavioral features are observed, supporting XCI influence towards variable behavioral outcomes (Marco and Skuse, 2006). As an example, impaired IQ scores below 85 have been reported for 50-70% (de Vries et al., 1996; Visootsak et al., 2005),

85%, (Loesch and Hay, 1988), and as low as 25-28% of study patients examined (Hagerman et al., 1999). Another commonly seen phenotype in females with FXS is an impairment in executive function (planning, attention), which becomes worse with age (Marco and Skuse, 2006). Additionally, phenotypes of increased anxiety, lesser attention, depression, and autistic-like symptoms are often found in female with FXS (Bennetto et al., 2001; Visootsak et al., 2005; Williams et al., 2013; Williams et al., 2014). FXS is also the most common (2%) monogenic cause of autism spectrum disorders (ASD) in male and females combined (Kielinen et al., 2004) and estimates of ASD in female FXS patients is 20% (Clifford et al., 2007). Specific to social contexts, FXS females exhibit anxiety and avoidance (Williams et al., 2014) as well as hyper-reactivity (Williams et al., 2013). This is represented by the high rates of social anxiety disorder (Cordeiro et al., 2011) and avoidant personality disorder (Freund et al., 1993) reported.

In attempts to explain XCI influence in female FXS penetrance researchers have commonly examined the degree by which XCI ratios measured in lymphocytes correlate to the individual patient's behavioral symptoms. Interpretations of this approach's outcomes have been mixed. Chaste et al reported similarly random XCI levels in two FXS sisters with ASD that had a varied levels of intellectual disability (ID) (Chaste et al., 2012). In a similarly designed study focused on FXS sisters, the sibling with higher intellectual disability exhibited skewed XCI suggesting more cells with the mutant allele, whereas the other mildly affected sister showed about equal paternal and maternal XCI (Heine-Suner et al., 2003). Most recently, another sibling study

found that the daughters of an asymptomatic FXS mother had random XCI, whereby the mother had skewed XCI (Stembalska et al., 2016). The authors concluded that the mother's skewing favored inactivation of the mutated allele, lending validity towards the XCI assay used. However, XCI ratios specific to lymphocytic genomic DNA may not be easily translatable to other tissues as other studies cite above did not find a correlation between XCI skewing and disease phenotype. Clearly, XCI determination in the brain is the relevant information to determine the role of XCI skewing in FXS in females. Since this is not possible in humans, an alternative approach may be to determine skin XCI ratios or other tissues derived from the same ectodermal germ layer as the brain.

In the following chapter I present experiments focusing on the influence of brain XCI on the severity of female behavioral phenotypes in heterozygous FXS KO mouse model. I use the same whole-brain cell counting strategy described in the last chapter. In this case, the MeCP2-GFP mouse is crossed into FMR1 KO mutant mice allowing me to track the healthy XCa-GFP+ allele and estimate the diseased XCa counts across the brain in female offspring. Behavioral scoring of anxiety, locomotion, spatial memory, and sociability in individual mice allowed me to determine the correlation between behavioral phenotypes and XCI ratios across all regions of the brain. The aim of these experiments is to provide explanations of female X-linked FXS disease penetrance due to XCI.

2. Materials and Methods

Subjects

Adult double transgenic (MeCP2-GFP+/FMR1 KO or WT) female mice were used for both behavioral and imaging experiments. All animals were housed under a 12-hour light/dark cycle (0600 ON, 1800 OFF), had access to food and water *ad libitum*, and were housed with littermates. FMR1 knockout (KO) mice were obtained from the Jackson laboratory (#003025). These mice were originally developed in the Oostra laboratory and contain a gene-disrupting neomycin resistance cassette in exon 5 of the FMR1 locus (Bakker et al., 1994). The same MeCP2-GFP XCa reporter mice described and used in chapter 2 were used for the FMR1 experiments here also. Mice were maintained on a C57Bl6/J background. Maternal XCa-reporting, paternal FMR1 KO ($Xm^{MeCP2\text{-}GFP}/Xp^{FMR1\ KO}$) female mice were generated by breeding homozygous MeCP2-GFP females with hemizygous FMR1 KO males. For imaging only, $Xm^{MeCP2\text{-}GFP}/Xp^{FMR1\ WT}$ female mice were generated by separately breeding homozygous MeCP2-GFP females with hemizygous FMR1 WT males. Conversely, paternal XCa-reporting, maternal FMR1 KO ($Xm^{FMR1\ KO}/Xp^{MeCP2\text{-}GFP}$) or WT littermate ($Xm^{FMR1\ WT}/Xp^{MeCP2\text{-}GFP}$) female mice were generated by breeding heterozygous FMR1 KO females with hemizygous MeCP2-GFP females. Using this strategy, maternal FMR1 KO mice have the healthy paternal XCa tracked with the MeCP2-GFP allele while paternal KOs have the healthy maternal XCa labeled. Estimated mutant XCa cell density for each genotype is calculated as the difference in healthy heterozygous MeCP2-GFP cell density from mean female MeCP2-GFP homozygous densities acquired in chapter 2 (Estimated mutant XCa cell density = Mean homozygous MeCP2-GFP cell density – measured healthy XCa cell density). All experimental

procedures were performed in accordance with CSHL Animal Care and Use Committee Guidelines.

Behavioral testing

All genotypes of mice were behaviorally phenotyped in a series of tests. $Xm^{FMR1\ WT}/Xp^{MeCP2\text{-}GFP}$ mice were used as behavioral controls for both heterozygous FMR1 KO groups. At least 2 weeks prior to the onset of testing mice were ovariectomized to prevent hormonal influence over behavior. Mice were between the ages of 6-8 months at the start of testing. Each test type was separated by 2-7 days to avoid acute post-testing and handling effects. Aside from 24 hour home cage monitoring (data not shown), the following tests were performed:

Open field test (OFT)

To measure activity and anxiety in an open field, unhabituated mice were placed in a 40 x 40 x 40 cm^2 open plexiglass box containing a layer of fresh bedding. The open field arena was located in a non-sound-proof, enclosed environment under dim lighting. All mice were housed in the same facility room behavioral testing was performed. An overhead camera visually captured all tests and ANY-maze (Stoelting) automated behavior tracking software was used for real-time activity/location recording and analysis. A 20 x 20 cm center square designated within the tracking settings defined the center and perimeter boundaries of the arena. The software measured total and center distance traveled. For center-specific activity – an index of anxiety (Belzung and Griebel, 2001) – center distance was normalized to total distance traveled and presented

as percent total distance traveled. Adequate cleaning of the maze with bleach, water and drying was performed between each mouse. Fresh bedding was used for each subject.

T-maze

We assessed mouse spatial memory by measuring spontaneous spatial alternations in the T-maze (Deacon and Rawlins, 2006; Spowart-Manning and van der Staay, 2004). Spontaneous alternation is an innate exploratory behavior possessed by rodents which is hippocampus-dependent and serves as an index of spatial and working memory (Deacon and Rawlins, 2006). Our protocol was based off of the continuous version with minor modification (Spowart-Manning and van der Staay, 2004). The dimensions of the T-maze used was 35 cm stem length, 28 cm arm length, 10 cm arm height, and 5 cm lane width (Stoelting). For testing, the T-maze was located in a non-sound-proof, enclosed environment under dim lighting. All mice were housed in the same facility room behavioral testing was performed in. To begin the test, each mouse was carefully placed at the stem start position of the maze and was freely allowed to enter either arm. To prevent the mouse from entering the other arm after its initial choice, a metal block was placed at the entrance of the empty arm once the subject committed exploration to an arm. The subjects were allowed to freely explore the chosen arm and stem until it explored back to start of the stem. Once the beginning position was reached, the mouse was held in-between the start position and a metal block placed proximally to the start position for 5 seconds. The metal block was then removed and the mouse was allowed again to enter an arm of its

choice. Manual scoring of each arm choice and time to experimental completion was made after 14 trials. No more than 3 minutes/trial was allowed for each subject and encouragement was given to each subject at 3 minutes (in the form of hand movement behind the mouse) to return to start position. Mice that did not complete more than 9 trials were excluded from analysis. Adequate cleaning of the maze with bleach, water and drying was performed between each mouse. The number of trial-to-trial arm entry alternations (e.g. left-to-right or right-to-left) was calculated and expressed as a percent of total trials.

3-chamber test

Sociability was measured using the 3-chamber test. The 3-chamber apparatus used consisted of a plexiglass box (60 x 40 x 22(h) cm) partitioned into 3 chambers (20 cm/each) (Stoelting). Doors (4 x 8 cm) connecting chambers allowed the mice to freely explore all areas of the box. The apparatus was located in a non-sound-proof, enclosed environment under dim lighting. All mice were housed in the same facility room that behavioral testing was performed in. An overhead camera visually captured all test sessions and ANY-maze (Stoelting) automated behavior tracking software was used for real-time activity/location recording and analysis. Chamber designations in tracking software were user-defined and used for chamber-specific activity measurements. Two metal-barred cylindrical cages (7 cm (diameter) x 15 cm (height); 3 mm bar diameter and 7 mm spacing) were used for stranger mouse containment in one chamber and for an empty enclosure in the opposite-sided chamber. The cage bars are spaced such that close sniffing is the only

interaction type possible. Ovariectomized adult female FMR1 wild-type mice were used as stranger mice and were habituated to an enclosure cage for 10 minutes at least 1 day prior to any experiments. Each stranger mouse (8 total) was used 4 times only and were rotated every 4 experiments for use. Test mice were habituated to an empty 3 chamber apparatus for 10 minutes prior to actual experiments. For testing, mice were allowed to freely explore all chambers for 10 minutes. For each experiment the enclosed stranger mouse was placed in the left chamber and the empty enclosure on the right. Chamber time spent and distance traveled was quantified for each chamber. Percent time spent or distance traveled was calculated as total value/individual chamber value. Sniffing, rearing, and grooming displays were manually recorded and the total time was quantified for each behavior.

Brain processing and whole-brain imaging and processing

All materials and methods of this section are the same as those described in chapter II.

Statistics

Total distance versus center distance traveled in the OFT was compared using a Student paired t-test for each genotype. Between-group comparisons amongst genotypes for total distance traveled, center distance traveled, and percent center distance traveled was analyzed using independent unpaired Student t-tests. Between-group comparisons amongst genotypes for percent

alternation from T-maze testing were compared also using independent unpaired Student t-tests. Percent chamber time spent and percent distance traveled was compared amongst genotypes and chamber using 3 x 3 factor two-way ANOVAs. Significant within-group differences amongst chambers were tested with Tukey post-hoc tests. Significant between-group differences amongst genotypes were tested with Tukey post-hoc tests. Between-group comparisons amongst genotypes for total distance traveled, total sniffing, grooming, and rearing time were statistically compared with independent unpaired Student t-tests. To understand if specific mutant regions or brain systems predict behavioral performance, Pearson's correlations were applied to healthy XCa cell density from 741 ROIs against behavioral scores. Behavioral scores used for correlations were percent center distance traveled (OFT), percent alternation (T-maze), and percent time spent in stranger or center chamber (3-chamber test). Alpha was set at 0.05 for all tests. All statistical testing was performed with Graphpad Prism software version 7.0.

3. Results

The animals used in these experiments were double transgenic females heterozygous for the *FMR1* KO and *MeCP2-GFP* alleles (Figure 18). As in chapter II, XCa cell density determinations were made possible by the *MeCP2-GFP* allele and for these experiments represent the healthy, unmutated XC. Cell density of the other, unmeasured XCa, represents the *FMR1 KO* mutant XC.

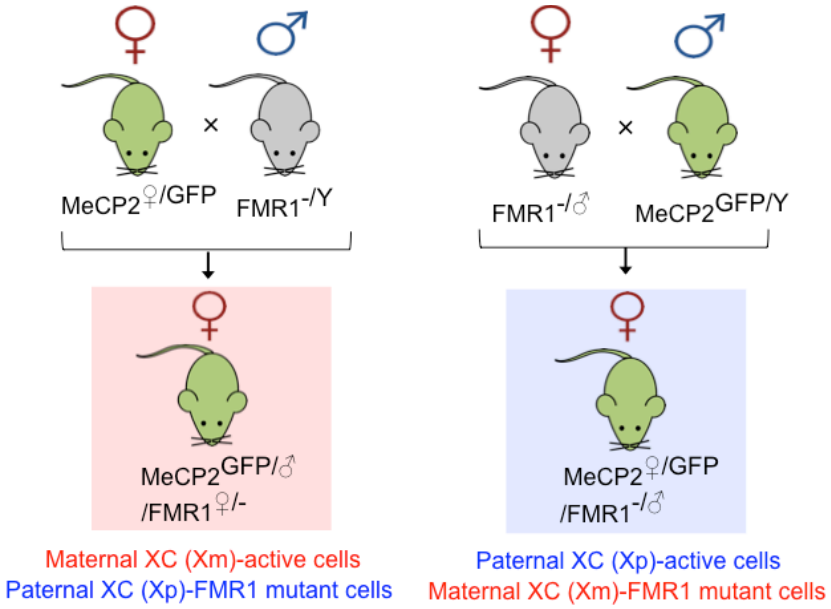

Figure 18: Breeding strategy for PO-specific healthy and FMR1 mutant XCa tracking. Two cohorts of animals were used for behavioral and imaging experiments. XCI cell density ratios were determined in paternal FMR1 KO heterozygotes that contain healthy maternal XCa-reporting cells ($Xm^{MeCP2\text{-}GFP}/Xp^{FMR1\ KO}$; left) and in maternal FMR1 KO heterozygotes that contain healthy paternal XCa-reporting cells ($Xm^{FMR1\ KO}/Xp^{MeCP2\text{-}GFP}$; right).

To assess the correlation between the level of XCI in the brain, and by extension the ratio between the cells expressing healthy and mutant *FMR1* allele, as well as the phenotypes in maternal and paternal KO female mice, I tested the mice in the following tests: open field test, T maze and social interaction in the 3-chamber task test (Figure 19).

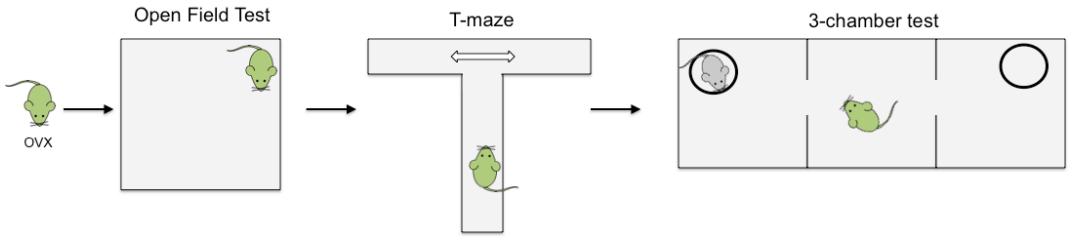

Figure 19: Sequence of behavioral testing performed. All mice were ovariectomized at least 2 weeks prior to open field test used to determine anxiety and activity levels. Subsequently, mice were subjected to the T-maze to measure spatial memory followed by the 3-chamber test of sociability. A subset of these

mice was used for whole-brain imaging experiments. All tests were separated by 2-7 days.

Open Field Test

Motor activity and anxiety levels of $Xm^{MeCP2\text{-}GFP}/Xp^{FMR1\ KO}$ and $Xm^{FMR1\ KO}/Xp^{MeCP2\text{-}GFP}$ mice were determined using the OFT (Figure 20). As a prey species, healthy mice display thigmotaxis, or the tendency to remain close to walls in an open field (Simon et al., 1994). This effect is related to the amount of anxiety mice express when venturing to the center of the OFT area. Pair-wise comparisons of total distance versus center distance traveled indicated a significant tendency for all genotypes to stay along the arena walls (FMR1 WT – total mean: 18.5 m, SD: 6.284; center mean: 2.381 m, SD: 0.9311; $t(8) = 8.792$, $p < 0.0001$; maternal FMR1 KO – total mean: 22.62 m, SD: 9.713; center mean: 2.261m, SD: 1.214; $t(9) = 7.101$, $p<0.0001$; paternal FMR1 KO – total mean: 18.5 m, 6.284; center mean: 2.381 m; SD: 1.074; $t(7)=8.682$, $p<0.0001$) (Figure 20a). Thus, all mice display normal thigmotaxis responses to the open field test. Periphery-specific distance travelled and time spent did not differ amongst groups (data not shown). I next analyzed if activity and anxiety differed amongst genotypes. All genotypes traveled similar total distances (FMR1 WT versus maternal FRM1 KO, $t(17)=1.083$, $p=0.2939$; FMR1 WT versus paternal FMR1 KO, $t(15)=0.3655$, $p=0.7199$; maternal FMR1 KO versus paternal FMR1 KO, $t(16)=0.7496$, $p=0.4643$) (Figure 20b). Additionally, all genotypes traveled similar center distances (FMR1 WT versus maternal FRM1 KO, $t(17)=0.2383$, $p=0.8145$; FMR1 WT versus paternal FMR1 KO, $t(15)=0.001686$, $p=0.9987$; maternal FMR1

KO versus paternal FMR1 KO, t(16)=0.2194, p=0.8291) (Figure 20c). Normalizing the center distance traveled by total distance traveled revealed a significantly lower percent center distance traveled in the maternal FMR1 KO group compared to FMR1 WT group but not paternal FMR1 KOs (maternal FMR1 KO mean: 9.789, SD: 3.748; FMR1 WT mean: 13.08, SD: 2.165; t(17)=2.309, p=0.0338; maternal FMR1 KO versus paternal FMR1 KO (mean: 11.9, SD: 5.183; t(16)=1.003, p=0.3310). Percent center distance traveled did not differ amongst the paternal FMR1 KOs and WT mice (t(15)=0.6294, p=0.5386) (Figure 20d). Overall, maternal and not paternal FMR1 KO mice display potentially heightened anxiety-like behavior in OFT.

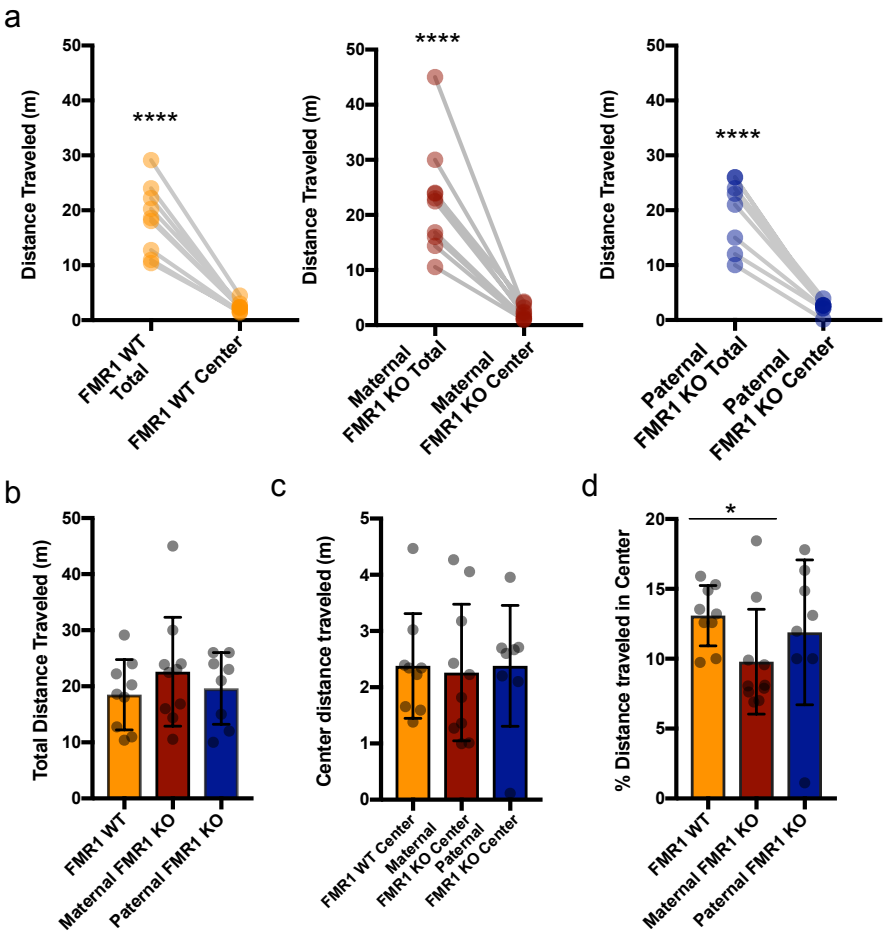

Figure 20: Open field test results of heterozygous female FMR1 ko mice. a) Total distance and center distance traveled compared amongst FMR1 WT (n=8; left), maternal FMR1 KO (n=9; middle), and paternal FMR1 KO (n=8; right) genotypes. Between-subject genotype comparisons for b) total distance traveled, c) center distance traveled, and d) percent center distance traveled from data in b) and c). All bar graphs = mean ± SD with individual data nts shown. *p<0.05; ****p<0.0001

T-maze test of spatial memory

In the T-maze test mice are placed in a T shape arena and given a choice to turn either left or right in 14 consecutive trials. This test represents a measure of spatial memory. As shown in figure 21, maternal (mean – 47.67%, SD – 14.32) but not paternal FMR1 KO (mean – 53.38%, SD – 18.63) mice exhibited significantly lower percent alternations (maternal KO comparison: t(15)=3.033, p=0.0084; paternal KO comparison: t(14)=1.846, p=0.0862) than WT mice (mean – 68.63, SD – 14.11) in the T-maze. Maternal inheritance of FMR1 mutation therefore leads to spatial memory deficits.

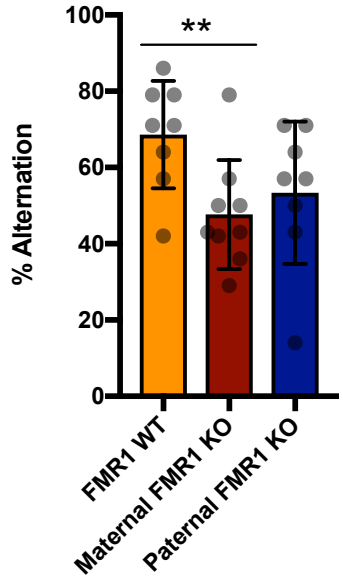

Figure 21: T-maze results of heterozygous female FMR1 ko mice. Percent spatial alternations are compared between FMR1 WT (n=8), maternal FMR1 KO

(n=9), and paternal FMR1 KO (n=8) genotypes. All bar graphs = mean ± SD with individual data nts shown. **p<0.01

3-chamber test of sociability

Finally, to assess differences in sociability amongst the genotypes, the 3-chamber test was employed. In this test, each mouse is freely allowed to explore 3 chambers of a compartmentalized arena. In the left chamber a stranger female mouse is restrained in a cylindrical cage, whereby in the right chamber an empty cylindrical cage is placed. Levels of sociability in experimental mice are determined based on time spent with the stranger mouse. A 3 x 3 two-way ANOVA analysis of percent chamber time — the social chamber, the middle chamber and the empty cage chamber — spent by genotypes revealed a significant chamber main effect ($F(2,66 = 34.31$, $p<0.0001$) and significant chamber by genotype interaction ($F(4,66 = 4.818$, $p=0.0018$). Percent chamber time spent comparisons confirmed a significant post-hoc social chamber preference for FMR1 WT (mean – 47%, SD – 7.4%; versus center chamber (mean – 23%, SD – 3.9%, $p<0.0001$); versus empty chamber (mean – 31%, SD – 7.1%; $p<0.0001$)) and paternal FMR1 KOs (mean – 43%, SD – 6.6%; versus center chamber (mean – 24%, SD – 7%, $p<0.0001$); versus empty chamber (mean – 33%, SD – 8.6%, $p<0.05$)), but not for maternal KO mice (mean – 37%, SD – 7.3%; versus center chamber (mean – 33%, SD – 7.5%, $p=0.3379$); versus empty chamber (mean – 30%, SD – 6.7%, $p<0.0544$)) (Figure 22, a). However, post-hoc genotype testing revealed a significantly reduced social chamber time spent for maternal FMR1 KO mice when compared to FMR1 WT littermates only ($p=0.0233$). Center chamber-specific genotype comparisons showed a

significantly enhanced chamber time spent for maternal FMR1 KO mice versus both FMR1 WT and paternal FMR1 KOs (p=0.0132; p=0.02229, respectively), indicating a lack of maternal FMR1 KO social preference is related to enhanced center chamber occupancy (Figure 22, b). Although neither FMR1 KO groups showed a hyperactive phenotype in the OFT, I next analyzed total distance traveled in the 3-chamber test in order to assess the measure of overall activity in this test. As shown in figure 22c, maternal FMR1 KOs (mean – 20 meters, SD

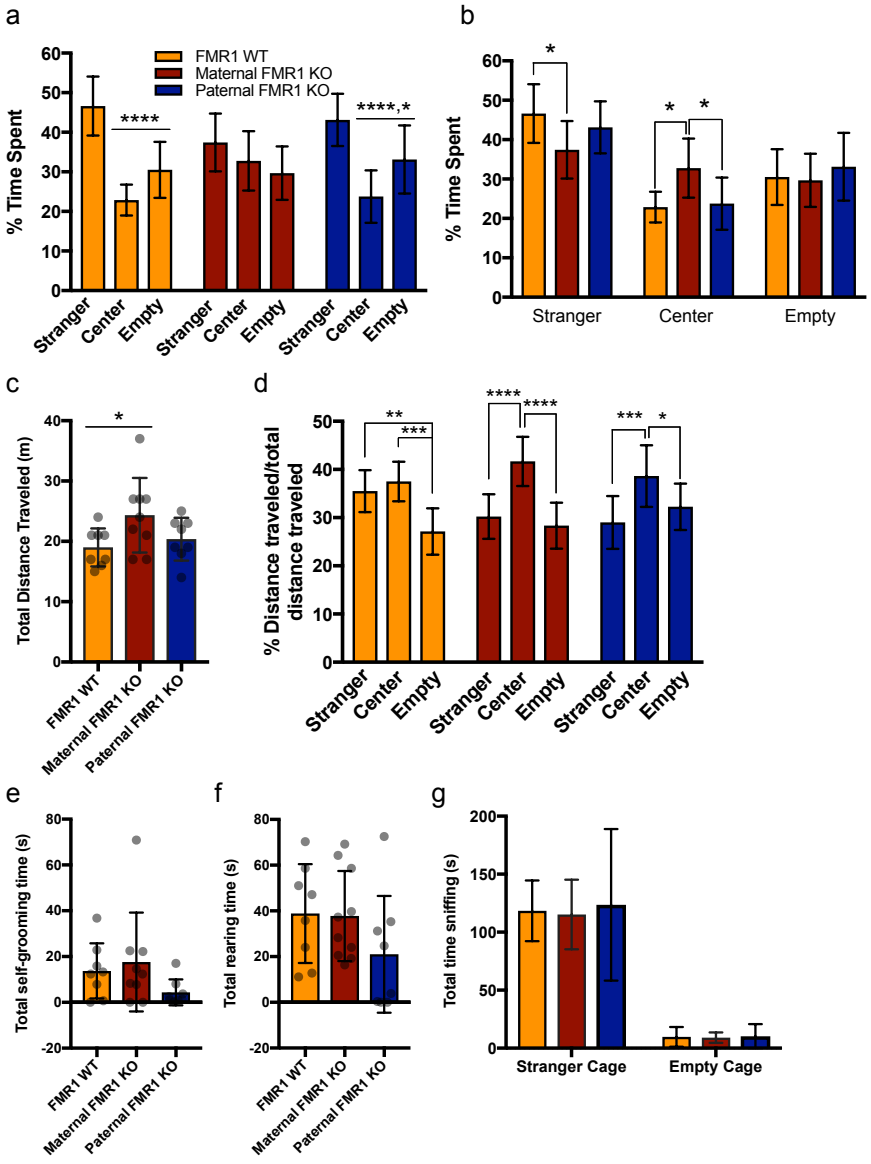

Figure 22: 3-chamber test results of heterozygous female FMR1 ko mice. a) Percent time spent in each chamber amongst FMR1 WT (n=8; left), maternal FMR1 KO (n=9; middle), and paternal FMR1 KO (n=8; right) genotypes. b) Between-subject genotype comparisons for same data in a). c) Total distance traveled and d) percent distance traveled amongst individual chambers across genotypes. e) Total time self-grooming, f) rearing, and g) sniffing at each cage. All bar graphs = mean $\pm$ SD with individual data points shown in c), e), and f). *p<0.05; **p<0.005; ***p<0.001; ****p<0.0001

– 3.5), traveled significantly more than FMR1 WT mice (mean – 19 meters, SD – 3.1; p=0.0445). A 3 (genotype) x 3 (chamber) two-way ANOVA was performed on percent distance traveled to find chamber-specific differences in activity (Figure 22, d). Center chamber distance traveled was highest for all genotypes, with maternal FMR1 KO mice displaying the strongest significant differences amongst other chamber distances (mean – 42%, SD – 5.1%); versus stranger chamber; (mean – 30%, SD – 4.6%, p<0.0001); versus empty chamber (mean – 28%, SD – 4.8%; p<0.0001). Percent center chamber distance traveled was also significantly more than both other chambers for paternal FMR1 KO mice (mean – 39%, SD – 6.4%; versus stranger chamber (mean – 29%, SD – 5.5%, p=0.0007); versus empty chamber (mean – 32%, SD – 4.8%; p<0.0336), but only more than the empty chamber for FMR1 WT mice (mean – 38%, SD – 4.1%; versus empty chamber (mean – 27%, SD – 4.8%; p=0.0003). WT mice also traveled significantly more in the stranger than empty chamber (stranger chamber mean – 36, SD – 4.3; p=0.0036). Therefore, in contrast to OFT data, a novel social context in the 3-chamber task induces hyperactivity. Finally, I also analyzed the time spent in self-grooming during the 3-chamber task. Both maternal and paternal FMR1 mutant groups displayed normal self-grooming and rearing

behavior during the 3-chamber test and also spent a similar amount of time sniffing the stranger mouse and empty cage (Figure 22, e-g). I conclude that maternal FMR1 KO mice display a lower time spent in the social chamber, suggesting a deficit in exploration of a novel social environment. In addition, the maternal FMR1 KO mice display increased locomotor activity in the center chamber, reflecting the increased amount of time spent in this compartment.

Whole-brain XCI in FMR1 mutant mice

In order to be able to correlate the above describe phenotypes in the maternal FMR1 KO mice, I next sought to determine XCI ratios in all heterozygous FMR1 KO mice examined, starting with measurements at the whole-brain level. Mice from the behavioral tests performed (except $Xm^{MeCP2\text{-}GFP}/Xp^{FMR1\ WT}$ group; see methods) were used for whole-brain imaging experiments. As shown in the previous chapter, the maternal XCa-reporting ($Xm^{MeCP2\text{-}GFP}/Xp^{FMR1\ WT}$) brains (median - 6.5 x 10^4 cells/mm^3, SD – 1.3 x 10^4) contained significantly more XCa cells than paternal XCa-reporting $Xm^{FMR1\ WT}/Xp^{MeCP2\text{-}GFP}$ brains (36%; median – 4.5 x 10^4 cells/mm^3, SD – 1.2 x 10^4; U(13) = 7; p = 0.014) (Figure 23, a). This difference persisted in the FMR1 KO comparisons, whereby $Xm^{MeCP2\text{-}GFP}/Xp^{FMR1\ KO}$ mutants (median – 6.6 x 10^4 cells/mm3, SD – 1.3 x 10^4) also showed significantly more XCa-reporting cells than $Xm^{FMR1\ KO}/Xp^{MeCP2\text{-}GFP}$ mutant brains (38%; median – 4.5 x 10^4 cells/mm3, SD – 1.5 x 10^4; p = 0.0379), and I also did not detect any differences amongst the FRM1 KO and the WT MeCP2-GFP comparisons (Figure 23, a; direct comparison not shown). XCa cell density within individual mutant brains were

next normalized by homozygous XCa-reporter brain cell density to visualize whole-brain XCa ratios of healthy and estimated mutant cells. As shown in figure 23b, 6/8 (75%) maternal (left) and 0/8 paternal FMR1 KO brains (right) imaged displayed >50% mutant XCa cell density. Average estimated mutant XCa whole-brain cell densities were 52% in maternal and 35% paternal FMR1 KO – an overall 39% difference. Altogether, these data show that the original maternal XCa bias described in chapter II was replicated in both FMR1 WT and maternal and paternal KO mice in these experiments, replicating the finding of non-random brain XCI. The presence of the FMR1 KO mutation on the XC did not change this bias, consequently leading to significantly more mutant FMR1 cells in maternally-inherited FXS mice. Thus, an increase in the number of mutant FMR1 cells correlates with the presence of the above described behavioral phenotypes in the maternal KO mice.

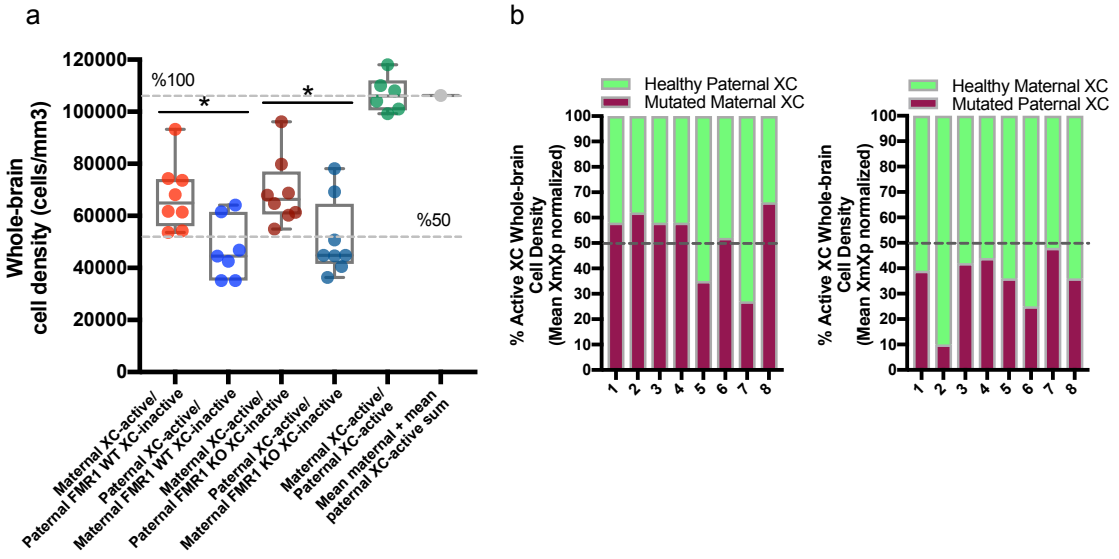

Figure 23: Whole-brain XCI in FMR1 mutant mice. a) Whole-brain cellular density of (from L-R) $Xm^{MeCP2\text{-}GFP}/Xp^{FMR1\ WT}$ (n=8), $Xm^{FMR1\ WT}/Xp^{MeCP2\text{-}GFP}$ (n=7), $Xm^{MeCP2\text{-}GFP}/Xp^{FMR1\ KO}$ (n=8), and $Xm^{FMR1\ KO}/Xp^{MeCP2\text{-}GFP}$ (n=8) mice. For 100% control visual reference, mean $Xm^{MeCP2\text{-}GFP}/Xp^{MeCP2\text{-}GFP}$ reporters and wild-type

heterozygous mean sums are shown to the right. Data is shown as box and whisker plots displaying individual sample values as dots, min/max values as whiskers, and median at line within the interquartile range box. b) Stacked 100% bar graphs of whole-brain XCa cell density values from a), normalized to mean $Xm^{MeCP2\text{-}GFP}/Xp^{MeCP2\text{-}GFP}$ values for maternal (left) and paternal (right) FMR1 KO mice. Percent XCa for each brain is shown as measured healthy XC (green) and estimated mutated XC (purple).

Regional XCI quantification in FMR1 mutant mice

While the analysis at the whole-brain level shows the persistent bias towards the maternal XCa, these data do not address the XCa distribution at the level of individual brain regions, which may have an additional importance for the specific phenotype penetrance in individual animals. For this, whole-brain XCa cell densities were next segmented and determined at the anatomical regional level (i.e. ROI), with the aim to identify intra-brain XCa differences amongst WT and KO mice from each PO. Such differences would indicate an effect, or skewing, of FMR1 mutation on brain XCI. Compared to WT, maternally inherited FMR1 KO brains displayed a modestly greater number of healthy XCa cell density throughout the brain (Figure 24, a). Two-way ANOVA analysis (genotype x ROI) confirmed this as a significant main effect of genotype ($F(1, 9620) = 108.8$, $p<0.0001$) (Figure 24, b). However, post-hoc testing did not identify significant differences at the level of individual ROIs, suggesting that the modest preference for cells with healthy XCa in the maternal FMR1 KO brains is evenly distributed across brain regions. At the same time, paternal transmission of the KO allele did not lead to a noticeable shifting of XCa choice that already favored

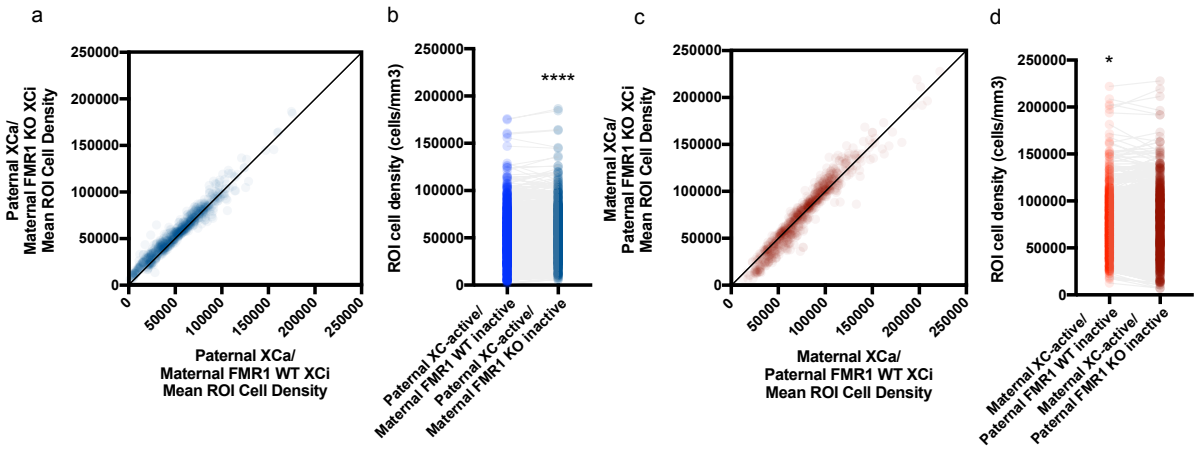

Figure 24: ROI-based XCa skewing analysis in FMR1 mutant mice. a, c) XY scatterplot visualization of mean KO (Y) versus WT (X) XCa ROI density values in a) maternal and c) paternal FMR1 mice. A perfect trendline is shown to mark boundaries of ROIs favoring WT (left) or KO (right) bias. b, d) Genotype main effect results of PO-matched (WT versus KO) 2-way ANOVA for b) maternal and d) paternal FMR1 mice. ****p<0.0001; *p<0.05

the healthy maternal XCa (Figure 24, c). Two-way ANOVA analysis found a significant main effect of genotype, with greater XCa cell density in WT versus paternal KO brains ($F(1, 10360) = 5$, $p=0.0254$). Sidak-corrected ROI post-hoc analysis indicated a single ROI, the parasolitary nucleus (PAS), to have significantly greater XCa cell density in WT (mean – 133192 cells/mm^3, SD – 34213) than KO mice (data not shown; mean – 86291 cells/mm^3, SD – 23456; $p<0.0001$). These results describe potentially opposing and modest PO-effects of FMR1 mutation on brain XCa selection.

Brain XCI neural correlates of behavioral penetrance in FXS mice

I hypothesized next that the penetrance of the FXS behavioral symptoms are influenced by brain XCI state at the level of individual ROIs and I predicted that the variability of XCI within each brain would affect the phenotypic penetrance based on the *amount* and *location* of mutant XCa-containing cells. I

addressed this question by correlating behavioral performance to the distribution of XCI in the segmented whole-brain datasets obtained from FMR1 mutant and wild-type mice. Specifically, Pearson's correlational analysis was performed on individual behavioral scores from each task (OFT – score analyzed: percent center distance traveled; T-maze – score analyzed: percent spatial alternation; 3-chamber – score analyzed: percent time spent in stranger or center chamber spent) amongst healthy XCa cell density across 740 regions. ROIs with high correlation and statistical significance would indicate their involvement over behavioral effects observed. Correlations were compiled for each genotype previously examined (FMR1 WT, n=7; maternal FMR1 KO, n=8; paternal FMR1 KO, n=8). Results of these analyses are visually summarized in figure 25. Heat maps of correlational significance at the level of individual ROIs revealed brain patterning of correlation for the OFT and 3-chamber test and only for the maternal FMR1 KO mice (Figure 25, a). In OFT, the majority (84%) of positive correlations were enriched in thalamic (34% of total significant ROIs) and hindbrain (50% of total significant ROIs) sensory regions (Figure 25, bd). Outside of these areas, the magnocellular nucleus (MA) and nucleus of the diagonal band (NDB) located in the cerebral nuclei showed high correlations, in addition to a single hypothalamic region, the ventrolateral preoptic area (VLPO) (Figure 25, d). Correlations for 3-chamber social task revealed a network of regions involved in object recognition and spatial processing (e.g. lateral visual areas (VISl), medial and lateral entorhinal areas (ENTm/l), as well as anxiety and social coding (e.g. bed nucleus of stria terminalis (BST), basolateral amygdala (BLA), medial

preoptic area (MPO)) (Figure 25, c,e). The 3-chamber correlated ROIs showed no convergence with those of the OFT. In fact, hindbrain and thalamic ROIs composed 50% and 34% total ROIs for OFT and 0 and 2% for 3-chamber, respectively. No cortical or hippocampal ROIs were significantly related to OFT behavior whereas 25 and 23% of ROIs in these areas were related to 3-chamber performance. (Figure 25, b,c). These data suggest the maternal FMR1 mutation-induced behavioral dysfunction is dependent upon the increased distribution of mutated cells amongst putative behavioral circuits. As discussed below, this finding may reflect the broadly varied phenotypes seen in human female patients with FXS.

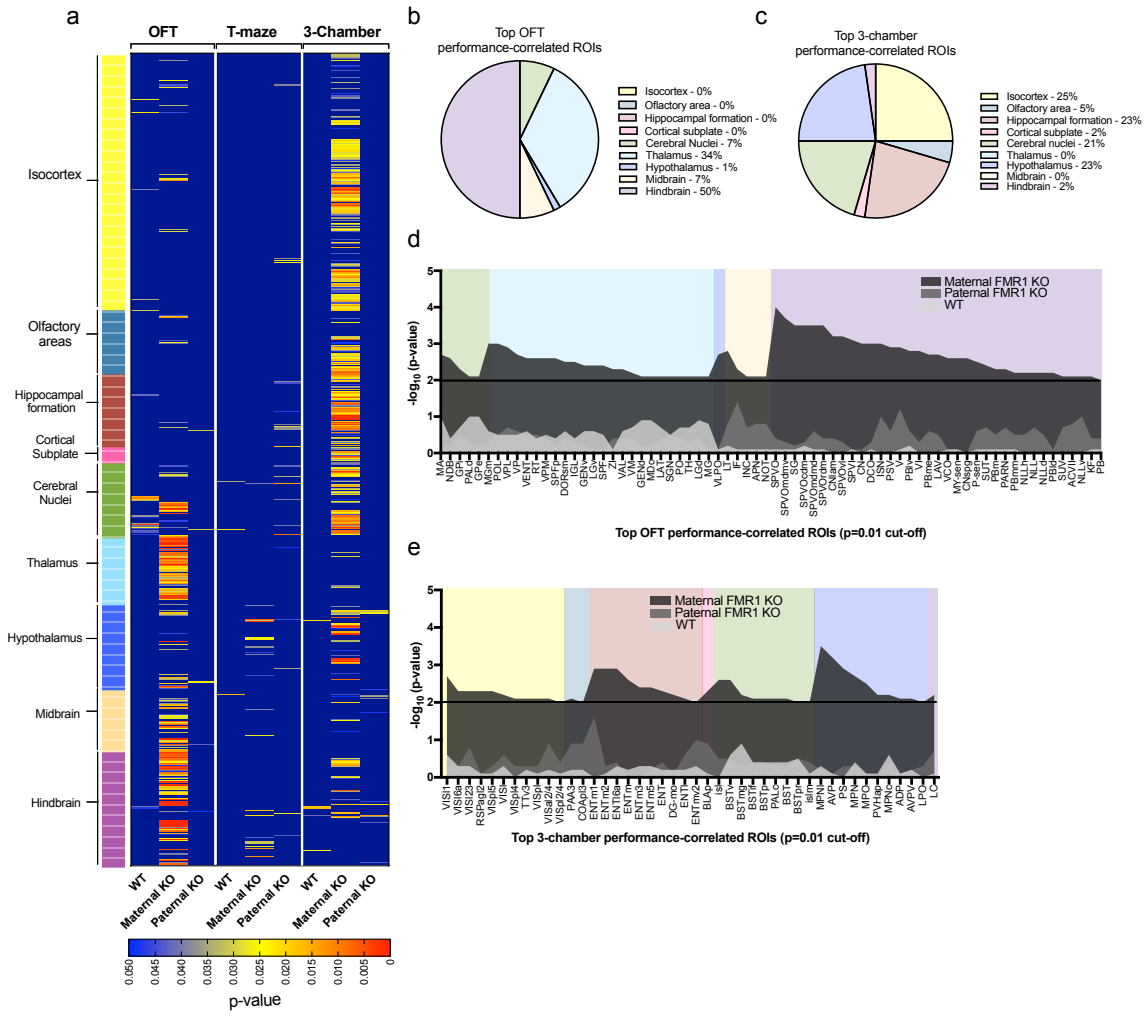

Figure 25: ROI-based correlational screening of XCI-dependent behavioral penetrance. a) Heat maps of correlational p-values listed by ROI healthy XCa cell density (y-axis) obtained from Pearson's correlational analysis amongst behavioral scores (OFT, T-maze, 3-chamber). Results from FMR1 WT, paternal and maternal FMR1 KO mice (x-axis) are grouped by each behavioral test and ROIs are listed in order of major hierarchical brain structures (top to bottom; indicated and color-coded to the left. b) Top (all $p<0.01$) maternal FMR1 KO correlated ROIs found in OFT grouped by major structures and expressed as percentage of total ROIs found. Percentage of significant ROIs/grouping structure is listed to right of pie chart. c) Same as in b) for significant 3-chamber ROIs. d) Significant individual ROIs ($p<0.01$ cut-off; black line) from b) expressed as –log10 transformed p-values. ROIs are listed left to right by grouping structure (color-coded) and in order of p-value (highest to lowest). Transformed p-values of FMR1 WT and paternal FMR1 KO genotypes are overlaid maternal FMR1 KO values for comparison. e) Same as in d) for 3-chamber test ROIs

Lastly, I surveyed significantly correlated ROI's found within OFT and 3-chamber behaviors for connectivity, asking if the regions for each task can collectively be a part of a behavioral circuit. I in-silico screened each ROI amongst each other using Allen Institute's publicly available mouse brain connectivity database. The database provides whole-brain anatomical connectivity results with defined source and target locations for hundreds of injections and mice lines. As the results show in figure 26, a, OFT correlated regions are heavily interconnected. Major sensory hindbrain nuclei connect to many thalamic relay centers. These relay centers are each innervated by the zona incerta (ZI) and a few project to the globus pallidus to inform voluntary movement. NDB connects to the sleep/wake centers, VLPO and MA while also communicating with the sensory-motor related thalamus (DORsm) and the reticular nucleus (RT). A smaller network of connections was observed for 3-chamber correlated ROIs (Figure 26, b). Two major hubs of 3-chamber-related

ROIs can be classified based on known function: spatial navigation and memory/object encoding, as well as social encoding/anxiety (Figure 26, b). The entorhinal cortex (ENT) was found to reciprocally connect with the lateral visual area. Inputs to the ENT consisted of the MPOA and BLA. The BLA sends a cortical projection to the VISl and subcortically projects to the posterior cortical amygdala (COAp) and piriform-amygdala area (PAA). The BST and COAp, both send additional projections to the MPOA. In conclusion, the connectivity amongst ROIs implicated in maternal FMR1 KO penetrance supports an underlying circuit model of female FXS behavioral deficits.

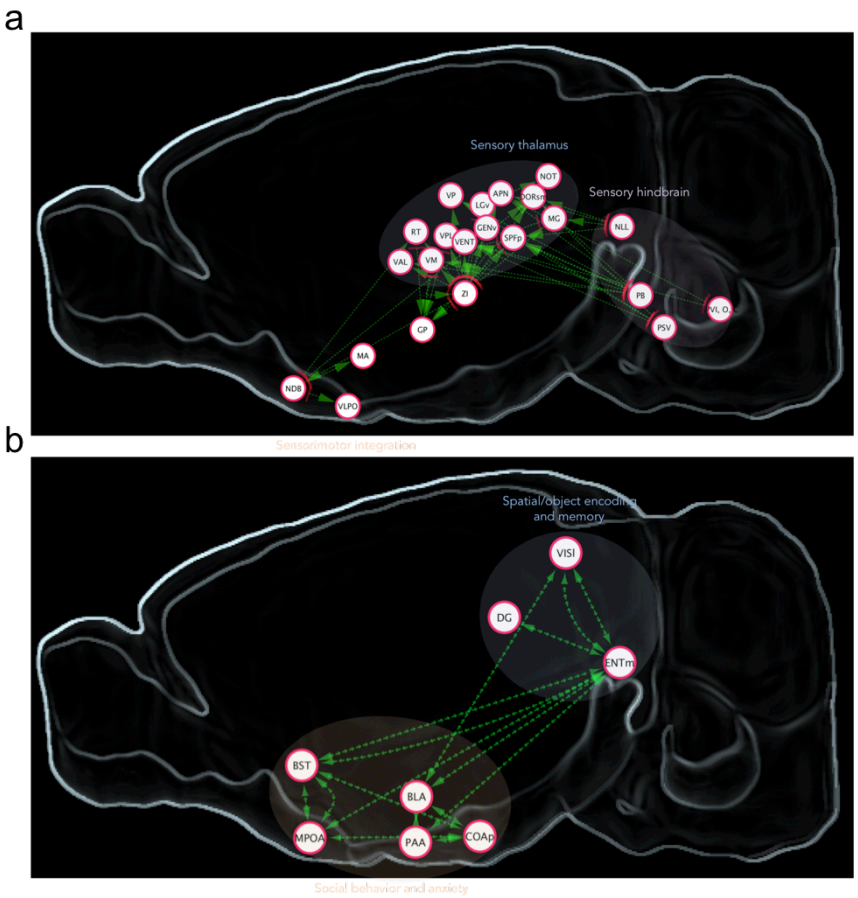

Figure 26. Connectivity summary of significantly correlated ROIs in OFT and 3-chamber tests. a) OFT ROI connections with sensory systems grouped by published function. b) 3-chamber ROI connections with grouping based on published function. See text for more details on compilation.

4. Discussion

Chapter III's experiments aimed to understand the influence of brain XCI on FXS behavioral phenotypes. In summary, I report that maternally biased XCa/paternally biad XCi in the whole-brain persists in female FMR1 mutants that received the mutation from either parent. Female FXS mice displayed penetrance of the maternal X FMR1 KO mutation only, supporting a functional consequence of maternally preferred brain XCa. I also identified putative neural circuits underlying affected exploratory and social behaviors based on XCI distributions at the level of specific brain regions, making future circuit-specific inquiries in FXS possible. Altogether, these results have broad implications regarding the manifestation of female X-linked mental disease based on PO effects at the XC.

The experiments presented in this chapter, to my knowledge, report the first behavioral study of heterozygous FXS female mice. Human FXS syndrome in females occurs only in heterozygous conditions with preferential maternal transmission (Loesch and Hay, 1988; Loesch et al., 1987; Zeesman et al., 2004). The study by Baker et al also investigated female FXS mice behaviors, however the mice were homozygous and data was combined with hemizygous males (Baker et al., 2010). Their results described spatial memory deficits in male/female FMR1 null mice agreeing here with my results from the maternal KO FMR1 heterozygous mice. Although the correlation between ROI cell count and spatial memory score analyses failed to identify specific brain regions

contributing to the behavioral phenotype, the similarity between the maternal KO and null mice likely relates to the increased number of mutated XCa in the maternally inherited heterozygous mice. Thus, the estimate of approximately 39% greater mutated XCa cell density in the maternal KO whole-brain (compared to WT) may reflect a threshold for FXS penetrance not reached in the paternal cases.

Regarding the relationship between brain regions and other phenotypes in male FXS mouse studies, experiments utilizing local recombinant expression of FMRP support the link amongst mutant cell number, their location, and behavior. Gholizadeh and colleagues reversed a repetitive behavior phenotype using AAV-driven FMRP expression via intracerebroventricular (ICV) injection at P5 (Gholizadeh et al., 2014). They reported that re-expression of FMRP protein in ~50% of cells in the hippocampus, retrosplenial and cingulate cortex was sufficient for correction of the pathological behavior. Additionally, a subsequent study showed a rescue of motor, anxiety, and sensorimotor responses using the same ICV AAV-FMRP approach (Arsenault et al., 2016). The authors used different promoters to drive AAV-FMRP at different levels which either rescued or exacerbated symptoms based on physiological or supraphysiological FMRP levels achieved, respectively. These studies thus agree with my present findings in which maternal FMR1 KO inheritance leads to an estimated average of 52% whole-brain cells with FMRP loss, resulting in a phenotypic penetrance. Conversely, preferential inactivation of the paternal FMR1 mutation limits whole-

brain FMRP loss to a 35% estimation of cells and the behaviors studied remaining unaffected.

Beyond spatial memory, phenotypic penetrance of the maternal FMR1 mutation was also observed in the OFT, an assay of motor activity and exploratory behavior. Exploration of the center space in an open field is considered to be related to anxiety; the more time explored, the less anxiety a mice has (Gould et al., 2001). Maternal KO mice traveled less in the center (when normalized to total distance traveled) than WT littermates indicating less exploratory drive possibly relating to higher levels of anxiety. Total distance traveled in the OFT was not different amongst groups indicating no major differences in arousal states or locomotion. Likewise, no differences were observed in distance traveled or time spent in the periphery (data not shown). Correlative analyses of healthy cell density and center distance traveled identified a potential network of brain regions involved in this effect, however, it failed to identify known components of an anxiety-regulating network (e.g. BST, several amygdala nuclei, periaqueductal grey (PAG), etc.) (Tovote et al., 2015). Instead, percent center time traveled positively correlated with healthy cell amount in subcortical regions collectively involved in sensorimotor (e.g. several sensory thalamic nuclei, the sensory pons and medulla, globus pallidus) and arousal (e.g. MA, VLPO, reticular nucleus (RT), zona incerta (ZI)) control. The nucleus of the diagonal band (NDB), the primary region responsible for theta oscillations – specific hippocampal activity underlying spatial cognition, exploratory behavior and sensorimotor integration (Bland and Oddie, 2001;

Buzsaki, 2002) – was importantly another top region in the basal forebrain correlated with center space exploration. These ROI functional classifications were matched with connectivity patterns derived from the Allen Brain Connectivity database that linked the identified ROIs onto putative behavioral circuit models for center exploration. Therefore, reductions in center distance traveled in maternal FMR1 KO mice can be interpreted as a circuit-based dysfunction in sensorimotor and arousal integration underlying exploratory behavior. Sensorimotor gating abnormalities in FXS patients and mice have been documented further supporting the current findings (Frankland et al., 2004; Nielsen et al., 2002).

In addition to anxiety and hyper reactivity, human female patients with maternal heterozygous loss of FMR1 also display avoidance to social contexts (Williams et al., 2013; Williams et al., 2014) and they account for ~20% of ASD females (Clifford et al., 2007). My experiments show that the maternal FMR1 mutant heterozygous female mice display also a social phenotype measured in the standard 3-chamber social task. The maternal but not the paternal mutant heterozygous mice showed a significantly reduced time spent in the social chamber and this effect was largely due to an increased time spent in the middle chamber. In addition these mice showed increased distance traveled/hyper reactivity in the middle chamber. These findings suggest that the maternal FMR1 mutants exhibit hyper reactivity/arousal coupled with social avoidance in the 3-chamber social task. Therefore, this behavioral dysfunction in the FXS mouse model seems to phenocopy human female's FXS patterns of social deficits well.

My results also parallel those made in the male FMR1 null mouse, in which males displayed social anxiety upon initial interaction with unrestrained stranger mice (Spencer et al., 2005).

As with the other behaviors tested, social behavior is subject to maternal FMR1 mutation penetrance likely due to biased maternal XCa in the brain. Maternal mutant mice spent abnormally more time occupying and traveling within the center chamber, avoiding the occupancy in the social chamber as well as in the opposite control chamber with an empty cup. This avoidant behavior was correlated across the brain with healthy XCa cell density to identify regions and circuits that may be responsible for this effect. Negative correlation to the time spent in the center chamber, i.e. an effect when more mutant XCa cell density correlates to the time spent in the center chamber, identified a network of regions classified into two nodes of function: 1) spatial navigation and memory/object recognition, and 2) social interaction/anxiety. Connectivity amongst the two nodes indicated functional integration for spatio-social involvement, aligning well with the disturbance in the 3-chamber social behaviors. Specifically, the entorhinal cortex (ENT; mainly medial) was found to reciprocally connect with the lateral visual area, both essential in spatial and object encoding (Fyhn et al., 2004; Wang et al., 2012). Inputs to the ENT consisted of the MPOA, a center for social interaction (McHenry et al., 2017), and the BLA, a center involved in fear/anxiety (Tovote et al., 2015). The BLA sends a cortical projection to the VISl and subcortically projects to the posterior cortical amygdala (COAp) and piriform-amygdala area (PAA). The BST, another anxiety and social component (Bayless

and Shah, 2016) as well as the COAp, an upstream social-guiding (Kim et al., 2015) nucleus additionally project to the MPOA. Taken together, this suggests female FXS penetrance in social behaviors may rely on the number of mutant XCa cells specifically in these behavioral circuits. My ongoing experiments are aimed at testing the causal roles of these regions by functionally manipulating the nodes of this circuit during social behavior in wild type mice. In addition, I also aim to attempt to rescue the social behavior phenotype in the maternal mutant FXS mice by recombinant FMRP expression targeted to mutant cells of the MPOA specifically.

In conclusion, by using FXS as a proxy for other female X-linked syndromes, I have described the functional influence of brain XCI in regulating female X-linked disease states. My data indicate that biased maternal XCa programs for more maternal X-linked mutant cells compared to when the same mutation is transmitted from father. Importantly, my data also suggest that this penetrance is dependent on the XCI distribution within the brain's anatomical areas, such as the deficit related to hyper activity when more cells with mutant XCa are found in the areas of sensory thalamus and hindbrain, or the deficit in social behavior when more cells with mutant XCa are found in the hippocampus, cortex and hypothalamus. This XCa brain area-dependent phenotypic penetrance may reflect the broad and varied range of phenotypes observed in female patients with heterozygous mutation passed from the mother.

Chapter IV: Identification and investigation of imprinted *Grb10*-defined neural circuits

1. Rationale

Imprinting of dosage-sensitive genes may is proposed to shape neural circuit activity underlying specific behaviors (Isles et al., 2006; Wilkinson et al., 2007). Examples of such behaviors include mother and pup socialization controlled by imprinted *Peg1* and *Peg3*, or *Gnas* and *Gnasxl* regulation of communal care (Ubeda and Gardner, 2011). Growth factor receptor-binding protein 10 (*Grb10)* is also an imprinted gene that is proposed to regulate social behavior, specifically in the context of social dominance (Garfield et al., 2011). This hypothesis is based on a study demonstrating that adult *Grb10* paternal knockout mouse shows dominant behavior toward wild type mice, including barbering and dominance in a forced encounter behavioral test. Using *LacZ*-based reporting from the disrupted *Grb10* allele, expression was seen in broad populations within the midbrain, hindbrain, and hypothalamus. Intriguingly, paternal *Grb10* knockout mice behaved similarly as wild-type littermate controls in several other assays testing anxiety-related behavior, locomotor activity, olfaction, aggression, and social recognition. It is therefore plausible that the broad *Grb10* expression patterns amongst distinct brain regions underlie a circuit controlling social hierarchy and dominance. Alternatively, individual expression

nodes of *Grb10* may define and regulate additional behaviors, but these were not identified using the germline knockout approach in which the organism may developmentally compensate for at least some functions of the Grb10 paternal allele.

The evidence listed from the aforementioned studies suggests that the control of specific behavioral circuits is coordinated by the actions of imprinted alleles in appropriate brain systems. To directly test this hypothesis, I have chosen to study how the allele-specific expression, connectivity, and activity of imprinted *Grb10* neurons regulates behavioral functions through a non-disruptive genetic strategy. To this end I have generated novel Grb10 parent of origin reporter mouse lines and used STPT and confocal microscopy to characterize genetically defined maternal and paternal *Grb10* expression marked by two color marker genes—GFP and tdTomato. In addition, driven by the tdTomato reporter allele, Cre recombinase expression allowed me to characterize connectivity and manipulate the activity of a novel biallelic *Grb10*-expressing neuronal population during behavior. These data thus address the putative role neuronal circuits marked by *Grb10* genomic imprinting in behavior without disrupting the *Grb10* gene function.

2. Materials and Methods

Subjects

Adult male mice (8-12 weeks old) were used for all experiments. Animals were housed under a 12-hour light/dark cycle (0600 ON, 1800 OFF), had access to food and water *ad libitum*, and were housed with littermates. All experimental

procedures were performed in accordance with CSHL Animal Care and Use Committee Guidelines. Mice were maintained on a C57Bl6/J background. *VIP-IRES-Cre* (here called VIP-Cre) mice used for tracing experiments were developed in the Huang laboratory (Taniguchi et al., 2011) and obtained from Jackson laboratory (Stock #: 010908). *GAD2-2A-nls-mCherry* mice used for colocalization studies were developed in the Svoboda lab (Peron et al., 2015) and were also obtained from the Jackson laboratory (Stock #: 023140)

Grb10 allelic reporter and Cre-driver mouse line generation

A novel fluorescent protein-based strategy was created to visualize single cells containing PO-specific monoallelic or biallelic Grb10 expression in mouse brain. For this, P2A-H2B-Venus or H2B-tdTomato cassette insertion into the 3' *Grb10* locus was chosen for discriminately reporting PO allelic expression. The H2B-fluorescent protein (FP) cassettes are designed to read in frame with the endogenous *Grb10* gene by replacing the stop codon of the last coding exon. The P2A peptide's "self-cleaving" ability serves for reliable, bicistronic expression of the reporter FP in a non-disruptive manner after the endogenous *Grb10* protein (Tang et al., 2009). Of the 2A peptide variants, P2A was chosen due to its high self-processing efficiency (Kim et al., 2011). I additionally incorporated a glycine-serine-glycine linker immediately upstream of the P2A sequence in order to facilitate the most optimum self-processing (Szymczak-Workman et al., 2012). To discriminate single-cell signals in mouse brain, histone 2B (H2B) sequence was fused with the FP to direct it's trafficking strictly to the nucleus. To allow

conditional viral tracing and activity studies, another 2A peptide, *Thosea asigna* virus 2A (T2A) was added to the tdTomato reporter mice to allow tricistronic expression of the *Grb10* allele, tdTomato, and iCre. Therefore, the parental allele reporting tdTomato will also express iCre. The iCre gene is a codon-optimized version of Cre recombinase engineered for maximal Cre expression and recombination in mammalian systems (Shimshek et al., 2002).

Grb10^{P2A}H2B-Venus, Grb10^{P2A}H2B-tdTomato, and Grb10^{P2A}H2B-tdTomato^{T2A}iCre gene-targeting construct designs were identical aside from reporter sequence and the ^{T2A}iCre addition. Accordingly, the ~5 kb and ~3 kb of the Grb10 genomic sequence upstream and downstream, respectively, of the stop codon within the last coding exon of *Grb10* gene was PCR-amplified from commercially available BAC DNA (BAC clone # RP24-121C11). These arms of homology were cloned into a PL450 gene-targeting vector. An Frt-flanked neomycin cassette separates the arms and was used for downstream positive selection of successfully recombined stem cells. An additional thymidine kinase cassette is located directly 3' of the arms for negative selection screening. Overlapping PCR was used to generate ^{P2A}H2B-Venus or ^{P2A}H2B-tdTomato^{T2A}iCre cassettes in frame with the C-terminus of Grb10. The finalized vectors were linearized through unique digestion outside of the arms of homology in preparation for gene targeting in embryonic stem cells (ESCs). The CSHL gene targeting facility performed standard methods of homologous DNA recombination in F1 hybrid 129 agouti/B6 ESCs. After targeted DNA electroporation, ESC clones surviving selection were screened 5' and 3' of the

targeted allele for correct recombination by PCR and 3' for southern blot. Screening primer sequences used are as follows: 5' primer pair: Forward - caatggtttgagggctgttt, reverse – ggggaacttcctgactaggg; 3' primer pair: forward – tcgccttcttgacgagttct, reverse – tgtcattccccaggtgctat; 3' probe primer pair: forward – ctacccctgtcacctgcaat, reverse – tcccacatgtgctgttttgt. Two correctly recombined clones/line were expanded and used for B6 blastocyst injections for implantation into pseudo-pregnant surrogate mothers. F0 and F1 mice were PCR screened and validated for the presence of knock-in alleles from mouse-tail genomic DNA. The same PCR primers and southern blot probes designed for ESC screening were used for F0 and F1 mouse allele screening. F1 mice harboring the knock-in allele were backcrossed to Flp-deleter mice in order to remove genomic neomycin selection cassettes. Successful deletion of neomycin cassettes were screened with primers: forward: caaaggcgttcgtactgaca, reverse – gcacaacaacaacgatgacc. Finally, neo-deleted mice of knock-in lines were successfully backcrossed into C57Bl6/J background for 5 generations.

Brain processing, whole-brain imaging and downstream processing

All other materials and methods of this section are the same as those described in chapter II with some modification. Accordingly, transformed voxelized cell counts from separately processed paternal and maternal *Grb10*^{P2A}*H2B-Venus* adult male heterozygous reporter brains were used for figure 30. Voxelized stacks from each brain were merged and overlaid on a reference brain stack for contrast. Adult male paternal *Grb10*^{P2A}*H2B-Venus*

brains (n=2) were used for mean whole-brain cell density determinations. Unlike chapter II, densities here are derived from uncorrected 50 um Z cell count resolution. All STPT and computational configurations used in chapter II were repeated for this chapter.

Immunostaining and confocal microscopy

Cell-type identification and characterization of paternal and maternal *Grb10*-expressing cells was performed on individual *Grb10*$^{♀H2B\text{-}tdTomato/♂H2B\text{-}Venus}$ or *Grb10*$^{♀H2B\text{-}Venuso/♂H2B\text{-}tdTomato}$ dual-reporting adult male brains. The same NeuN labeling protocol described in chapter II was used here. Grb10 (abcam; ab125583) antibody was used at 1:100 dilution for expression validation with chapter II's immunostaining protocol. The following primary antibodies and dilutions for neuron subtype identification in biallelic vlPAG neurons were also used with the same staining protocol used in chapter II: 5-HT (1:500; Immunostar, 20080), ChAT (1:500; Santa Cruz Biotechnology, 20672), VIP (1:400; Immunostar, 20077). For glutamate (1:500; Immunostar, 22523) staining only, perfusion fixative was modified to contain 1% glutaraldehyde for detection enhancement.

Stereology

50 um thick vibratome sections from two adult male *GAD2-2A-NLS-mCherry/matGrb10-H2B-Venus* mice were prepared for vlPAG colocalization

studies. Section collection began at -3.27 bregma in the anterior PAG and ended at -5.07 bregma. 3-channel confocal images were acquired for every 200 um in the Z plane under a 20x oil-immersed objective. Cellular quantification was performed using Fiji image analysis software (NIH). The Paxinos and Franklin mouse atlas (2012) was used as guidance for manual v/vlPAG segmentation. Within the segmentation of every image, VIP+ cells were counted manually and matGrb10+ and GAD2+ nuclei counted semi-automatically. For the automation, segmented images were threshholded using the embedded Otsu algorithm and all cells above 10 um in size were detected using the 3D objects counter. Total cells counted from all sections were then divided by total tissue thickness imaged (e.g. 300 um) to arrive at cells/mm3. Colocalized cells were detected using the AND math calculator function off of thresholded images and counted with the analyze particles function.

Adeno-associated virus (AAV) stereotaxic injections

Stereotaxic injections of adeno-associated virus (AAV) were performed using the methods of Cetin et al (Cetin et al., 2006). Ventrolateral PAG (vlPAG) stereotaxic brain coordinates (as defined by Paxinos and Franklin, 2012) used for maternal *Grb10-H2B-tdTomato-iCre* anterograde, retrograde, and loss-of-function experiments were -4.71 anterior/posterior, 0.4 medial/lateral, 2.75 dorsal/ventral. Coordinates used for *VIP-Cre* tracing were -4.50 anterior/posterior, 0.25 medial/lateral, and 2.65 dorsal/ventral. AAVs used that were obtained through the UNC viral core included AAV9-CAG-FLEX-EGFP,

AAV8-CAG-EGFP, AAV8-CAG-FLEX-tdTomato, AAV8-CA-FLEX-RG, AAV8-EF1a-FLEX-TVAmCherry, and AAV1-FLEX-taCasp3-TEVp. AAV8-hSyn-DIO-hM4D(Gi)-mCherry was purchased through Addgene (#44362). G-deleted, EnvA-pseudotyped, EGFP-expressing rabies virus for retrograde input mapping was made by the Gene Transfer, Targeting and Therapeutics Core (GT3) at Salk Institute. Pressure injected viral volumes used for each AAV as well as incubation time prior to euthanization or behavioral testing was dependent on experiment as indicated: 0.1 ul unilateral AAV-CAG-FLEX-EGFP (2 weeks); 0.2 ul unilateral AAV-CAG-FLEX-tdTomato: AAV-CAG-EGFP coinjection mix (5:1) (2 weeks); 0.2 ul unilateral AAV8-CA-FLEX-RG: AAV8-EF1a-FLEX-TVAmCherry (3:1) (4 weeks); 0.25 ul bilateral AAV1-FLEX-taCasp3-TEVp (2 weeks) and AAV8-hSyn-DIO-hM4D(Gi)-mCherry (4 weeks). 0.25 ul unilateral rabies virus was used for input mapping with an incubation time of 1 week.

Maternal Grb10-H2B-tdtomato-iCre v/vlPAG anterograde tracing

Anterograde projections were visualized by STPT microscopy. Main areas of projection sites were found by systematic visual inspection of STPT raw datasets of 1 um Y x 1 um X x 50 um Z resolution.

BNST axon terminal quantification

VIP-Cre v/vlPAG projections in the bed nucleus of stria terminalis (BNST) were analyzed in Fiji. All brains (n=3) were imaged in 2-channels via STPT at 1 um Y x 1 um X x 50 um Z resolution. Intra-BNST terminal specificity was

calculated from manually segmented oval nucleus or remaining BNST nuclei (e.g. juxtacapsular, anteromedial and anterolateral nuclei) combined. Within manual segmentations, pixel area of each channel's signal was separately threshholded with the max entropy algorithm. Signal pixel counts were detected using the analyze particles function. Percent pixel area of VIP+-specific terminals (i.e. EGFP+/tdTomato+) and total v/vlPAG terminals (i.e. EGFP(+)/tdTomato(+) and EGFP(+)/tdTomato(-)) were calculated in Fiji. Percent VIP(+) terminal area was determined by subtraction of percent tdTomato(+) area from total percent EGFP(+) area. VIP(-) terminal area was calculated by calculating percent difference of total EGFP+ terminal area from EGFP(+)/tdTomato(+).

Fear conditioning experiments

I adopted Penzo et al's fear conditioning paradigm for acute and chronic loss-of-function maternal Grb10(+) vlPAG experiments with minor modification (Penzo et al., 2015). Accordingly, conditioning foot shock intensities for acute and chronic loss-of-function experiments were 0.6 mA and 0.8 mA, respectively. Fear memory retrieval test and extinction for the chronic experiment measured percent freezing during auditory cues in a novel context (same as (Penzo et al., 2015). Retrieval test cues were the same as training conditioned stimulus (CS) cues (5, 30-s variable 75 dB tones). Extinction auditory cues were also the same but 10 total tones were delivered per session. Percent freezing was calculated as average percent freezing amongst all individual tone displays. Acute experimental testing days measured freezing to shock chamber context only.

Accordingly, mice were placed in conditioning chamber for 10 minutes and freezing was recorded for 3, 30 s clips between minutes 4-7 which refers to the time of maximal fear memory recall. Percent freezing shown in figure 37 reflects the average percent freezing for these 3 recordings. Prior to fear chamber context habituation, baseline freezing was tested for in a completely different context than the fear chamber as described previously (see figure 37) (Penzo et al., 2015). A 5 mg/kg dose of clozapine-N-oxide (CNO) (Tocris, # 4936) was used for DREADD activation in acute experiments. Fresh CNO solution was prepared prior to each experiment by dissolving 5 mg in DMSO and diluting this to 5 mg/ml in sterile saline. The same solution without CNO was prepared fresh prior to each experiment and used as vehicle control. CNO or vehicle was administered intraperitoneally exactly 45 minutes prior to testing.

Stereology for chronic loss-of-function experiments was performed for matGrb10+ nuclei as described in previous methods above.

Statistics

AAV-labeled terminal area in BNST subnuclei was compared using a 2 (terminal type - VIP+, non-VIP+) x 2 (BNST area - ovBNST, ju,al,amBNST) 2-way ANOVA. Sidak-corrected post-hoc tests were used to examine differences of terminal type within each location of the BNST. For acute fear conditioning, a 2 (treatment – CNO, vehicle) x 5 (US number) repeated measures two-way ANOVA was employed. Significant US number – treatment comparisons were tested for using a Sidak-corrected post-hoc test. Acute contextual freezing on

test day iterations were compared between groups for each day using a student unpaired t-test. Paired t-tests were used amongst testing days within the two scheduled treatment groups. Chronic ablation statistical testing used the same statistical approach as used for acute experiments. R^2 value for test day percent freezing and vlPAG matGrb10+ neuronal correlations in chronic experiments was determined using one-tailed Pearson's correlation. *matGrb10+* cell amounts were in Cre+ and Cre- mice analyzed with a one-tailed, unpaired student t-test. Alpha was set to 0.05 for all experiments.

3. Results

Monoallelic Grb10 reporter expression validation

I developed a fluorescent protein-based strategy to visualize cells containing PO-specific monoallelic or biallelic *Grb10* expression in mouse brain (Figure X). Implantations of recombined ESC-containing blastocysts into pseudo-pregnant mouse recipients led to successful transmission of each allele, *Grb10^{P2A}H2B-Venus, Grb10^{P2A}H2B-tdTomato, Grb10^{P2A}H2B-tdTomato^{T2A}iCre*, and the establishment of 2 new *Grb10* FP reporter lines and 1 *Grb10* FP reporter/Cre driver line. These novel mice were designed to faithfully report the expression of each *Grb10* allele with nuclear FP expression. Therefore, I first examined if the generated mice faithfully reported the endogenous Grb10

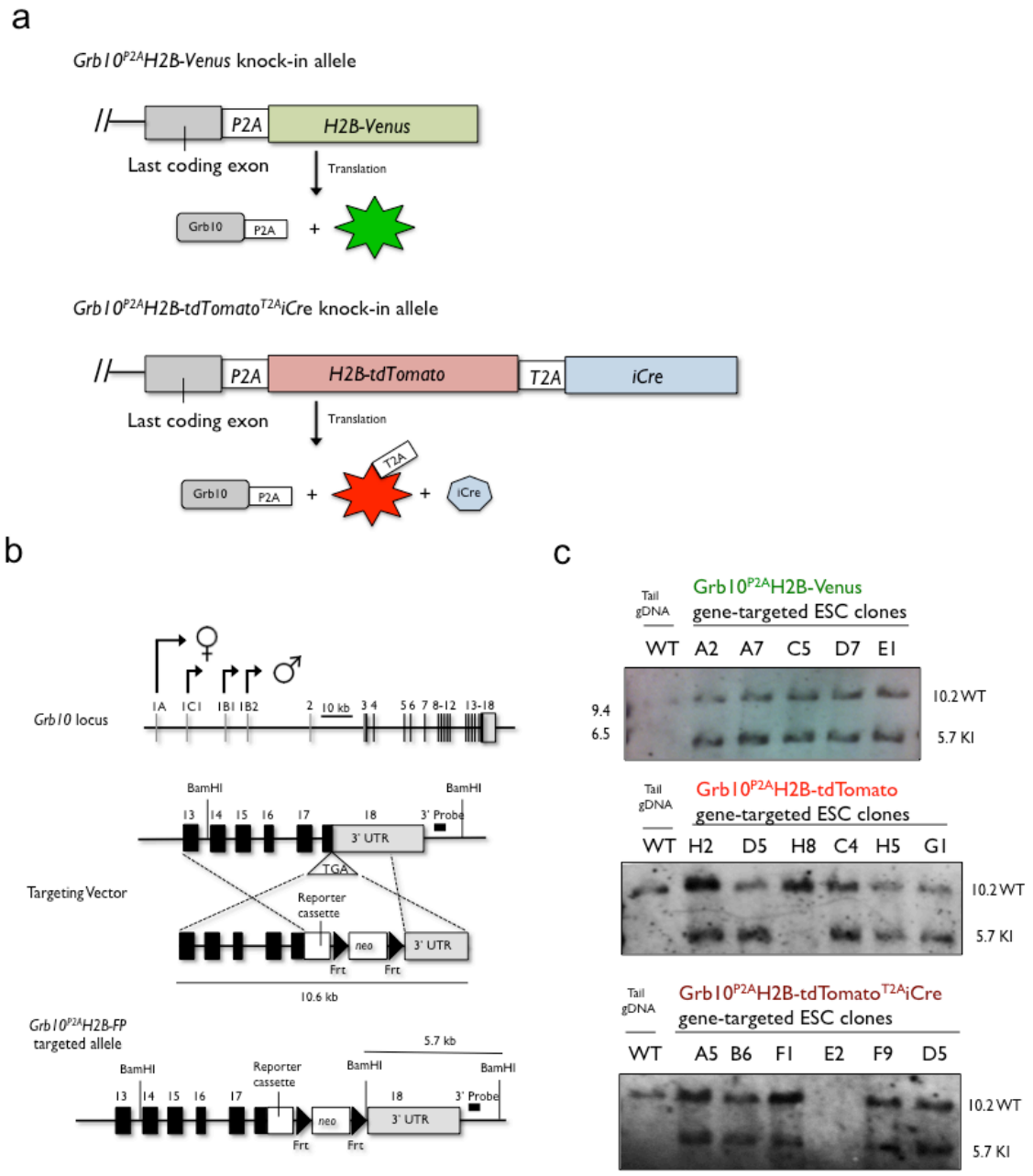

Figure 27. Grb10 allelic reporter/Cre-driver design and targeted ESC screening. a) Cartoon schematic of Grb10 allelic reporter/Cre-driver strategy. Knock-in reporter alleles (venus, top; tdTomato-iCre, bottom) report Grb10 transcription in separate colors with an H2B-fused FP (+/- iCre recombinase). Grb10, FP, and iCre recombinase unwanted fusion events are minimized through genetically-encoded self-cleaving 2A peptides separating each gene. Every gene product should therefore retain proper functionality due to translational separation. b) Grb10 genomic structure (top), targeting event (middle), and recombined targeted knock-in allele (bottom). Maternal transcripts arise from 5' promoter 1A (denoted by female gender symbol), whereas paternal transcripts are driven from promoters 1C, 1B1, and 1B2 (denoted by male gender symbol). Both transcripts

terminate in exon 18. Black boxes – coding regions; Number above regions indicate exon number. Targeting vectors were designed to replace the exon 18 stop codon with in-frame fluorescent protein (FP)/Cre reporter cassettes. BamHI sites were used for southern blot screening with 3' probes. The successful targeted allele (bottom) is indicated by a 5.7 kb (10.2 kb for WT) band in southern blot screens. c) Southern blot screens of targeted ESCs for each reporter/Cre line showing positive ESC clones (indicated by 5.7 kb knock-in BamHI fragments) in which two clones each were used for subsequent chimeric mouse generation. Control wild-type genomic DNA from mouse tail is loaded in lane 1

expression using confocal microscopy and Grb10 immunohistochemistry in brain sections of dual *Grb10*$^{\text{♀ H2B-Venus/♂ H2B-tdTomato}}$-reporting mice. As expected, the subcellular localization of both paternal H2B-tdTomato and maternal H2B-Venus protein expression was nuclear (Figure 28a). Paternal reporter expression filled nuclei of round shapes indicate of neuronal cell types with variable intensity across cells and brain regions, whereas maternal expression localized to oval-shaped nuclei indicative of non-neuronal cells with a common intensity. These observations were not sex-dependent (data no shown) and did not change with reversal of PO designation of each H2B-FP reporter (see next results section). Staining patterns of endogenous Grb10 protein followed very closely regional paternal H2B-tdTomato expression (Figure 28, b-e). Specifically, major brain areas marked by *patGrb10* expression included the medial habenula of the epithalamus, thalamic paraventricular nucleus, midbrain dorsal raphe nucleus, hypothalamic paraventricular nucleus, and basomedial amygdala shadowed that of Grb10 staining (Figure 28,b-d). The Grb10 immunostaining did not label the cells marked by the maternal H2B-Venus protein expression. The following results suggest the *patGrb10*-reporting mice faithfully express FP's in cellular nuclei of patGrb10 protein-expressing brain regions. The validity of the choroid

plexus and meninges matGrb10-expressing FP could not be determined based on the immunostaining results.

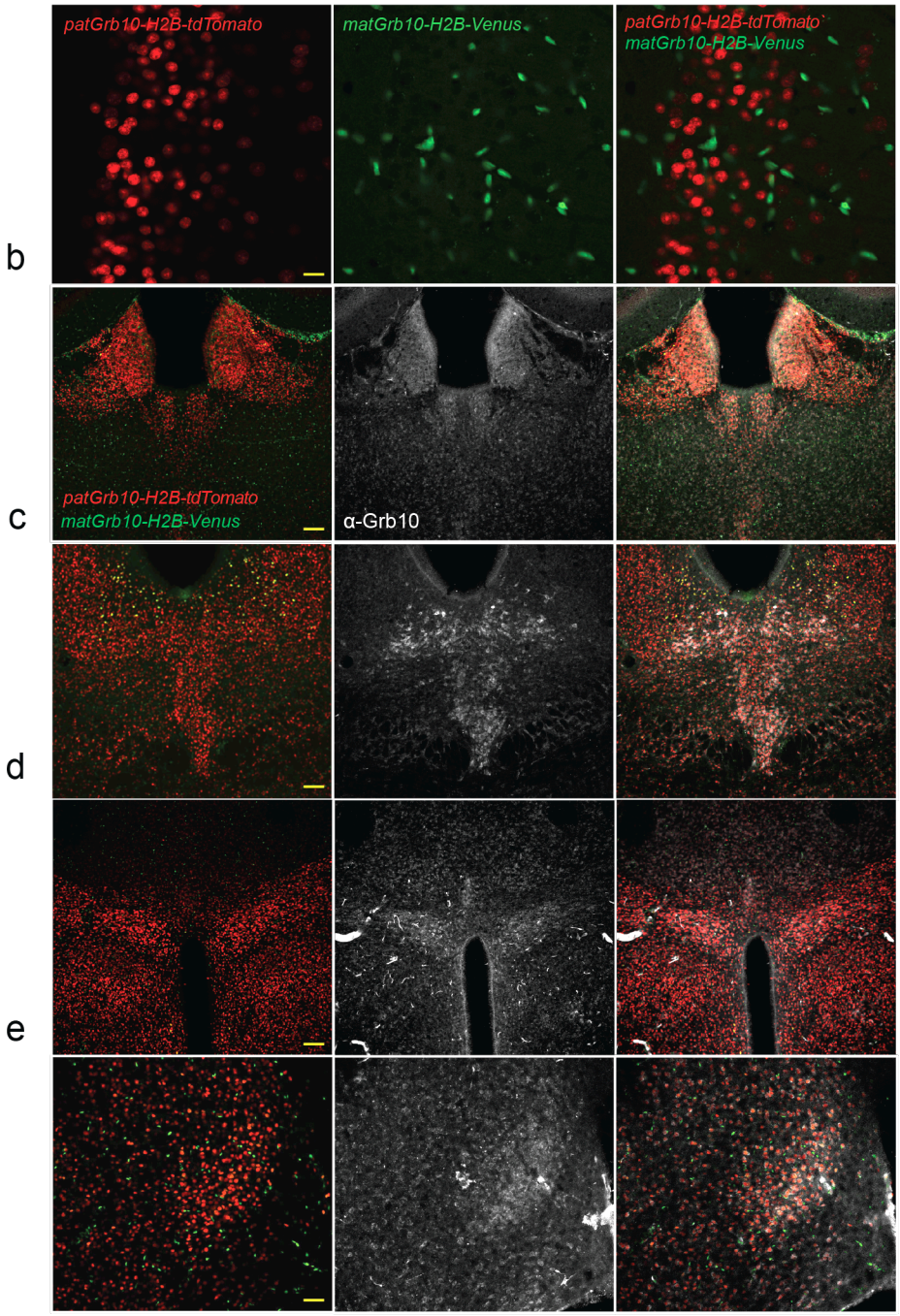

Figure 28. Monoallelic Grb10 reporter expression validation. a) 40x examination of paternal (left), maternal (middle), and merged (right) subcellular FP expression in layer 2/3 of the retrosplenial cortex. b-e) Grb10 staining patterns in a separate

Grb10$^{♀ H2B\text{-}Venus/♂ H2B\text{-}tdTomato}$ brain in major areas of paternal H2B-tdTomato expression, including (b) medial habenula, c) dorsal raphe nucleus, d) hypothalamic paraventricular nucleus, and e) basomedial amygdala). Scale bars: a) 25 um, b-d) 75 um, e) 50 um

Monoallelic Grb10 reporter expression characterization

The differences in nuclei shapes observed amongst maternal and paternal H2B-FP-expressing cells indicated different cell-type specification of each *Grb10* allele dependent on PO. To understand what major cell-types each allele is specified in, I performed immunostaining against markers of different cell-types in brain sections from *Grb10*$^{♀H2B\text{-}tdTomato/♂H2B\text{-}Venus}$-reporting mice. NeuN staining established neuron-specific expression predominantly in *pat*- but not *matGrb10*-expressing cells (Figure 29, a-d). Lectin-488 staining of endothelium revealed the localization of matH2B-tdTomato-expressing nuclei on top of or enclosed within individual endothelia (Figure 29, e). PDGFRβ+ staining of pericytes labeled a subset of these cells indicating pericyte-specific expression, while lack of staining indicated endothelial cell-specific expression. Expression was also observed in presumptive ependymal cells of blood-brain borders (not shown). This indicates *matGrb10* expression is primarily targeted to pericyte and endothelial cells, respectively. Collectively, *Grb10* alleles are expressed in different cell types of the mouse brain, which were uncovered through novel dual-reporting monoallelic Grb10 reporter mice defined and generated in this thesis.

The amount and intensity of labeling of the *patGrb10*+ neurons displayed throughout the brain was not uniform, but exhibited a largely subcortical pattern of high expression in select areas. I hypothesized that the observed expression

profile indicated a systems-level patterning of *patGrb10* expression. To quantify the whole-brain distribution of the *patGrb10*-expressing neurons,

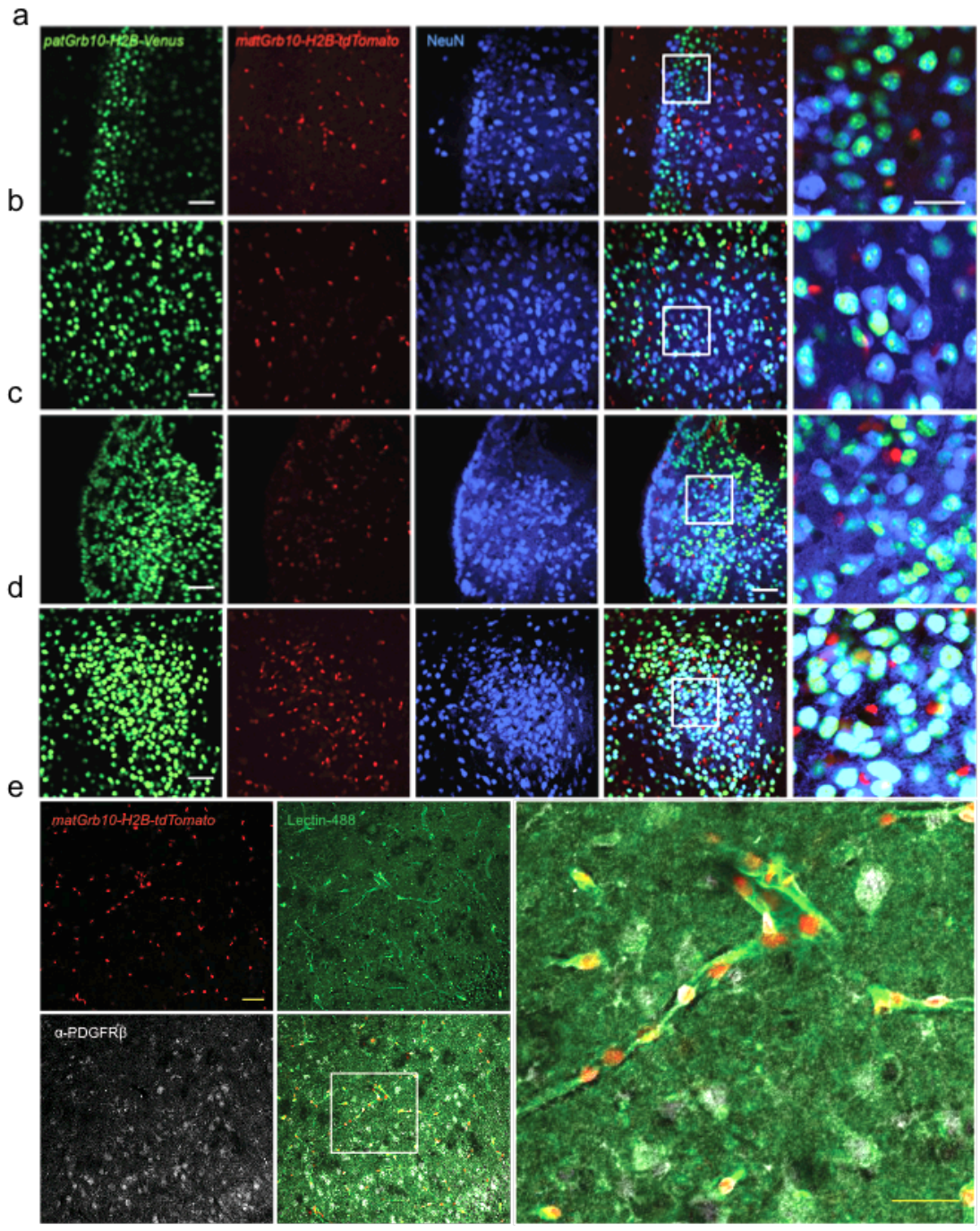

Figure 29. Cell-type specification of *Grb10* alleles. a-d) Neuron-specific expression of paternal or maternal Grb10-expressing cells identified by NeuN stains. Demonstration of NeuN+ staining in paternal-specific Grb10-expressing cells is shown in the a) retrosplenial cortex (layer 2/3), b) cortical amygdala, c)

medial habenula, and d) ventromedial hytpohalamus. e) Maternal Grb10-expressing cells are affiliated with lectin-488+ endothelium amongst PDGFRβ+ and PDGFRβ- cells. Scale bars: a-d) 50 um; zoom - 25 um; e) 50 um; zoom - 50 um

I next performed whole-brain STPT imaging and analysis on two adult male *patGrb10-H2B-Venus* mice brains. Mean cell densities of patGrb10+ containing ROIs were determined as described in chapter 2 and 3. For visualization purposes, voxelized cell counts were warped onto the reference brain space (Figure 30, a). The anatomical distribution of the *patGrb10*-expressing neurons replicated observations from confocal microscopy-based experiments described above, with some additional detail: strong and diffuse cell labeling was seen starting at the olfactory areas and basal forebrain, which continued caudally in subcortical and medial areas throughout the entire brain (Figure 30, a). A *matGrb10-H2B-Venus* voxelized brain was superimposed in order to visualize the contrast of expression amongst alleles. Vasculature related structures including the pia, ventricular systems, and microvasculature are labeled. In this view, the *patGrb10* expression is strikingly seen as the dominant neuronally expressed allele in the mouse brain.

I next quantified and analyzed whole-brain *patGrb10*-expressing ROI cell densities to identify the strongest nodes of expression. Amongst all of the cells visualized and counted, the upper quartile range of ROI cell densities were selected as “top hit” ROIs. ROIs from this classification were further reduced to the top 15 ROIs per major hierarchical structure (e.g. cortex, olfactory area, hippocampal formation, cortical subplate, cerebral nuclei, thalamus,

hypothalamus, midbrain, and hindbrain) in order to normalize amount of top ROIs by structure. Under these guidelines, the 75th percentile cutoff for ROI cell density was 13,721 cells/mm^3 with an overall range of 69,978 cells/mm^3 to 78 cells/mm^3 (mean – 10,606 cells/mm^3; SD – 13,565 cells/mm^3) (Figure 30). All major grouping structures contained *patGrb10+* expression nodes with variable amounts of ROIs (86 total) contained within each. Accordingly, layer 2 and 2/3 of the ventral retrosplenial cortex (RSPv2-2/3) was the only cortical node of expression identified and was accompanied by the anterior cortical amygdala (COAa) and nucleus of the lateral olfactory tract (NLOT2,3) nodes in the olfactory area. In the hippocampal formation, a node containing the medial ventral entorhinal cortex (ENTmv) with the pre- and post-subiculum (PRE, POST) was identified. A basomedial (BMA) and posterior amygdala (PA) node was found in the cortical subplate. An identified cerebral nuclei node contained many ROIs of bed nucleus of stria terminalis (BST/BNST) as well as other ROIs including the ventral lateral septum (LSv), major island of calleja (islm), caudal pallidum (PALc), lateral division of the central amygdala (CeAl), and the anteroventral medial amygdala (MEAav). A thalamic node consisted of the subparafascicular area (SPA) with a specifically dense magnocellular division (SPFm). Midline thalamic regions (MTN) were also involved, with main density contributions seen in the reunions nucleus (RE) and paraventricular nucleus (PVT). Replicating confocal observations, the medial habenula (MH) of the epithalamus (EPI) was also an ROI of the thalamic node. The hypothalamus contained a node of ROIs with the densest amount of cells amongst all structures (max: PVHmm – 69,9978

cells/mm^3; min: DMH – 52,026 cells/ mm^3). Accordingly, it consisted of several magnocellular components of the paraventricular nucleus (PVHm), the dorsal medial hypothalamus (DMH), ventral medial hypothalamus (VMH), ventral premammilary nucleus (PMv), medial preoptic nucleus (central and medial, MPNc,m), and the anteroventral posterior periventricular nucleus (AVPV). A specifically dense precommisural nucleus (PRC) was found amongst other ROIs in the midbrain. The other ROIs included the dorsal raphe nucleus (DR), PAG, edinger westphal nucleus (EW), midbrain trigeminal nucleus (MEV), the medial, pre-, and olivary pretectal nuclei (MPT, PPT, OPT), several components of the super colliculus (SC), nucleus of Darkschewitsch (ND), and nucleus of posterior commissure (NPC). Lastly, the hindbrain produced a collection of dense ROIs containing many components of the nucleus of solitary tract (NTS) and parabrachial nucleus (PB). In addition, the node contained the dorsal motor nucleus of the vagus nerve (DMX), Barrington's nucleus (B), laterodorsal tegmental nucleus (LDT), locus ceruleus (LC), and the dorsal tegmental nucleus. In sum, whole-brain quantification of neuronal patGrb10+ cell densities identified a number of predominantly subcortical areas that are known to be involved in several aspects of stress processing,

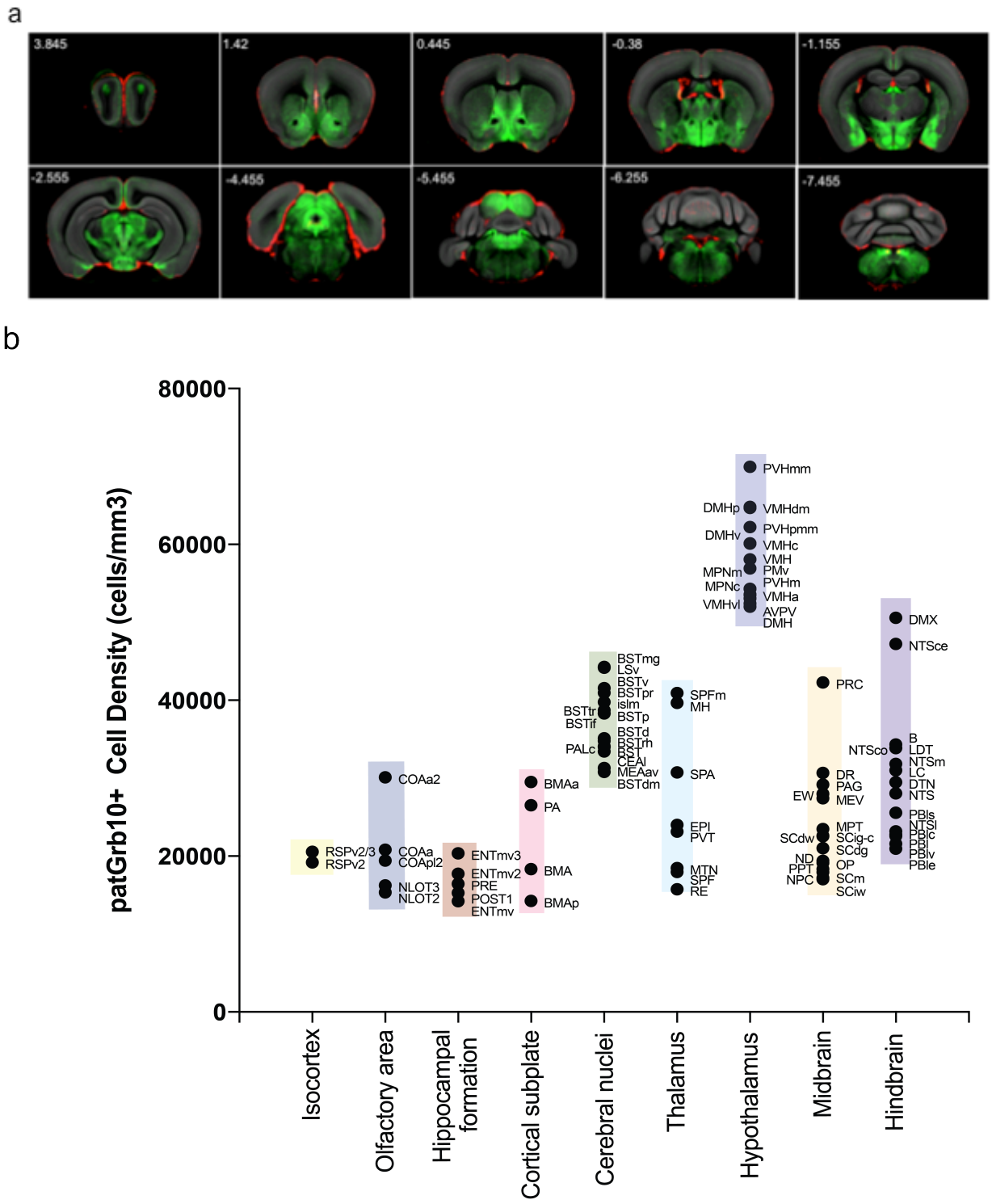

Figure 30. patGrb10+ nodes of neuronal expression. a) Voxelized cell count visualization of warped *patGrb10+* (green) or *matGrb10+* (red) H2B-Venus labeled cells in whole-brain reference space. Anterior/posterior bregma coordinate reference is listed in upper left of each image. b) Quantification of *patGrb10-H2B-Venus* cell density (n=2). Top 15 ROIs in the upper quartile range

of *patGrb10+* cell density are listed per major hierarchical brain structure and plotted against ROI cell density on the y-axis. All abbreviations can be found in results section and table 1.

Identification of biallelic Grb10-expressing neurons

Targeted neuronal expression of *patGrb10* indicates imprinting on the maternal allele in most neurons whereas maternal microvasculature-associated cell expression indicates paternal allele imprinting in those cell type, in addition to cell populations that do not express either allele, such as the majority of cells in the cortex or cerebellum. Therefore, any biallelic expression observed would indicate a loss of imprinting at the allele specifically imprinted in one of the given cell types. I hypothesized that biallelic populations of Grb10-expressing cells in the brain existed and this could be found using my dual *Grb10* expression-reporting approach. Observed cells expressing the two Venus and tdTomato fluorophores would be positive for *Grb10* maternal and paternal expression (i.e. biallelic). Using confocal microscopy for the initial examination of a *Grb10*$^{♀H2B\text{-}tdTomato/♂H2B\text{-}Venus}$-reporting mouse brain in sections I did not find biallelic expression in the vasculature-associated cell types. Interestingly, biallelic Grb10-expressing neurons were observed in 3 brain areas, including the hypothalamic periventricular nucleus, anterior pretectal nucleus of the midbrain, and the ventrolateral column of the periaqueductal gray (vlPAG) (Figure 31). These results provide first evidence for a loss of maternal *Grb10* imprinting and consequently bi-allelic Grb10 (*biGrb10*) expression in neurons of brain areas involved in defensive behaviors.

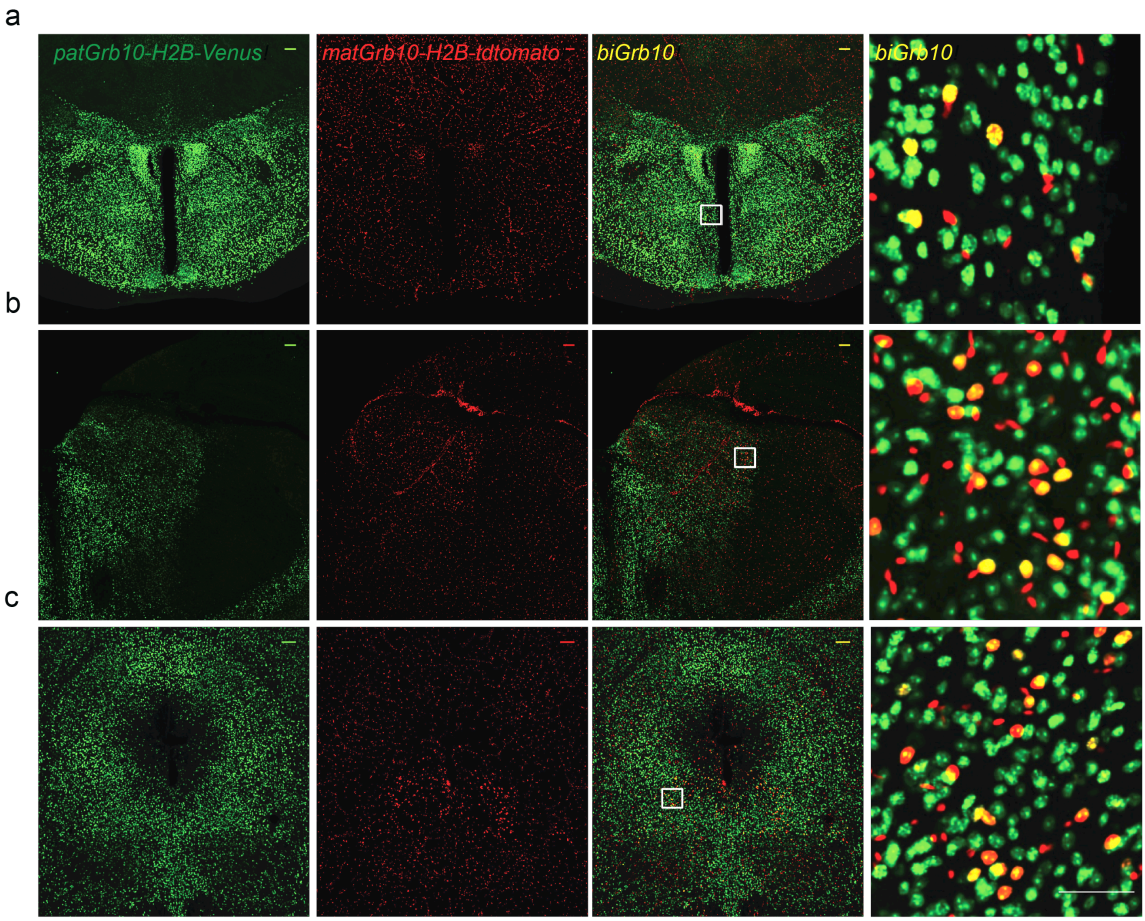

Figure 31. Identification of biallelic *Grb10*-expressing neurons. a-c) Main brain areas containing neuronal biallelic *Grb10 (biGrb10)* expression, indicated by H2B-Venus+/H2B-tdTomato+ nuclei (far right). Brain areas shown are a) hypothalamic periventricular nucleus, b) anterior pretectal nucleus, and c) vlPAG. Scale bars: 100 um; far right – 50 um

Neuronal cell type identification of biGrb10-expressing vlPAG neurons

Regions of *patGb10+* expression defined a network of functionally related brain systems. However, the cellular specificity of *patGrb10+* expression was very broad, as all or most cells were labeled by the patGrb10-reporter in these areas. This suggests that *patGrb10+* expression is targeted to specific brain areas; the circuits labeled by the *patGrb10* allele are very broad and participate in many behaviors and brain functions. However, the more selective *biGrb10*

expression may mark neuronal populations that may have more defined and perhaps novel behavioral roles. In preliminary immunohistochemistry screens, the periventricular hypothalamus population localized to ~50% of dopaminergic cells (not reported in chapter IV). Dopaminergic periventricular cells represent a highly specialized and sparse population that control pituitary release of prolactin – a main hormone controlling maternal care and reproduction (Freeman et al., 2000). ~1/2 of the anterior pretectal nucleus (APN) *biGrb10*+ neurons expressed GABA, and APN GABAergic cells may state-dependently gate thalamocortical sensory transfer (Bokor et al., 2005). Of particular interest, the PAG contains functionally distinct columns of neurons that are collectively involved in the defensive flight or fight response (Vianna and Brandao, 2003). The vlPAG column contains heterogeneous neuronal cell types and is a primary region specifically responsible for defensive freezing behavior in rodents (Schenberg et al., 2005; Tovote et al., 2016; Tovote et al., 2015). Since the largest population of *biGrb10*-expressing neurons (*biGrb10*) was found within the vlPAG, I hypothesized that these cells may play a specific role in these behaviors. To begin to study the vlPAG *biGrb10* cells I next examined their cell types in a series of mouse genetic and immunostaining/stereology experiments (Figure 31 and 32). The single allele *matGrb10-H2B-Venus* mice were used for *biGrb10*+ neuron co-labeling studies, since all *matGrb10*+ neurons in the vlPAG are also *patGrb10*+ (Figure 31). First I asked what are the cell type proportions among all *biGrb10*+ cells. GAD2, a GABAergic neuron marker, colabeled the largest percentage of *biGrb10*+ neurons (50%), as revealed through genetic expression

reporting in double transgenic *GAD2-NLS-mCherry*/*matGrb10-H2B-Venus* mice (Figure 32). Vasoactive intestinal peptide (VIP) - a neuropeptide commonly associated with a subset of GABAergic neurons – staining labeled an additional 26% of *biGrb10*+ neurons in these double transgenic mice (Figure 32). In addition, a small portion, approximately 6% of *biGrb10*+ neurons were serotonergic (staining shown in Figure 33, b). Neither the VIP+ nor the 5-HT+ neurons in the vlPAG expressed GAD2, regardless of *biGrb10* expression. The identity for the remaining about 20% of *biGrb10*+ neurons is currently not clear. Next I asked what is the proportion of *biGrb10*+ neurons among the identified cell types. Mean percentages of each colabeled cell type that expressed *biGrb10* was: 6% for GAD2+, 5% for 5-HT+, and 71% for VIP+ neurons (Figure 32, c). Mean vlPAG cellular densities for each colabeled population were 1,366 (*biGrb10+)*, 22,529 (*GAD2*+), 1,800 (5-HT+), and 312 (VIP+) cells/mm3 (Figure 32, d), and colabeled densities amongst *biGrb10*+ neurons were 668 (GAD2+), 59 (5-HT+), and 245 (VIP+) cells/mm3. Notably, the vlPAG spatial distribution of the *biGrb10*+ neurons differed based on the cell type. The VIP+ neurons were found to reside along the surface of the aqueduct (mean soma to aqueduct distance = 46 um), whereas VIP- neurons were positioned more away (257 um) from aqueduct on average (Figure 32, e).

Additional neuron cell type screening of the vlPAG neurons identified serotonergic, cholinergic, dopaminergic, and glutamatergic populations in the vlPAG (Figure 33). GAD67/GAD1 and GABA staining for GABAergic neurons

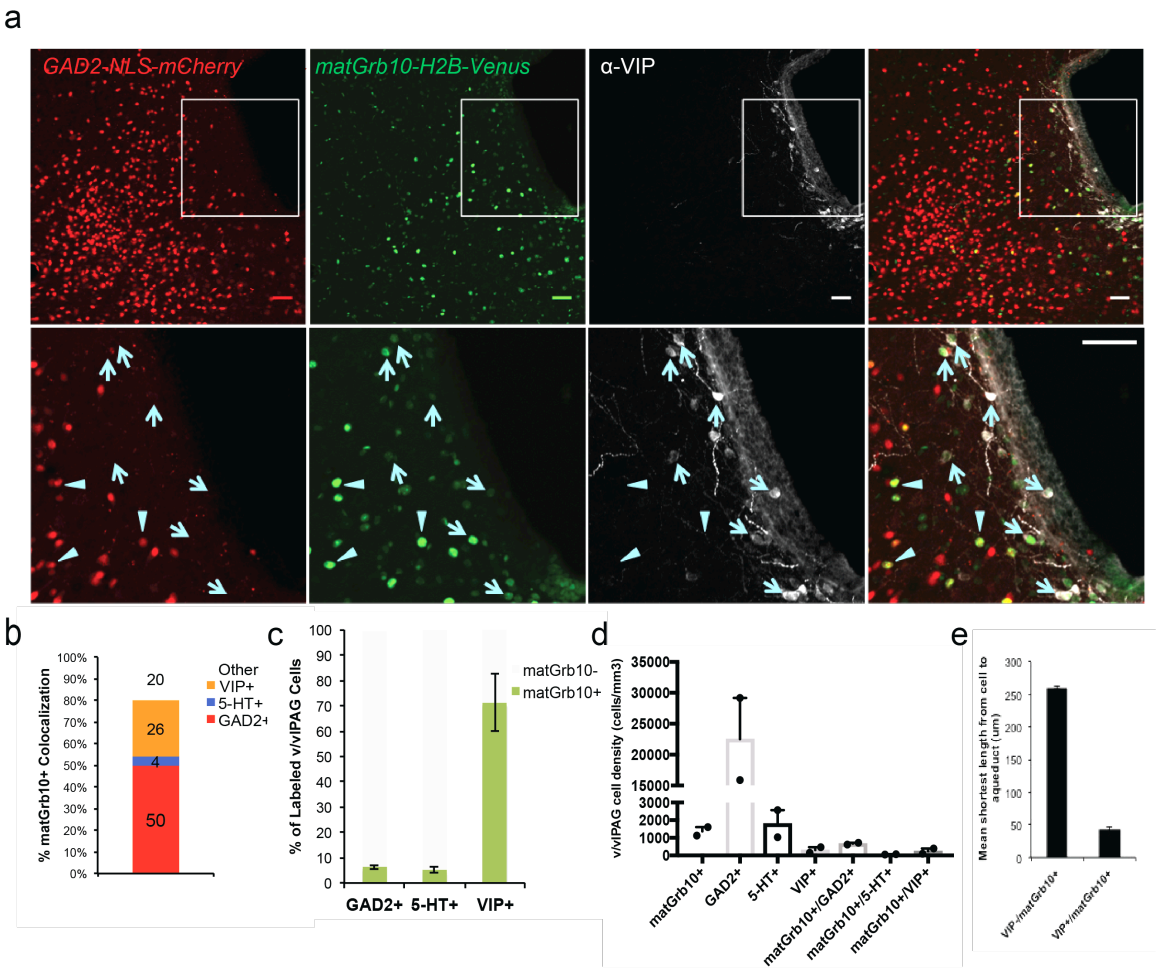

Figure 32. vlPAG *biGrb10+* cell type identification. a) Confocal images of VIP staining within a *GAD2-NLS-mCherry*/*matGrb10-H2B-Venus* dual reporter mouse in the vlPAG. Individual labeling is shown (from left to right) for *GAD2+*, *matGrb10+*, and VIP+ neurons with merged image to the right. Scale bars = 25 um. *GAD2+*/*matGrb10+* and VIP+/*matGrb10+* neuron examples are indicated with triangles and arrowheads (bottom), respectively. b-e) Quantification of b) percent *matGrb10*-colocalion by cell type, c) percent of cell types colocalized with *matGrb10,* d) mean vlPAG cellular density for colocalized cell types, and e) mean soma to aqueduct distance (um) for VIP+ and VIP-/*matGrb10+* neurons.

was also performed but failed to label any vlPAG cells (data not shown). With the exception of serotonergic cells (described in figure 32), the labeled populations did not show any colocalization with *biGrb10+* cells. In summary, *Grb10* is biallelically expressed in a small portion of GAD2+ neurons in the majority of sparse, periventricular, VIP+/GAD2- neurons of the vlPAG. The cell

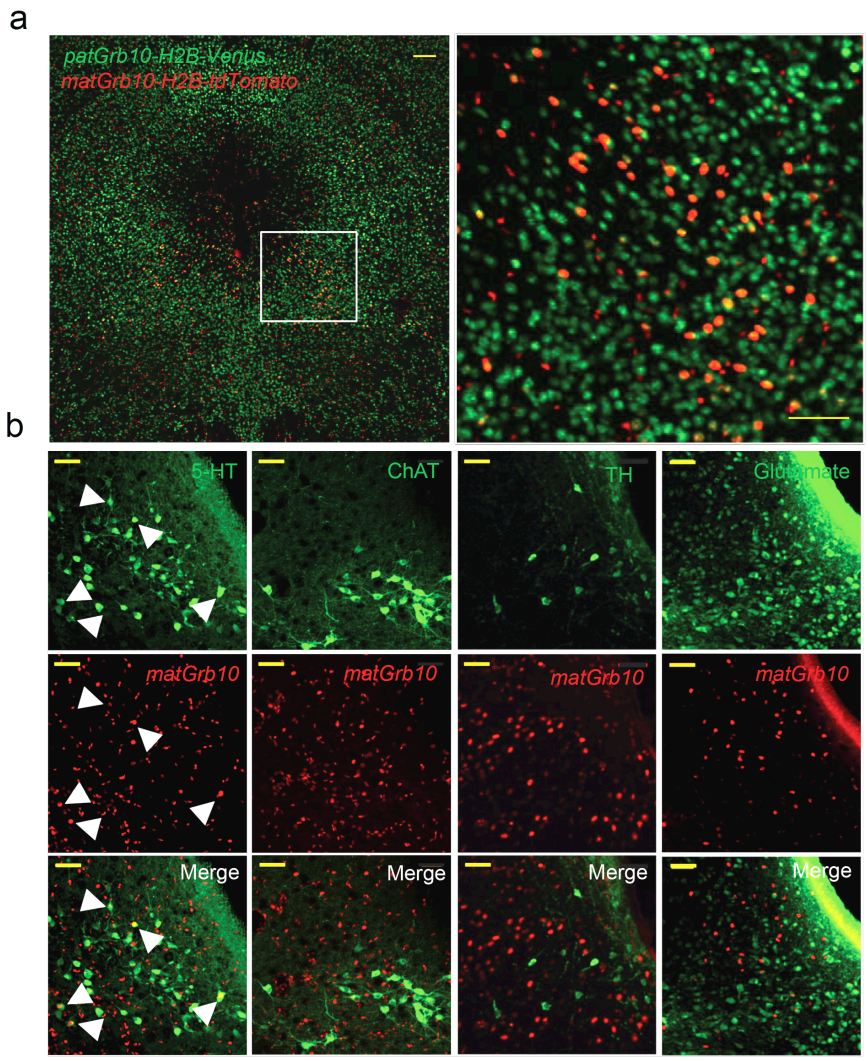

Figure 33. vlPAG cell types screened for *biGrb10* expression. a) Representative vlPAG section of a *Grb10*$^{♀H2B\text{-}tdTomato/♂H2B\text{-}Venus}$-reporting mouse displaying peak *biGrb10*+ neuronal density as indicated by H2B-tdomato+/H2B-Venus+ nuclei. Scale bar = 100 um, 25 um right. b) Representative images of (from left to right) serotonergic (5-HT+), cholinergic (ChAT+), dopaminergic (TH+), and glutamatergic (glutamate+) vlPAG populations in a *matGrb10-H2B-tdTomato* mouse brain. Colabeled examples of 5-HT+/*matGrb10*+ cells are indicated by triangles. Scale bar = 25 um.

type specificity of vlPAG *biGrb10*+ neurons suggests their involvement in defensive behavior circuitry based on the established role of this structure in freezing behavior (Tovote et al., 2016; Tovote et al., 2015).

Characterization of vlPAG biGrb10+ and VIP+ neuronal projections

Immunostaining results confirmed a distinct cell type specificity of neurons marked by the *biGrb10* expression. I next hypothesized that the connectivity of these cells also possess distinction amongst other vlPAG neurons. I approached this question using stereotaxic delivery of Cre-dependent FP-expressing AAV in the vlPAG of Cre recombinase-expressing transgenic mice. Maternal transmission of the *Grb10-tdTomato-iCre* allele allowed genetic access restricted to the total *biGrb10*+ vlPAG population in offspring. *VIP-Cre* mice allowed genetic access restricted to the VIP+ vlPAG cells only, which according to my immunostaining estimates, should mostly (~70%) express *biGrb10*, and contain 26% of total *biGrb10*+ vlPAG neurons. Therefore, the combined mouse strategies allowed me to address total *biGrb10*+ neuron projection targets from those that are only VIP+. Accordingly, *AAV-CAG-FLEX-EGFP* injection into the vlPAG of *matGrb10-tdTomato-iCre* mice (n=2) revealed ipsilateral EGFP+ axon terminals in ascending subcortical brain regions (Figure 34). Specific output targets of *biGrb10*+ neurons included the BNST, CeAl, dorsomedial nucleus of the hypothalamus (DMN), peripeduncular nucleus (PPN), and 3 regions of the midline thalamus: PVT, central medial nucleus (CM), and intermediodorsal nucleus (IMD). I next asked how axon projections from the all *biGrb10*+ vlPAG neurons compare to those that are VIP+ only. Towards this goal, I coinjected *VIP-Cre* (n=3) mice with AAV-CAG-FLEX-tdTomato and AAV-CAG-EGFP into the vlPAG. This coinjection strategy was used to understand the specificity of VIP+-specific projection terminals in yellow from non-specific bulk vlPAG

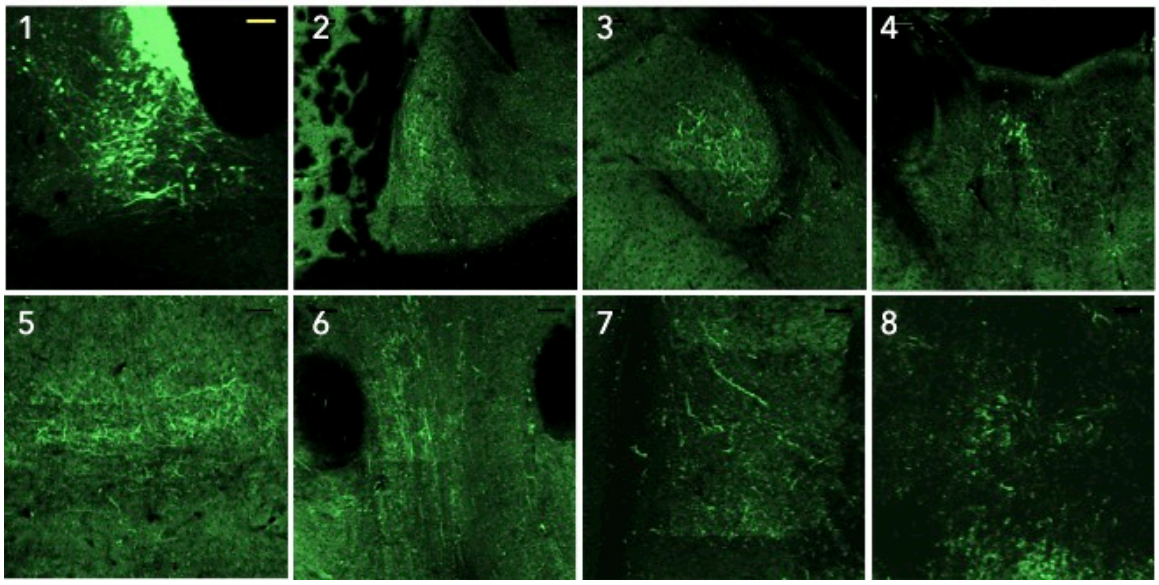

Figure 34. Projection patterns of *biGrb10*+ vlPAG neurons. 1-8) Representative 2-photon images show results of an *AAV-CAG-FLEX-EGFP* injection into the vlPAG of a *matGrb10-tdTomato-iCre* mouse brain. Originating from the (1) vlPAG injection site, ascending, ipsilateral axon terminations were visualized in the 2) BNST 3) CeAl 4) PVT 5) CM 6) IMD 7) DMN and 8) PPN. Scale bar = 100 um. Abbreviations found in text and table 1.

projections in green. Using this approach, unilateral coinjections revealed bilateral terminals only in the BNST (Figure 35). BNST subdivisions were further analyzed for innervation preferences amongst VIP+ and VIP- vlPAG neurons. Terminal area for each terminal type (VIP+/-) was quantified amongst the oval nucleus of the BNST (ovBNST) and other subdivisions (anterolateral, anteromedial, juxtacapsular nucleus) combined (Figure 35, d). Statistical comparisons revealed a strongly significant interaction of terminal type amongst BNST nuclei ($F(1,8) = 70.18$, $p<0.0001$). Post-hoc analyses indicated significant VIP+ terminal enrichment (80% terminal area) in the ovBNST ($p=0.0008$). VIP- projections, labeled in EGFP only, conversely accounted for a significant ($p=0.0006$) 79% terminal area outside of the ovBNST. VIP+ neurons therefore provide a highly specific majority of vlPAG inputs to the ovBNST. Additionally,

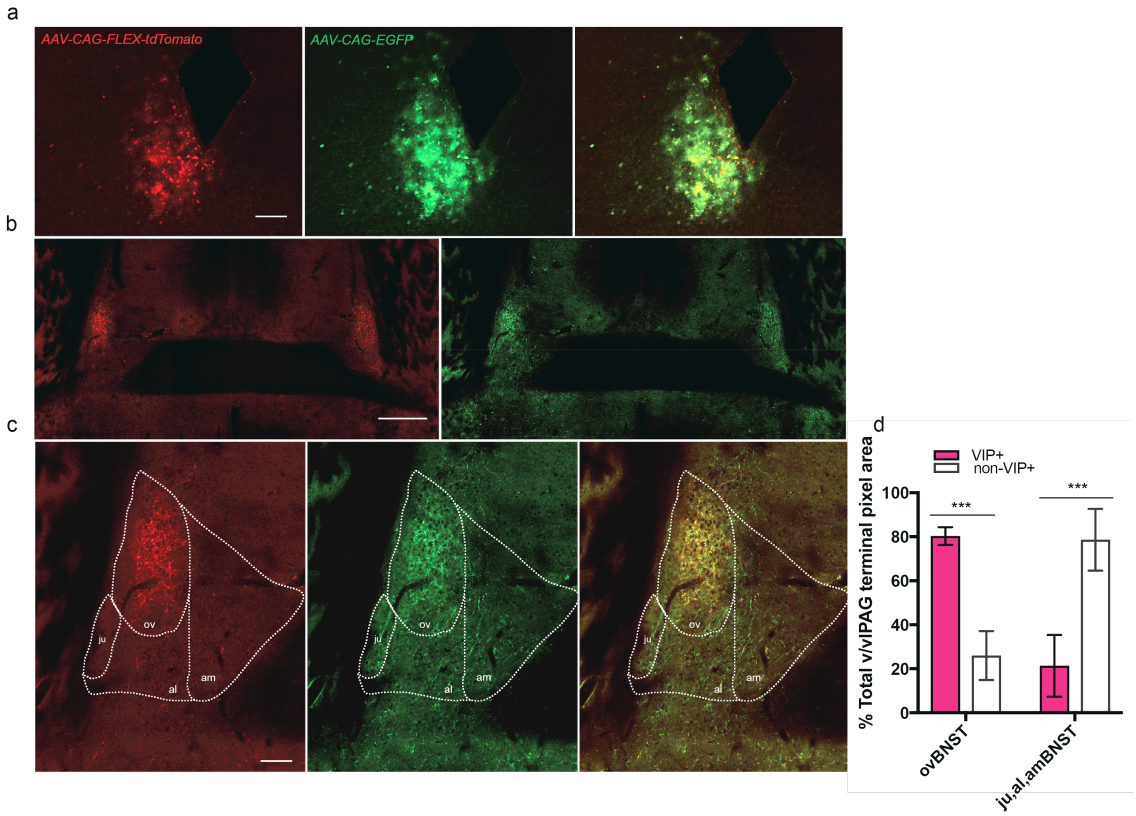

Figure 35. VIP+ vlPAG innervation of the ovBNST. a-c) Representative 2-photon image results of a AAV-CAG-FLEX-tdTomato/AAV-CAG-EGFP coinjection into the vlPAG of a *VIP*-Cre mouse. a) vlPAG unilateral injection site, b) bilateral BNST innervation, c) BNST subdivision segmentation, d) Quantification of BNST terminal pixel area from VIP+ (EGFP+/tdTomato+) and VIP- (EGFP+/tdTomato-) terminals amongst the ovBNST and ju,al,amBNST. ***p<0.001. Scale bars = a,c) 100 um, b) 500 um

these findings in combination with immunostaining and *biGrb10*+ tracing results, suggest that the remaining projections (midline thalamus, CeAl, DMN, PPN, al,am,juBNST) observed from total *biGrb10*+ neuron tracing, are GAD2+/VIP-. Therefore *biGrb10*-expressing neurons of the vlPAG appear to fall into two neuronal populations: 1) a GAD2+ population that projects predominantly to the midline thalamus and, 2) a VIP+/GAD2- population that only innervates the ovBNST. Based on the published role of midline thalamus in arousal and awareness (Van der Werf et al., 2002), and the BNST, CeAl in anxiety and fear

processing (Okamoto and Aizawa, 2013; Tovote et al., 2015) these results suggest an involvement of *biGrb10+* neurons in awareness/arousal and anxiety/fear components of defensive behavior, respectively.

Involvement of biGrb10+ vlPAG neurons in freezing behavior

The vlPAG is intricately involved in freezing behavior, a fear-related response in rodents (Vianna and Brandao, 2003). Lesion and pharmacology experiments have indicated an overall pro-freezing role of the vlPAG in conditioned fear responses (Johansen et al., 2010; Koutsikou et al., 2014; LeDoux et al., 1988; McDannald, 2010). Recently, Tovote et al have provided optogenetic loss-of-function experiments to suggest that local GABAergic vlPAG neurons facilitate unconditioned freezing responses by inhibiting glutamatergic brainstem-projecting vlPAG neurons (Tovote et al., 2016). *biGrb10+* vlPAG neurons define a circuit module suggestive of freezing behavior regulation with ~50% of *biGrb10+* vlPAG neurons being GABAergic. Therefore, I asked whether this novel vlPAG population functions in conditioned and/or unconditioned freezing behavior. I first examined freezing responses of *matGrb10-H2B-tdTomato-iCre* mice with chronic loss-of-function manipulations. A Cre-dependent apoptotic strategy for permanent loss of *biGrb10+* neuron function was achieved through *AAV-FLEX-taCasp3-TEVp* bilateral injections. This virus triggers apoptosis of infected, Cre-expressing cells by tobacco etch virus protease-mediated Caspase 3 proteolytic activation (Yang et al., 2013). Bilaterally injected *matGrb10-H2B-Venus* animals, which do not express the Cre

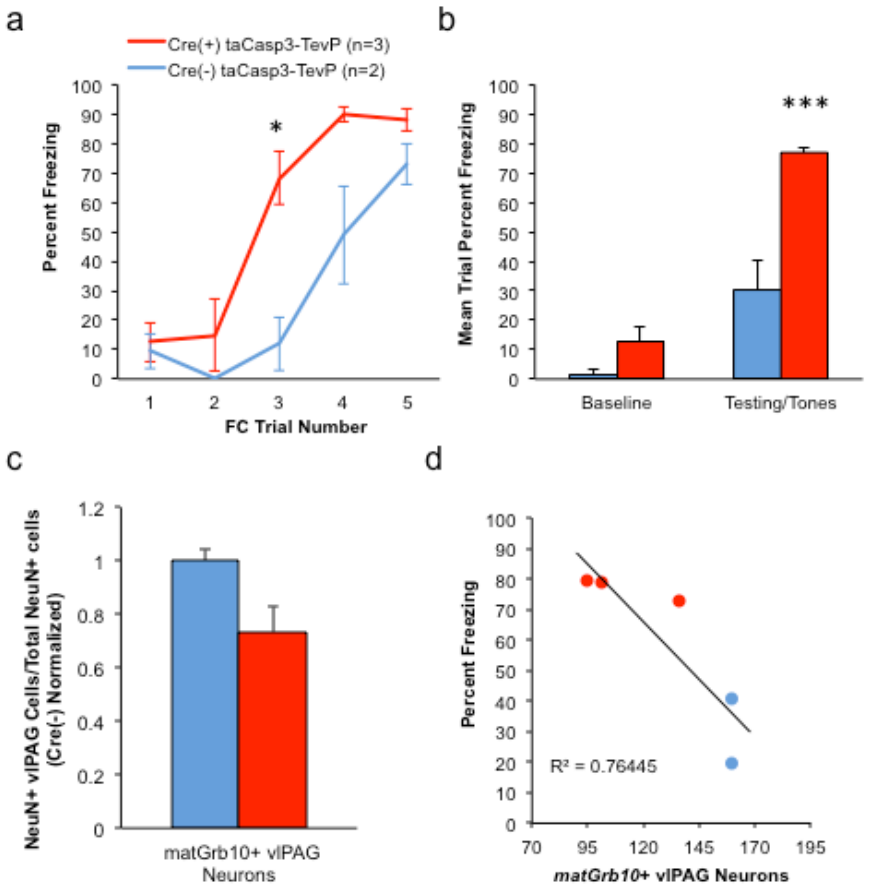

Figure 36. Chronic loss of *biGrb10+* vlPAG neuron function during fear memory acquisition and cued retrieval. Injections of *AAV-FLEX-taCasp3-TEVp* into the vlPAG of *matGrb10-H2B-tdTomato-iCre* (Cre+; n=3) and *matGrb10-H2B-Venus* (Cre-; n=2) mice were performed and percent freezing during a) fear memory acquisition and b) cued fear memory retrieval was analyzed. c) Quantification of vlPAG *matGrb10+* neurons in behaviorally tested Cre+ and Cre- animals from a) and b). d) Correlations of percent freezing during fear memory retrieval and vlPAG *matGrb10+* cell amount quantified in c). Data point colors indicate genotype. p<0.05; ***p<0.005

recombinase, were used as controls. Percent freezing comparisons between the two Cre+ and Cre- groups during fear conditioning revealed a significant main genotype effect ($F(1,3) = 12.49$, $p = 0.039$) and interaction ($F(4,12 = 3.298$, $p = 0.048$), with Cre+ animals showing significantly more freezing behavior (Figure 36, a). Post-hoc analysis identified a significantly higher amount of freezing

amongst Cre+ animals (65% Cre+, 8% Cre-; p=0.028) specifically during CS presentation #3. Cre+ animals also exhibited significantly more freezing during cued fear memory retrieval test (63% Cre+, 9% Cre-; p=0.004) (Figure 36, b). To understand if the viral strategy was effective in ablating the *matGrb10+* neurons, quantifications of total *matGrb10+* vlPAG neurons were obtained from all animals. Cre+ mice were found to contain significantly less (30%; t(3) = 2.989, p (one-tailed) = 0.0291) *matGrb10+* neurons than Cre- mice (Figure 36, c), suggesting that the observed increase in freezing behavior was indeed due to the loss of the *matGrb10+* neuronal population in the vlPAG. To probe this question further, I next asked if there was a relationship between the cell loss and the behavioral effect measured. Pearson's correlational analyses revealed a significant negative correlation ($R^2 = 0.7465$; p (one-tailed) = 0. 0262) amongst total *matGrb10+* vlPAG neurons and percent freezing during memory retrieval test. In sum, these results suggest that a ~30% loss of *biGrb10+* vlPAG neurons was accompanied by increased behavioral freezing in response to fear memory retrieval during acquisition and recent testing. Taken together, these results points towards a regulatory role of *biGrb10+* vlPAG neurons in fear memory-related freezing.

The permanent loss-of-function results implicate *biGrb10+* neurons during fear memory encoding and retrieval. However, the experiment could not test unconditioned freezing, nor could it dissociate memory acquisition from recent memory retrieval. The enhanced freezing seen at both stages could be due to three possibilities: 1) fear memory unrelated freezing activation, 2) enhancement

of memory acquisition only, or 3) memory retrieval enhancement as it is being acquired and during short term retrieval. Acute loss-of-function experiments were next used to tackle these questions, using the inhibitory hM4D(Gi) DREADD for neuronal hyperpolarization during behavior. In this approach, Cre-dependent *AAV-hSyn-DIO-hm4D(Gi)-mCherry* was expressed bilaterally in *biGrb10*+ vlPAG neurons of adult male *matGrb10-H2B-tdTomato-iCre* mice. Clozapine-n-oxide (CNO) administration 45 minutes prior to behavioral testing is expected to induce silencing of the DREADD-expressing *biGrb10*+ vlPAG neurons. As a control for the resulting alterations in freezing behavior I used vehicle-treated *matGrb10-H2B-tdTomato-iCre* mice injected with the same virus. The effect of CNO-induced silencing on behavioral freezing was tested during unconditioned exploration, fear memory acquisition (i.e. conditioning), and recent and remote contextual fear memory recall. Group treatments were balanced in the following way: half of mice (n=4/group) were assigned CNO or vehicle treatment during a novel context exploration, prior to any fear chamber context exposure. After contextual fear chamber habituation, CNO was given to one group of animals (n=4) and vehicle was given to the other (n=4) during conditioning. Contextual fear memory testing 3 days later administered CNO and vehicle in swapped animal groups from the conditioning day. Group administration was further swapped at the 10-day remote memory test. Using this paradigm, within subject effects of CNO-induced silencing can be compared across testing days, and between subject treatment effects can be compared at each testing day. Additionally, this schedule minimizes CNO exposure for all mice. Conditioning

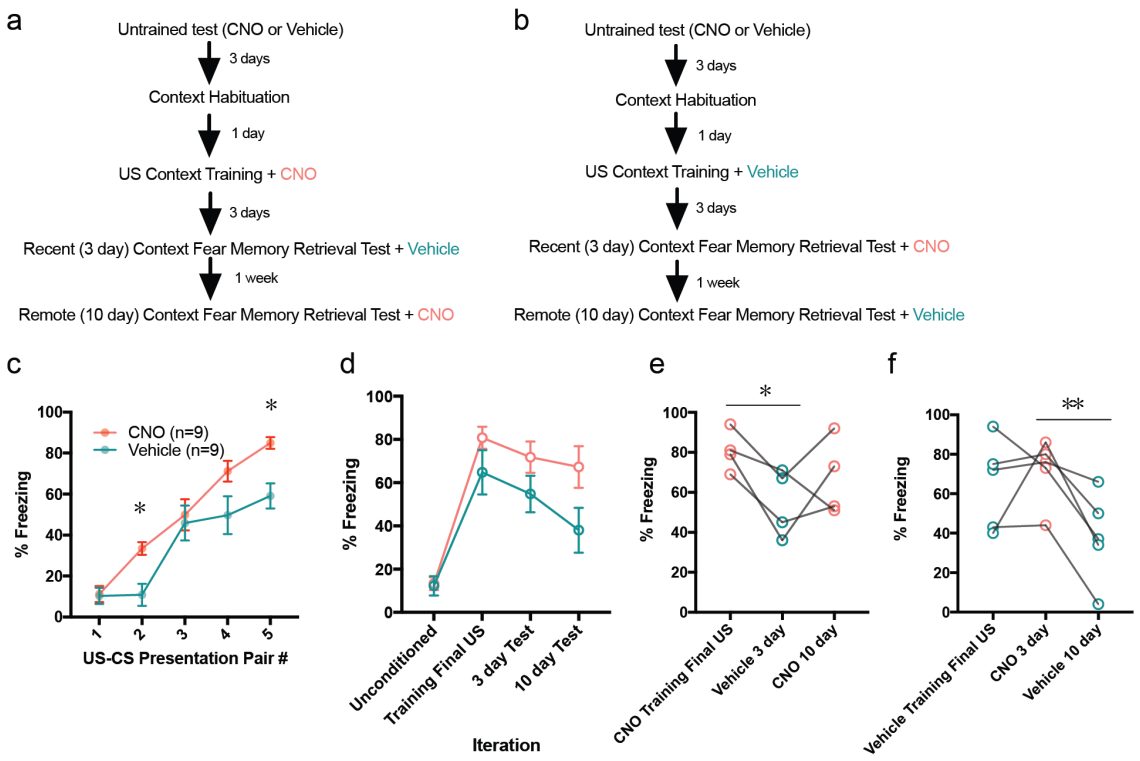

Figure 37. Acute loss of *biGrb10+* vlPAG neuron function during unconditioned and conditioned fear memory retrieval. a-b) Schedule of testing and treatments for the two groups of experimental mice (n=4/group). c) Percent freezing during fear memory acquisition. d) Percent freezing during unconditioned and conditioned testing days. e) Percent freezing in individual mice from treatment schedule a). f) Percent freezing displayed amongst individual mice from treatment schedule b)

data from a separate but similar protocol experiment was combined with the groups tested on the treatment schedule (n=9 total for conditioning test; n=4 all other tests). The results during fear conditioning revealed a significant main effect of treatment ($F(1,16) = 6.722$, $p=0.0196$), with CNO-treated animals overall freezing more (50% CNO, 35% vehicle) throughout all conditioning CS presentations. Post-hoc testing indicated significantly increased freezing in CNO-treated mice specifically at the second ($p=0.0439$) and fifth ($p=0.015$) CS presentations (Figure 37, c). A between-subject 2 (treatment) x 4 (testing iteration) two-way ANOVA identified a significant main effect of treatment

(F(1,27) = 7.332, p= 0.0116) with CNO treatment causing overall more freezing (58% CNO, 43% vehicle) across testing days (Figure 37, d). Significant testing day differences amongst treatment groups were not found in post-hoc testing, although a trend for CNO-induced freezing enhancement was seen only in conditioned and not unconditioned tests (Figure 37, d). Paired t-tests amongst freezing levels at all 3 testing days revealed that CNO treatment prevented time-dependent decreases in retrieval-specific freezing. Specifically, animals receiving CNO on training day and on the 10 day remote memory test displayed a significant drop (t(3) = 3.84, p = 0.031) in freezing only on day 3 testing (Figure 37, e). Thus, 10-day-old remote fear memory freezing levels were increased by CNO treatment to maximal levels displayed during fear memory acquisition. Conversely, animals receiving CNO on the day 3 test prevented significant loss of freezing from training day levels seen in the other scheduled treatment group. Instead, a significant loss (t(4) =4.862, p =0.0083) of freezing levels from 3 to 10 day-old remote memory testing was observed (Figure 37, f). Altogether, the combined results of two separate loss-of-function manipulations support a role of vlPAG *biGrb10+* neurons in conditioned freezing responses by specifically controlling fear memory retrieval-coupled freezing at all memory stages tested.

4. Discussion

The purpose of the experiments described in this chapter was to identify and characterize novel behavioral circuits based on the whole-brain imprint status of *Grb10*. Novel PO-specific dual-colored reporter mice were created for

unbiased identification and access into putative behavioral functions of identified *Grb10* expressing cell types and circuts. My main findings illustrate 1) the ability of each *Grb10* allele to highlight separate brain systems of behavioral function, and 2) the identification and initial description of a novel vlPAG circuit that may participate in controlling fear memory retrieval-evoked freezing behavior.

The paternal copy of *Grb10* largely dominated allelic expression in the brain, specifically in subcortical areas. This result replicates previous work using transgenic LacZ expression reporting from a paternal knockout allele (Garfield et al., 2011). Top *patGrb10*-expressing regions identified by whole-brain microscopy also resembled Garfield et al results, with additional regions and cells being labeled, presumably due to higher signal sensitivity of H2B-FP-reporting alleles and our automated whole-brain imaging method (Garfield et al., 2011). Particularly, notable cortical expression in layers 2-2/3 of the retrosplenial cortex and spatial encoding areas of the hippocampus (PRE, POST, ENTmv) contained a prominent *patGrb10*-positive neuronal population that has not been described before.

Top *patGrb10*+-expressing ROIs were identified by unbiased screens and defined a network of regions relating to several aspects of stress behavior. Importantly, ROIs with shared functions collectively represent modalities of anxiety/fear (BNST, LSv, MH, PVT, RE, DR, PAG, CeAl, BMA, LC, LDT, PB, EW) (Adhikari et al., 2015; Gaszner et al., 2012; Okamoto and Aizawa, 2013; Penzo et al., 2015; Tovote et al., 2015; Yang et al., 2016), threat detection (NLOT, CoAa, MeAav, NPT, OP, PPT, NPC, SC, PAG) (Pereira and Moita,

2016), aggression (VMH, PMv, MPN, SPA, PAG, BNST, LSv) (Motta et al., 2013; Nelson and Trainor, 2007; Roberts and Nagel, 1996), homeostatic/autonomic control (DMH, PVHm, VMH, NTS, DMX, B) (Gao and Horvath, 2008; Sved et al., 2002), and spatial memory/processing (PRE, POST, ENTmv, RSP2-2/3) (Fanselow and Dong, 2010). This functional organization coupled with the overall broad subcortical expression of the paternal Grb10 allele may reflect a top-down, connectivity-based control over the *patGrb10*-tagged network.

The medial prefrontal cortex (mPFC), consisting of the anterior cingulate (AC), infralimbic (IL), and PL (PL) cortices, represents a potentially connected cortical source linking modular *patGrb10* expression patterns. The mPFC provides inhibition of stress-responsive limbic and brainstem structures (Maier et al., 2006). Converging evidence from two separate studies implicate mPFC control over behavioral selection to stress/challenge (Amat et al., 2005; Warden et al., 2012). In both cases, mPFC's ability to guide behavioral sequelae was dependent on its interaction with the DR – another top *patGrb10*+ brain region. At the amygdala, a ventral mPFC → basomedial amygdala (BMA) connection was shown to provide top-down control over anxiety state and conditioned fear (Adhikari et al., 2015). Additionally, mPFC stimulation can also inhibit conditioned fear responses through the central amygdala (CeA) (Quirk et al., 2003). Subdivisions of each amygdalar structure were top *patGrb10*+ ROIs, with the BMAa being the densest ROI in the cortical subplate, and the CeAl as the most dense amygdalar structure from the cerebral nuclei. In combination with my data, these studies offer support to the notion of an mPFC efferent link with the

patGrb10-defined behavioral system reported. Whole-brain efferent mapping from multiple mPFC locations within *patGrb10*-reporter mice will uncover the extent of this possible relationship in future studies.

matGrb10+ brain expression was largely restricted to vasculature-related cell types (e.g. pericytes, endothelial cells, ependymal cells), suggesting a very different cellular function than that of the *patGrb10* allele. However, maternal/paternal isoform-specific differences in Grb10 protein function remain uncharacterized (Plasschaert and Bartolomei, 2015). This PO-specific cell type segregation of allelic expression also indicates that somatic *Grb10* expression of each allele is dependent upon cell type-specific chromatin states. This complements the results of past epigenetic/molecular studies which identified cell type-specific epigenetic changes at paternal and maternal promoters of *Grb10* (discussed in introduction)(Sanz et al., 2008; Yamasaki-Ishizaki et al., 2007). Garfield et al identified prenatal *matGrb10+* expression in the same non-neuronal cell types, with no expression seen post-natally (Garfield et al., 2011). Their results also documented *matGrb10+* expression in peripheral tissues of mesoderm (kidney) and endodermal (liver) origin, again supporting cell type-dependent epigenetic changes at the *Grb10* locus. While peripheral tissue expression was not examined in my studies, the brain *matGrb10+* expression differences between my results and the Garfield study likely reflect sensitivity of the detection assays used. As mentioned previously, my H2B-FP-tagged reporter system with STPT 2-photon detection is likely to offer much greater sensitivity than bright-field imaging of *LacZ* stained sections. It is worth mentioning that

antibody detection of Grb10 protein shadowed *patGrb10* reporter patterns but failed to detect protein in the vasculature-related *matGrb10+* cell types. This discrepancy could be related to a number of possibilities that were not addressed in the staining-based reporter validation experiments. Such possibilities include paternal isoform preferred antigenicity, disproportionate *matGrb10* transcription to protein production with protein levels being lower than antibody detection limits, or expression leak from the MatGrb10 allele in my experiments. My ongoing experiments aim to clarify this issue through reporter expression validation with allele-specific fluorescent in-situ hybridizations (FISH) in the reporter mice.

Apparent loss of *matGrb10* imprinting, resulting in biallelic expression, in a small population of neurons was observed in my experiments. The *biGrb10+* cells, to my knowledge, have not been documented previously. Major regions identified to comprise these neurons were the periventricular nucleus of the hypothalamus (PVi), a region involved in maternal behavior (Larsen and Grattan, 2012), the anterior pretectal nucleus (APN), a region assigned to antinociception (Brandao et al., 1991) and the vlPAG, an overall defensive behavior center (Vianna and Brandao, 2003). Additional minor populations were seen in the medial septum (MS) and nucleus of solitary tract (NTS), but were not characterized in the current experiments due to their sparseness.

The vlPAG population represent the most abundant *biGrb10+* neuron-containing region. For this reason, and also due to the subdivision specificity of expression and the vlPAG's specialized function in freezing behavior, I decided

to investigate this population further (Tovote et al., 2015). Cell type identification, anterograde tracing, and behavioral studies revealed unique traits of this population that distinguish it from other known cells of the vlPAG. First, sparse periaqueductal VIP+/GAD2- neurons were enriched with *biGrb10* expression and represented the major source of bilateral ovBNST afferents from the vlPAG. This specific connection was previously examined in Slc6a3-Cre mice, in which VIP was expressed in Slc6a3-recombined cells (Poulin et al., 2014) which are presumptive dopaminergic neurons. In my hands, TH staining experiments did not label the *biGrb10*+ neurons in vlPAG, even though this cell population comprises ~70% of VIP+ neurons. This discrepancy may be related to lower sensitivity of detection in staining versus genetic Cre-mediated recombination. The loss *Grb10* maternal imprinting in the majority of the VIP+ cells combined with their very specific projections suggests an involvement of *Grb10* in behavioral functions of the vlPAG region. Second, approximately 50% of *biGrb10*+ neurons were GAD2+ and these neurons mainly innervated the midline thalamic structures and the CeAl. These projections are similar to the projections of the vlPAG neurons described in previous studies (Vianna and Brandao, 2003). However, the GAD2+ identity of some/all of these projections was not known. Lastly, chemogenetically inhibition of the total population during fear memory retrieval potentiates the freezing response. vlPAG is affiliated with pro-freezing output during fear learning (McDannald, 2010; Schenberg et al., 2005; Vianna and Brandao, 2003), which has recently been linked to local GABAeric control of glutamatergic neurons in the unconditioned state (Tovote et al., 2016). I cannot

rule out that *biGrb10+* locally connect with glutamatergic output neurons. However, DREADD silencing in the unconditioned mice failed to generate increased freezing, suggesting fear memory-retrieval linked freezing control by the *biGrb10+* neurons. To what extent the VIP+ population controls this affect will be tested in the near future using similar loss-of-function experiments. This will also address the relevance of the ovBNST vlPAG connection in this behavioral effect.

In conclusion, the allelic choice of imprinted *Grb10* expression revealed new insights into system-specific roles of imprinting in behaviors. Ongoing studies are aimed to further characterize the VIP+ vlPAG population and other *biGrb10+* populations will be explored to search for more circuit-relevant roles in the brain.

Chapter V. General Discussion

The overarching goal of my thesis was to characterize patterns of brain imprinting and to understand how these epigenetic gene regulations may affect behavior.

I investigated this problem between two forms of imprinting, XCI and genomic autosomal imprinting. Patterns of whole brain XCI were characterized in chapter II and the results, demonstrating a brainwide bias towards inactivation of the paternal X chromosome, were found to have novel and significant consequences for the penetrance of the deletion of the Fragile X gene in the FXS mouse model, as described in chapter III. The finding of ~12.5% (or ~2.5 million cell) maternal XCa: paternal XCi bias was maintained across the left-right axis and within all regions of the brain. This result is supported by previous XCI brain estimations of 6-19% based on other approaches (Gregg et al., 2010; McMahon et al., 1983; Wang et al., 2010) that did not have the spatial resolution of our assays. Interestingly, the brain-to-brain XCI variability was fairly large, with a range of 25-75% whole-brain XCa. Within this variability, I observed a whole-brain to individual region XCa correlation, suggesting that XCa at the level of individual brain regions can be predicted by the overall whole-brain status (though see below for discussion of subtle intra-brain differences XCI differences, at least with respect to the penetration of X-linked mutations). The overall

agreement between whole brain and regional XCI points towards developmental XCI selection in one of three possible modes: pre-gastrulation, gastrulation-dependent, or post-gastrulation (Figure 38). Specifically, pre-gastrulation selection would describe completion of XCI selection prior to gastrulation with a currently unknown factor biasing inactivation towards the Xp. Support for this case would be found in the examination of XCI ratios within other germ layer-derived tissues. Similar bias in XCI in mesoderm and endoderm derivatives would support this model and maternal XCa bias would be ascribed towards the embryo as a whole, and not just that of the brain. Pre-implantation silencing of the Xp may affect post-implantation XCi choice (Huynh and Lee, 2003; Lee and Bartolomei, 2013), supporting this mode of brain selection. However, a mechanism to this effect has yet to be revealed. Gastrulation-dependent brain XCI selection would set XCI ratios during the time of ectoderm differentiation, meaning that XCI choice occurs through the gastrulation process itself. Selection and bias could therefore be directed by differentiation-specific factors that may influence other germ layer ratios as well. Lastly, post-gastrulation selection would correspond to post XCI setting in which differentiation, proliferation, and/or developmental processes select for more maternal XCa in the brain. While all modes of brain XCI selection are equally possible, future mechanistic and developmental descriptions are needed to clarify the selection modes of brain-specific, non-random XCI. I am currently investigating these question in ongoing experiments.

In the subsequent chapter III I examined behavioral consequences of brain XCI on the penetrance of an X-linked mutation. Specifically, penetrance in heterozygous FXS mice was studied in the context of the inheritance of the mutation either from the maternal or paternal side. The behaviors examined in these mice included novel open arena exploration, working spatial memory, and social behavior. In agreement with more maternal XCa cells in normal wild type brain, the maternal heterozygous KO, but not paternal heterozygous KO, showed a deficit in each of these tests, with the strongest phenotype observed for the social behavior-based test. Analysis of the whole-brain XCI status in these mice confirmed the predicted persistent bias in maternal XCa in the presence of one mutant FMR1 copy. This suggests that the greater mutant FMR1 cell density in maternal versus paternal KO heterozygotes is the cause for the penetrance of the FXS phenotype. These data also suggest that the overall presence of >50% of cells with the wild type FMR1 gene in the paternal KO heterozygous mice is sufficient to compensate ("buffer-out") the genetic lesion in the female brains. Next I examined the XCa ratios in the female heterozygous FXS mice across brain areas and compared these local ratios to the animals' behavioral performance. My prediction was that an XCa distribution across brain regions and neuronal circuits in individual mice could influence the extent of their behavioral dysfunctions. The extent of social avoidance – a human FXS symptom in females (Williams et al., 2014) – was significantly correlated to XCI-based mutant cell distributions across a network of interconnected brain regions known to regulate social behaviors. This neural circuit contained the MPOA,

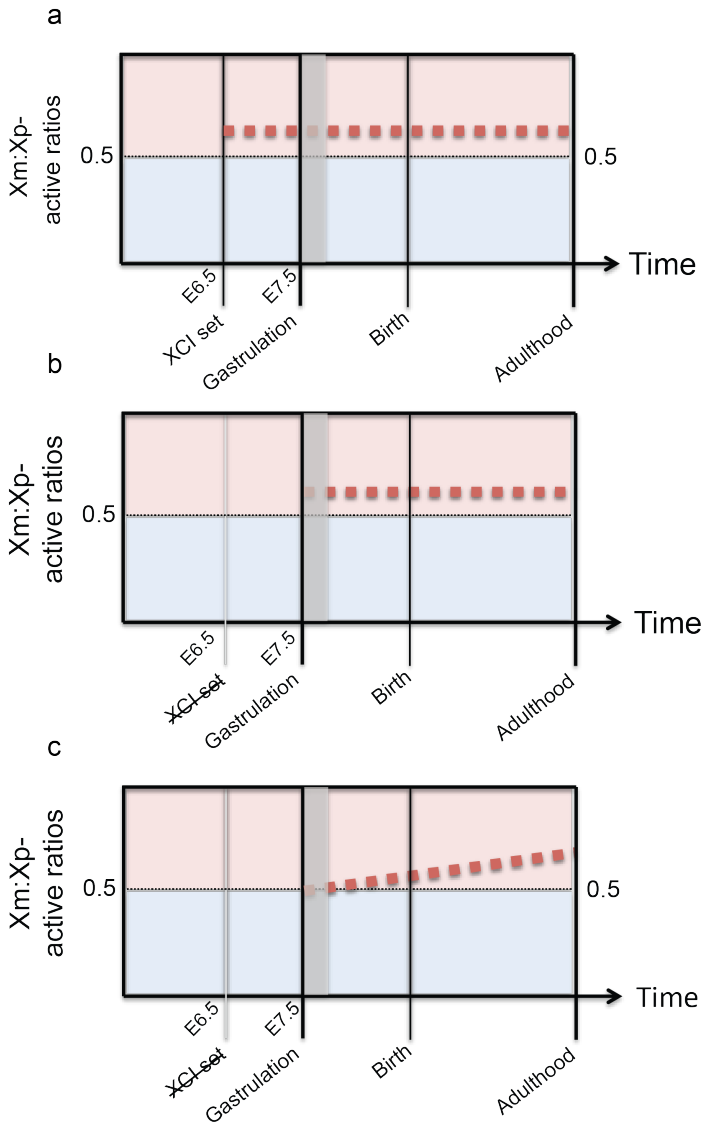

Figure 38. Proposed brain XCI modes of selection. Unidentified factor/s causing maternally biased brain XCa throughout the whole brain can be selected for in 3 possible modes: a) upon implantation at E6.5, the bias is predetermined, stable throughout development, and affects all tissues, b) the differentiation of the ectoderm selects for the bias, c) post-gastrulation selection throughout postnatal development occurs due to differentiation, proliferation, and/or other developmental effects favoring the Xm. Red dotted line indicates average ratios of Xm/Xp-active brain cells with ending adult ratios experimentally defined in my thesis

ENTm, BST, BLA, and COAp. In addition, the percent center distance traveled in an open field was also correlated to healthy XCa cell density in a sensorimotor interconnected network of brain regions. This circuit contained multiple sensory

hindbrain and thalamic regions as well as areas of sensorimotor integration including the NDB, GP, VLPO, and MA.

These results thus suggest that the maternal and paternal XCa distribution can vary between brain regions within individual brains, resulting in some animals with a higher FXS KO-XCa cell density in regions linked to social behavior and in others in regions linked to non-social exploration. The X-linked behavioral deficits in female FXS mice thus act through 1) a global brain XCI bias favoring maternal XCa, and 2) intra-brain XCI variability across behavioral circuits. These results could also explain the broad phenotypic range of FXS and other X-linked brain disorders in female patients, as each patient would be predicted to carry a unique overall and local distribution of cells carrying the mutant versus the healthy X chromosome.

In summary, my thesis work presents the first report of PO effects in female X-linked disease penetrance, implicating paternal XCI bias as the basis for higher penetrance of maternal inherited X-linked mutations. Whether similar XCI-based penetrance in other X-linked disorders exists is yet to be tested experimentally nor has it been described, to my knowledge, clinically. In addition to FXS, other female X-linked forms of brain dysfunction include the Rett syndrome (Weaving et al., 2005), Christianson syndrome (Christianson et al., 1999), Turner syndrome (Lepage et al., 2013), and over 20 forms of X-linked mental retardation (XLMR) (Plenge et al., 2002). Therefore, research using other X-linked mouse models and experimental approaches similar to the one used in

my work, will likely help to understand the translatability of my results to other X-linked brain disease states.

In the second part of my thesis I examined genomic imprinting on an autosomal chromosome, focusing on the imprinted gene *Grb10*. I devised a dual-color, PO-specific genetic reporting approach for comprehensive mapping of the expression of the maternal and paternal Grb10 allele. This strategy allowed me to examine whole-brain allelic compositions in cells of *Grb10* expression. Allelic composition within identified *Grb10*-expressing cells existed in 3 varieties throughout the brain: 1) paternal in neurons of a broad and diffuse subcortical network, 2) maternal in vasculature-related cell-types, and 3) biallelic (i.e. reflecting a loss of maternal imprint) in neurons of several distinct subcortical regions. This finding partially overlapped with previous work in which paternal-expressing *Grb10*+ cells were reported in a similar subcortically defined fashion (Garfield et al., 2011). The differences amongst reported expression were discussed previously (see chapter IV), and likely relate to detection sensitivity and/or genetic design of the two reporter systems. Particularly, the Garfield described expression of *Grb10* was reported of a knockout allele, potentially causing genetic compensation of some form or another form of dysregulation due to the dysfunctional allele. In other words, the nature of the expression reported may not represent endogenous levels and location faithfully. A main principle behind the genetic approach used in my thesis was to retain *Grb10* function and expression due to the presumed sensitivity of gene dosage in *Grb10*-expressing cells. This was primarily achieved through the engineering of 3' in-frame bi or

tricistronic expression of reporter cassettes. The system created in my thesis, to my knowledge, is the first example of a gene non-disruptive reporting system used to dissect imprinted gene expression.

The PO-specific *Grb10* expression amongst cell types is most likely regulated by epigenetic differences within the promoter regions of *Grb10* (Plasschaert and Bartolomei, 2015; Sanz et al., 2008; Yamasaki-Ishizaki et al., 2007). For example, bivalent H3K4me2 and H3K27me3 marks at the paternal promoter associate with non-neuronal somatic cells and therefore may be found in the maternal *Grb10*+ (including the biallelic cells) I report (Sanz et al., 2008). The novel *Grb10*-FP-reporting mice developed for this thesis enable further characterization into the potential epigenetic and transcriptomic distinctions within each *Grb10*+ population. Accordingly, fluorescent activated cell sorting (FACS) of the different *Grb10*+ populations followed by chromatin immunoprecipitation (ChIP) or RNAseq can evaluate epigenetic differences at the promoter and survey transcriptome-wide differences, respectively.

Whole-brain cell density mapping using the Ostan lab imaging and computational methods enabled a classification of major *patGrb10*+ expression brain areas. These regions can broadly be defined as stress-related networks, where multiple behavioral functions can be ascribed across the network, such as anxiety/fear, threat detection, aggression, homeostatic/autonomic function, and spatial memory/processing. This anatomical-based functional classification combined with the broad, non-cell type-specific *patGrb10*+ expression seen in the top ROIs suggested a connectivity-based network, and particularly from that

of a top-down influence, such as the mPFC. While the thesis did not experimentally address this hypothesis, I plan to test mPFC connectivity amongst the *patGrb10*+network using anterograde delivery of *AAV1-Cre* into the mPFC of *patGrb10-H2B-tdTomato/Rosa26-LSL-H2B-GFP* double transgenic mice. *AAV1-Cre*'s ability to transynaptically infect and express in target cells (Zingg et al., 2017) will be used to report connections with H2B-EGFP fluorescence. Whole-brain imaging and double positive cell counting will quantify the degree cells infected at mPFC injection site connect to *patGrb10*+ brain areas. If high correspondence is found, further characterization of the developmental course of connections and its regulation over *patGrb10*+ expression will be studied. Additionally, groundwork will be laid for the molecular characterization of connectivity-defined regulation over the *patGrb10* allele. In support of this mPFC-based connectivity hypothesis, in-silico screens of connectivity (via Allen Brain Connectivity database) amongst IL and PL with *patGrb10*+ nodes identified a high percentage of hits, providing some support for this hypothesized *patGrb10*+ brain network model.

In addition to the *patGrb10*-defined brain expression, another circuit-based pattern of expression was observed in discreet clusters of *biGrb10*+ neurons surrounded by larger numbers of monoallelic *patGrb10*+ neurons in several subcortical brain areas. The combination of both allele's expression in neurons indicated a loss of *Grb10* maternal imprinting and therefore epigenetic distinction within these cells. As discussed above, FACS-based ChIP, ChIPseq and RNAseq studies in the future can be used to look in-depth at any molecular

distinction these cells contain. The 3 main areas containing *biGrb10*+ cells included the periventricular hypothalamus, anterior pretectal nucleus, and the vlPAG. Density of these cells was greatest in the vlPAG – a subcolumn specialized in freezing behavior (Johansen et al., 2010; McNally et al., 2011) and the vlPAG population was defined as ovBNST-projecting VIP+/GAD2- and midline thalamus and amygdala-projecting GAD2+ neurons. Cellular acute or chronic loss-of-function manipulations in the mixed population enhanced conditioned freezing responses to contextual and cued fear memory retrieval, respectively. This effect was demonstrated during learning and maintained up to 10 days after acquisition of the fear memory. Failure to enhance freezing during an unconditioned novel arena test supported a separate function of these cells than what has recently been functionally reported amongst the entire GABAergic population (Tovote et al., 2016). Ongoing studies are aimed at understanding the inputs of this population, the contribution of each subpopulation (i.e. VIP+ or GAD2+) in behavior, and the effects of artificial activation in the entire population during behavior.

Concluding Remarks

Imprinting – in XCI and genomic forms – assigns cellular gene dosage based on parent-of-origin. My dissertation describes the phenotypic power imprinted neurons bestow upon behavior due to brain patterns of expression. For XCI, the patterning due to a maternally biased, yet variable choice governs

behavioral X-linked disease susceptibility. And in genomic imprinting, the stereotyped choice in neural circuits is likely to regulate various behaviors. In conclusion, this work opens the doors to future brain systems level inquiries amongst X-linked disease penetrance and imprinted rules of behavior.

Table 1: List of assayed ROIs and acronyms

Name	Acronym
root	root
Basic cell groups and regions	grey
Cerebrum	CH
Cerebral cortex	CTX
Cortical plate	CTXpl
Isocortex	Isocortex
Frontal pole, cerebral cortex	FRP
Frontal pole, layer 1	FRP1
Frontal pole, layer 2/3	FRP2/3
Somatomotor areas	MO
Somatomotor areas, Layer 1	MO1
Somatomotor areas, Layer 2/3	MO2/3
Somatomotor areas, Layer 5	MO5
Somatomotor areas, Layer 6a	MO6a
Primary motor area	MOp
Primary motor area, Layer 1	MOp1
Primary motor area, Layer 2/3	MOp2/3
Primary motor area, Layer 5	MOp5
Primary motor area, Layer 6a	MOp6a
Primary motor area, Layer 6b	MOp6b
Secondary motor area	MOs
Secondary motor area, layer 1	MOs1
Secondary motor area, layer 2/3	MOs2/3
Secondary motor area, layer 5	MOs5
Secondary motor area, layer 6a	MOs6a
Secondary motor area, layer 6b	MOs6b
Somatosensory areas	SS
Somatosensory areas, layer 1	SS1
Somatosensory areas, layer 2/3	SS2/3
Somatosensory areas, layer 4	SS4
Somatosensory areas, layer 5	SS5
Somatosensory areas, layer 6a	SS6a
Somatosensory areas, layer 6b	SS6b
Primary somatosensory area	SSp
Primary somatosensory area, layer 1	SSp1
Primary somatosensory area, layer 2/3	SSp2/3
Primary somatosensory area, layer 4	SSp4
Primary somatosensory area, layer 5	SSp5
Primary somatosensory area, layer 6a	SSp6a
Primary somatosensory area, layer 6b	SSp6b
Primary somatosensory area, nose	SSp-n
Primary somatosensory area, nose, layer 1	SSp-n1

Primary somatosensory area, nose, layer 2/3	SSp-n2/3
Primary somatosensory area, nose, layer 4	SSp-n4
Primary somatosensory area, nose, layer 5	SSp-n5
Primary somatosensory area, nose, layer 6a	SSp-n6a
Primary somatosensory area, nose, layer 6b	SSp-n6b
Primary somatosensory area, barrel field	SSp-bfd
Primary somatosensory area, barrel field, layer 1	SSp-bfd1
Primary somatosensory area, barrel field, layer 2/3	SSp-bfd2/3
Primary somatosensory area, barrel field, layer 4	SSp-bfd4
Primary somatosensory area, barrel field, layer 5	SSp-bfd5
Primary somatosensory area, barrel field, layer 6a	SSp-bfd6a
Primary somatosensory area, barrel field, layer 6b	SSp-bfd6b
Primary somatosensory area, lower limb	SSp-ll
Primary somatosensory area, lower limb, layer 1	SSp-ll1
Primary somatosensory area, lower limb, layer 2/3	SSp-ll2/3
Primary somatosensory area, lower limb, layer 4	SSp-ll4
Primary somatosensory area, lower limb, layer 5	SSp-ll5
Primary somatosensory area, lower limb, layer 6a	SSp-ll6a
Primary somatosensory area, lower limb, layer 6b	SSp-ll6b
Primary somatosensory area, mouth	SSp-m
Primary somatosensory area, mouth, layer 1	SSp-m1
Primary somatosensory area, mouth, layer 2/3	SSp-m2/3
Primary somatosensory area, mouth, layer 4	SSp-m4
Primary somatosensory area, mouth, layer 5	SSp-m5
Primary somatosensory area, mouth, layer 6a	SSp-m6a
Primary somatosensory area, mouth, layer 6b	SSp-m6b
Primary somatosensory area, upper limb	SSp-ul
Primary somatosensory area, upper limb, layer 1	SSp-ul1
Primary somatosensory area, upper limb, layer 2/3	SSp-ul2/3
Primary somatosensory area, upper limb, layer 4	SSp-ul4
Primary somatosensory area, upper limb, layer 5	SSp-ul5
Primary somatosensory area, upper limb, layer 6a	SSp-ul6a
Primary somatosensory area, upper limb, layer 6b	SSp-ul6b
Primary somatosensory area, trunk	SSp-tr
Primary somatosensory area, trunk, layer 1	SSp-tr1
Primary somatosensory area, trunk, layer 2/3	SSp-tr2/3
Primary somatosensory area, trunk, layer 4	SSp-tr4
Primary somatosensory area, trunk, layer 5	SSp-tr5
Primary somatosensory area, trunk, layer 6a	SSp-tr6a
Primary somatosensory area, trunk, layer 6b	SSp-tr6b
Supplemental somatosensory area	SSs
Supplemental somatosensory area, layer 1	SSs1
Supplemental somatosensory area, layer 2/3	SSs2/3
Supplemental somatosensory area, layer 4	SSs4
Supplemental somatosensory area, layer 5	SSs5
Supplemental somatosensory area, layer 6a	SSs6a
Supplemental somatosensory area, layer 6b	SSs6b
Infralimbic area	ILA
Infralimbic area, layer 1	ILA1

Infralimbic area, layer 2	ILA2
Infralimbic area, layer 2/3	ILA2/3
Infralimbic area, layer 5	ILA5
Infralimbic area, layer 6a	ILA6a
Infralimbic area, layer 6b	ILA6b
Gustatory areas	GU
Gustatory areas, layer 1	GU1
Gustatory areas, layer 2/3	GU2/3
Gustatory areas, layer 4	GU4
Gustatory areas, layer 5	GU5
Gustatory areas, layer 6a	GU6a
Gustatory areas, layer 6b	GU6b
Visceral area	VISC
Visceral area, layer 1	VISC1
Visceral area, layer 2/3	VISC2/3
Visceral area, layer 4	VISC4
Visceral area, layer 5	VISC5
Visceral area, layer 6a	VISC6a
Visceral area, layer 6b	VISC6b
Auditory areas	AUD
Dorsal auditory area	AUDd
Dorsal auditory area, layer 1	AUDd1
Dorsal auditory area, layer 2/3	AUDd2/3
Dorsal auditory area, layer 4	AUDd4
Dorsal auditory area, layer 5	AUDd5
Dorsal auditory area, layer 6a	AUDd6a
Dorsal auditory area, layer 6b	AUDd6b
Primary auditory area	AUDp
Primary auditory area, layer 1	AUDp1
Primary auditory area, layer 2/3	AUDp2/3
Primary auditory area, layer 4	AUDp4
Primary auditory area, layer 5	AUDp5
Primary auditory area, layer 6a	AUDp6a
Primary auditory area, layer 6b	AUDp6b
Posterior auditory area	AUDpo
Posterior auditory area, layer 1	AUDpo1
Posterior auditory area, layer 2/3	AUDpo2/3
Posterior auditory area, layer 4	AUDpo4
Posterior auditory area, layer 5	AUDpo5
Posterior auditory area, layer 6a	AUDpo6a
Posterior auditory area, layer 6b	AUDpo6b
Ventral auditory area	AUDv
Ventral auditory area, layer 1	AUDv1
Ventral auditory area, layer 2/3	AUDv2/3
Ventral auditory area, layer 4	AUDv4
Ventral auditory area, layer 5	AUDv5
Ventral auditory area, layer 6a	AUDv6a
Ventral auditory area, layer 6b	AUDv6b
Visual areas	VIS

Visual areas, layer 1	VIS1
Visual areas, layer 2/3	VIS2/3
Visual areas, layer 4	VIS4
Visual areas, layer 5	VIS5
Visual areas, layer 6a	VIS6a
Visual areas, layer 6b	VIS6b
Anterolateral visual area	VISal
Anterolateral visual area, layer 1	VISal1
Anterolateral visual area, layer 2/3	VISal2/3
Anterolateral visual area, layer 4	VISal4
Anterolateral visual area, layer 5	VISal5
Anterolateral visual area, layer 6a	VISal6a
Anterolateral visual area, layer 6b	VISal6b
Anteromedial visual area	VISam
Anteromedial visual area, layer 1	VISam1
Anteromedial visual area, layer 2/3	VISam2/3
Anteromedial visual area, layer 4	VISam4
Anteromedial visual area, layer 5	VISam5
Anteromedial visual area, layer 6a	VISam6a
Anteromedial visual area, layer 6b	VISam6b
Lateral visual area	VISl
Lateral visual area, layer 1	VISl1
Lateral visual area, layer 2/3	VISl23
Lateral visual area, layer 4	VISl4
Lateral visual area, layer 5	VISl5
Lateral visual area, layer 6a	VISl6a
Lateral visual area, layer 6b	VISl6b
Primary visual area	VISp
Primary visual area, layer 1	VISp1
Primary visual area, layer 2/3	VISp2/3
Primary visual area, layer 4	VISp4
Primary visual area, layer 5	VISp5
Primary visual area, layer 6a	VISp6a
Primary visual area, layer 6b	VISp6b
Posterolateral visual area	VISpl
Posterolateral visual area, layer 1	VISpl1
Posterolateral visual area, layer 2/3	VISpl2/3
Posterolateral visual area, layer 4	VISpl4
Posterolateral visual area, layer 5	VISpl5
Posterolateral visual area, layer 6a	VISpl6a
Posterolateral visual area, layer 6b	VISpl6b
posteromedial visual area	VISpm
posteromedial visual area, layer 1	VISpm1
posteromedial visual area, layer 2/3	VISpm2/3
posteromedial visual area, layer 4	VISpm4
posteromedial visual area, layer 5	VISpm5
posteromedial visual area, layer 6a	VISpm6a
posteromedial visual area, layer 6b	VISpm6b
Anterior cingulate area	ACA

Anterior cingulate area, layer 1	ACA1
Anterior cingulate area, layer 2/3	ACA2/3
Anterior cingulate area, layer 5	ACA5
Anterior cingulate area, layer 6a	ACA6a
Anterior cingulate area, layer 6b	ACA6b
Anterior cingulate area, dorsal part	ACAd
Anterior cingulate area, dorsal part, layer 1	ACAd1
Anterior cingulate area, dorsal part, layer 2/3	ACAd2/3
Anterior cingulate area, dorsal part, layer 5	ACAd5
Anterior cingulate area, dorsal part, layer 6a	ACAd6a
Anterior cingulate area, dorsal part, layer 6b	ACAd6b
Anterior cingulate area, ventral part	ACAv
Anterior cingulate area, ventral part, layer 1	ACAv1
Anterior cingulate area, ventral part, layer 2/3	ACAv2/3
Anterior cingulate area, ventral part, layer 5	ACAv5
Anterior cingulate area, ventral part, 6a	ACAv6a
Anterior cingulate area, ventral part, 6b	ACAv6b
Prelimbic area	PL
Prelimbic area, layer 1	PL1
Prelimbic area, layer 2	PL2
Prelimbic area, layer 2/3	PL2/3
Prelimbic area, layer 5	PL5
Prelimbic area, layer 6a	PL6a
Prelimbic area, layer 6b	PL6b
Orbital area	ORB
Orbital area, layer 1	ORB1
Orbital area, layer 2/3	ORB2/3
Orbital area, layer 5	ORB5
Orbital area, layer 6a	ORB6a
Orbital area, layer 6b	ORB6b
Orbital area, lateral part	ORBl
Orbital area, lateral part, layer 1	ORBl1
Orbital area, lateral part, layer 2/3	ORBl2/3
Orbital area, lateral part, layer 5	ORBl5
Orbital area, lateral part, layer 6a	ORBl6a
Orbital area, lateral part, layer 6b	ORBl6b
Orbital area, medial part	ORBm
Orbital area, medial part, layer 1	ORBm1
Orbital area, medial part, layer 2	ORBm2
Orbital area, medial part, layer 2/3	ORBm2/3
Orbital area, medial part, layer 5	ORBm5
Orbital area, medial part, layer 6a	ORBm6a
Orbital area, ventral part	ORBv
Orbital area, ventrolateral part	ORBvl
Orbital area, ventrolateral part, layer 1	ORBvl1
Orbital area, ventrolateral part, layer 2/3	ORBvl2/3
Orbital area, ventrolateral part, layer 5	ORBvl5
Orbital area, ventrolateral part, layer 6a	ORBvl6a
Orbital area, ventrolateral part, layer 6b	ORBvl6b

Agranular insular area	AI
Agranular insular area, dorsal part	AId
Agranular insular area, dorsal part, layer 1	AId1
Agranular insular area, dorsal part, layer 2/3	AId2/3
Agranular insular area, dorsal part, layer 5	AId5
Agranular insular area, dorsal part, layer 6a	AId6a
Agranular insular area, dorsal part, layer 6b	AId6b
Agranular insular area, posterior part	AIp
Agranular insular area, posterior part, layer 1	AIp1
Agranular insular area, posterior part, layer 2/3	AIp2/3
Agranular insular area, posterior part, layer 5	AIp5
Agranular insular area, posterior part, layer 6a	AIp6a
Agranular insular area, posterior part, layer 6b	AIp6b
Agranular insular area, ventral part	AIv
Agranular insular area, ventral part, layer 1	AIv1
Agranular insular area, ventral part, layer 2/3	AIv2/3
Agranular insular area, ventral part, layer 5	AIv5
Agranular insular area, ventral part, layer 6a	AIv6a
Agranular insular area, ventral part, layer 6b	AIv6b
Retrosplenial area	RSP
Retrosplenial area, lateral agranular part	RSPagl
Retrosplenial area, lateral agranular part, layer 1	RSPagl1
Retrosplenial area, lateral agranular part, layer 2/3	RSPagl2/3
Retrosplenial area, lateral agranular part, layer 5	RSPagl5
Retrosplenial area, lateral agranular part, layer 6a	RSPagl6a
Retrosplenial area, lateral agranular part, layer 6b	RSPagl6b
Retrosplenial area, dorsal part	RSPd
Retrosplenial area, dorsal part, layer 1	RSPd1
Retrosplenial area, dorsal part, layer 2/3	RSPd2/3
Retrosplenial area, dorsal part, layer 4	RSPd4
Retrosplenial area, dorsal part, layer 5	RSPd5
Retrosplenial area, dorsal part, layer 6a	RSPd6a
Retrosplenial area, dorsal part, layer 6b	RSPd6b
Retrosplenial area, ventral part	RSPv
Retrosplenial area, ventral part, layer 1	RSPv1
Retrosplenial area, ventral part, layer 2	RSPv2
Retrosplenial area, ventral part, layer 2/3	RSPv2/3
Retrosplenial area, ventral part, layer 5	RSPv5
Retrosplenial area, ventral part, layer 6a	RSPv6a
Retrosplenial area, ventral part, layer 6b	RSPv6b
Posterior parietal association areas	PTLp
Posterior parietal association areas, layer 1	PTLp1
Posterior parietal association areas, layer 2/3	PTLp2/3
Posterior parietal association areas, layer 4	PTLp4
Posterior parietal association areas, layer 5	PTLp5
Posterior parietal association areas, layer 6a	PTLp6a
Posterior parietal association areas, layer 6b	PTLp6b
Temporal association areas	TEa
Temporal association areas, layer 1	TEa1

Temporal association areas, layer 2/3	TEa2/3
Temporal association areas, layer 4	TEa4
Temporal association areas, layer 5	TEa5
Temporal association areas, layer 6a	TEa6a
Temporal association areas, layer 6b	TEa6b
Perirhinal area	PERI
Perirhinal area, layer 6a	PERI6a
Perirhinal area, layer 6b	PERI6b
Perirhinal area, layer 1	PERI1
Perirhinal area, layer 5	PERI5
Perirhinal area, layer 2/3	PERI2/3
Ectorhinal area	ECT
Ectorhinal area/Layer 1	ECT1
Ectorhinal area/Layer 2/3	ECT2/3
Ectorhinal area/Layer 5	ECT5
Ectorhinal area/Layer 6a	ECT6a
Ectorhinal area/Layer 6b	ECT6b
Olfactory areas	OLF
Main olfactory bulb	MOB
Main olfactory bulb, glomerular layer	MOBgl
Main olfactory bulb, granule layer	MOBgr
Main olfactory bulb, inner plexiform layer	MOBipl
Main olfactory bulb, mitral layer	MOBmi
Main olfactory bulb, outer plexiform layer	MOBopl
Accessory olfactory bulb	AOB
Accessory olfactory bulb, glomerular layer	AOBgl
Accessory olfactory bulb, granular layer	AOBgr
Accessory olfactory bulb, mitral layer	AOBmi
Anterior olfactory nucleus	AON
Anterior olfactory nucleus, dorsal part	AONd
Anterior olfactory nucleus, external part	AONe
Anterior olfactory nucleus, lateral part	AONl
Anterior olfactory nucleus, medial part	AONm
Anterior olfactory nucleus, posteroventral part	AONpv
Anterior olfactory nucleus, layer 1	AON1
Anterior olfactory nucleus, layer 2	AON2
Taenia tecta	TT
Taenia tecta, dorsal part	TTd
Taenia tecta, dorsal part, layers 1-4	TTd1-4
Taenia tecta, dorsal part, layer 1	TTd1
Taenia tecta, dorsal part, layer 2	TTd2
Taenia tecta, dorsal part, layer 3	TTd3
Taenia tecta, dorsal part, layer 4	TTd4
Taenia tecta, ventral part	TTv
Taenia tecta, ventral part, layers 1-3	TTv1-3
Taenia tecta, ventral part, layer 1	TTv1
Taenia tecta, ventral part, layer 2	TTv2
Taenia tecta, ventral part, layer 3	TTv3
Dorsal peduncular area	DP

Dorsal peduncular area, layer 1	DP1
Dorsal peduncular area, layer 2	DP2
Dorsal peduncular area, layer 2/3	DP2/3
Dorsal peduncular area, layer 5	DP5
Dorsal peduncular area, layer 6a	DP6a
Piriform area	PIR
Piriform area, layers 1-3	PIR1-3
Piriform area, molecular layer	PIR1
Piriform area, pyramidal layer	PIR2
Piriform area, polymorph layer	PIR3
Nucleus of the lateral olfactory tract	NLOT
Nucleus of the lateral olfactory tract, layers 1-3	NLOT1-3
Nucleus of the lateral olfactory tract, molecular layer	NLOT1
Nucleus of the lateral olfactory tract, pyramidal layer	NLOT2
Nucleus of the lateral olfactory tract, layer 3	NLOT3
Cortical amygdalar area	COA
Cortical amygdalar area, anterior part	COAa
Cortical amygdalar area, anterior part, layer 1	COAa1
Cortical amygdalar area, anterior part, layer 2	COAa2
Cortical amygdalar area, anterior part, layer 3	COAa3
Cortical amygdalar area, posterior part	COAp
Cortical amygdalar area, posterior part, lateral zone	COApl
Cortical amygdalar area, posterior part, lateral zone, layers 1-2	COApl1-2
Cortical amygdalar area, posterior part, lateral zone, layers 1-3	COApl1-3
Cortical amygdalar area, posterior part, lateral zone, layer 1	COApl1
Cortical amygdalar area, posterior part, lateral zone, layer 2	COApl2
Cortical amygdalar area, posterior part, lateral zone, layer 3	COApl3
Cortical amygdalar area, posterior part, medial zone	COApm
Cortical amygdalar area, posterior part, medial zone, layers 1-2	COApm1-2
Cortical amygdalar area, posterior part, medial zone, layers 1-3	COApm1-3
Cortical amygdalar area, posterior part, medial zone, layer 1	COApm1
Cortical amygdalar area, posterior part, medial zone, layer 2	COApm2
Cortical amygdalar area, posterior part, medial zone, layer 3	COApm3
Piriform-amygdalar area	PAA
Piriform-amygdalar area, layers 1-3	PAA1-3
Piriform-amygdalar area, molecular layer	PAA1
Piriform-amygdalar area, pyramidal layer	PAA2
Piriform-amygdalar area, polymorph layer	PAA3
Postpiriform transition area	TR
Postpiriform transition area, layers 1-3	TR1-3
Postpiriform transition area, layers 1	TR1
Postpiriform transition area, layers 2	TR2
Postpiriform transition area, layers 3	TR3
Hippocampal formation	HPF
Hippocampal region	HIP
Ammon's horn	CA
Field CA1	CA1
Field CA1, stratum lacunosum-moleculare	CA1slm
Field CA1, stratum oriens	CA1so

Field CA1, pyramidal layer	CA1sp
Field CA1, stratum radiatum	CA1sr
Field CA2	CA2
Field CA2, stratum lacunosum-moleculare	CA2slm
Field CA2, stratum oriens	CA2so
Field CA2, pyramidal layer	CA2sp
Field CA2, stratum radiatum	CA2sr
Field CA3	CA3
Field CA3, stratum lacunosum-moleculare	CA3slm
Field CA3, stratum lucidum	CA3slu
Field CA3, stratum oriens	CA3so
Field CA3, pyramidal layer	CA3sp
Field CA3, stratum radiatum	CA3sr
Dentate gyrus	DG
Dentate gyrus, molecular layer	DG-mo
Dentate gyrus, polymorph layer	DG-po
Dentate gyrus, granule cell layer	DG-sg
Dentate gyrus, subgranular zone	DG-sgz
Dentate gyrus crest	DGcr
Dentate gyrus crest, molecular layer	DGcr-mo
Dentate gyrus crest, polymorph layer	DGcr-po
Dentate gyrus crest, granule cell layer	DGcr-sg
Dentate gyrus lateral blade	DGlb
Dentate gyrus lateral blade, molecular layer	DGlb-mo
Dentate gyrus lateral blade, polymorph layer	DGlb-po
Dentate gyrus lateral blade, granule cell layer	DGlb-sg
Dentate gyrus medial blade	DGmb
Dentate gyrus medial blade, molecular layer	DGmb-mo
Dentate gyrus medial blade, polymorph layer	DGmb-po
Dentate gyrus medial blade, granule cell layer	DGmb-sg
Fasciola cinerea	FC
Induseum griseum	IG
Retrohippocampal region	RHP
Entorhinal area	ENT
Entorhinal area, lateral part	ENTl
Entorhinal area, lateral part, layer 1	ENTl1
Entorhinal area, lateral part, layer 2	ENTl2
Entorhinal area, lateral part, layer 2/3	ENTl2/3
Entorhinal area, lateral part, layer 2a	ENTl2a
Entorhinal area, lateral part, layer 2b	ENTl2b
Entorhinal area, lateral part, layer 3	ENTl3
Entorhinal area, lateral part, layer 4	ENTl4
Entorhinal area, lateral part, layer 4/5	ENTl4/5
Entorhinal area, lateral part, layer 5	ENTl5
Entorhinal area, lateral part, layer 5/6	ENTl5/6
Entorhinal area, lateral part, layer 6a	ENTl6a
Entorhinal area, lateral part, layer 6b	ENTl6b
Entorhinal area, medial part, dorsal zone	ENTm
Entorhinal area, medial part, dorsal zone, layer 1	ENTm1

Entorhinal area, medial part, dorsal zone, layer 2	ENTm2
Entorhinal area, medial part, dorsal zone, layer 2a	ENTm2a
Entorhinal area, medial part, dorsal zone, layer 2b	ENTm2b
Entorhinal area, medial part, dorsal zone, layer 3	ENTm3
Entorhinal area, medial part, dorsal zone, layer 4	ENTm4
Entorhinal area, medial part, dorsal zone, layer 5	ENTm5
Entorhinal area, medial part, dorsal zone, layer 5/6	ENTm5/6
Entorhinal area, medial part, dorsal zone, layer 6	ENTm6
Entorhinal area, medial part, ventral zone	ENTmv
Entorhinal area, medial part, ventral zone, layer 1	ENTmv1
Entorhinal area, medial part, ventral zone, layer 2	ENTmv2
Entorhinal area, medial part, ventral zone, layer 3	ENTmv3
Entorhinal area, medial part, ventral zone, layer 4	ENTmv4
Entorhinal area, medial part, ventral zone, layer 5/6	ENTmv5/6
Parasubiculum	PAR
Parasubiculum, layer 1	PAR1
Parasubiculum, layer 2	PAR2
Parasubiculum, layer 3	PAR3
Postsubiculum	POST
Postsubiculum, layer 1	POST1
Postsubiculum, layer 2	POST2
Postsubiculum, layer 3	POST3
Presubiculum	PRE
Presubiculum, layer 1	PRE1
Presubiculum, layer 2	PRE2
Presubiculum, layer 3	PRE3
Subiculum	SUB
Subiculum, dorsal part	SUBd
Subiculum, dorsal part, molecular layer	SUBd-m
Subiculum, dorsal part, pyramidal layer	SUBd-sp
Subiculum, dorsal part, stratum radiatum	SUBd-sr
Subiculum, ventral part	SUBv
Subiculum, ventral part, molecular layer	SUBv-m
Subiculum, ventral part, pyramidal layer	SUBv-sp
Subiculum, ventral part, stratum radiatum	SUBv-sr
Cortical subplate	CTXsp
Layer 6b, isocortex	6b
Claustrum	CLA
Endopiriform nucleus	EP
Endopiriform nucleus, dorsal part	EPd
Endopiriform nucleus, ventral part	EPv
Lateral amygdalar nucleus	LA
Basolateral amygdalar nucleus	BLA
Basolateral amygdalar nucleus, anterior part	BLAa
Basolateral amygdalar nucleus, posterior part	BLAp
Basolateral amygdalar nucleus, ventral part	BLAv
Basomedial amygdalar nucleus	BMA
Basomedial amygdalar nucleus, anterior part	BMAa
Basomedial amygdalar nucleus, posterior part	BMAp

Posterior amygdalar nucleus	PA
Cerebral nuclei	CNU
Striatum	STR
Striatum dorsal region	STRd
Caudoputamen	CP
Striatum ventral region	STRv
Nucleus accumbens	ACB
Fundus of striatum	FS
Olfactory tubercle	OT
Islands of Calleja	isl
Major island of Calleja	islm
Olfactory tubercle, layers 1-3	OT1-3
Olfactory tubercle, molecular layer	OT1
Olfactory tubercle, pyramidal layer	OT2
Olfactory tubercle, polymorph layer	OT3
Lateral septal complex	LSX
Lateral septal nucleus	LS
Lateral septal nucleus, caudal (caudodorsal) part	LSc
Lateral septal nucleus, rostral (rostroventral) part	LSr
Lateral septal nucleus, ventral part	LSv
Septofimbrial nucleus	SF
Septohippocampal nucleus	SH
Striatum-like amygdalar nuclei	sAMY
Anterior amygdalar area	AAA
Bed nucleus of the accessory olfactory tract	BA
Central amygdalar nucleus	CEA
Central amygdalar nucleus, capsular part	CEAc
Central amygdalar nucleus, lateral part	CEAl
Central amygdalar nucleus, medial part	CEAm
Intercalated amygdalar nucleus	IA
Medial amygdalar nucleus	MEA
Medial amygdalar nucleus, anterodorsal part	MEAad
Medial amygdalar nucleus, anteroventral part	MEAav
Medial amygdalar nucleus, posterodorsal part	MEApd
Medial amygdalar nucleus, posterodorsal part, sublayer a	MEApd-a
Medial amygdalar nucleus, posterodorsal part, sublayer b	MEApd-b
Medial amygdalar nucleus, posterodorsal part, sublayer c	MEApd-c
Medial amygdalar nucleus, posteroventral part	MEApv
Pallidum	PAL
Pallidum, dorsal region	PALd
Globus pallidus, external segment	GPe
Globus pallidus, internal segment	GPi
Pallidum, ventral region	PALv
Substantia innominata	SI
Magnocellular nucleus	MA
Pallidum, medial region	PALm
Medial septal complex	MSC
Medial septal nucleus	MS
Diagonal band nucleus	NDB

Triangular nucleus of septum	TRS
Pallidum, caudal region	PALc
Bed nuclei of the stria terminalis	BST
Bed nuclei of the stria terminalis, anterior division	BSTa
Bed nuclei of the stria terminalis, anterior division, anterolateral area	BSTal
Bed nuclei of the stria terminalis, anterior division, anteromedial area	BSTam
Bed nuclei of the stria terminalis, anterior division, dorsomedial nucleus	BSTdm
Bed nuclei of the stria terminalis, anterior division, fusiform nucleus	BSTfu
Bed nuclei of the stria terminalis, anterior division, juxtacapsular nucleus	BSTju
Bed nuclei of the stria terminalis, anterior division, magnocellular nucleus	BSTmg
Bed nuclei of the stria terminalis, anterior division, oval nucleus	BSTov
Bed nuclei of the stria terminalis, anterior division, rhomboid nucleus	BSTrh
Bed nuclei of the stria terminalis, anterior division, ventral nucleus	BSTv
Bed nuclei of the stria terminalis, posterior division	BSTp
Bed nuclei of the stria terminalis, posterior division, dorsal nucleus	BSTd
Bed nuclei of the stria terminalis, posterior division, principal nucleus	BSTpr
Bed nuclei of the stria terminalis, posterior division, interfascicular nucleus	BSTif
Bed nuclei of the stria terminalis, posterior division, transverse nucleus	BSTtr
Bed nuclei of the stria terminalis, posterior division, strial extension	BSTse
Bed nucleus of the anterior commissure	BAC
Cerebellum	CB
Cerebellar cortex	CBX
Vermal regions	VERM
Lingula (I)	LING
Lingula (I), molecular layer	LINGmo
Lingula (I), Purkinje layer	LINGpu
Lingula (I), granular layer	LINGgr
Central lobule	CENT
Lobule II	CENT2
Lobule II, molecular layer	CENT2mo
Lobule II, Purkinje layer	CENT2pu
Lobule II, granular layer	CENT2gr
Lobule III	CENT3
Lobule III, molecular layer	CENT3mo
Lobule III, Purkinje layer	CENT3pu
Lobule III, granular layer	CENT3gr
Culmen	CUL
Lobule IV	CUL4
Lobule IV, molecular layer	CUL4mo
Lobule IV, Purkinje layer	CUL4pu
Lobule IV, granular layer	CUL4gr
Lobule V	CUL5
Lobule V, molecular layer	CUL5mo
Lobule V, Purkinje layer	CUL5pu
Lobule V, granular layer	CUL5gr

Lobules IV-V	CUL4, 5
Lobules IV-V, molecular layer	CUL4, 5mo
Lobules IV-V, Purkinje layer	CUL4, 5pu
Lobules IV-V, granular layer	CUL4, 5gr
Declive (VI)	DEC
Declive (VI), molecular layer	DECmo
Declive (VI), Purkinje layer	DECpu
Declive (VI), granular layer	DECgr
Folium-tuber vermis (VII)	FOTU
Folium-tuber vermis (VII), molecular layer	FOTUmo
Folium-tuber vermis (VII), Purkinje layer	FOTUpu
Folium-tuber vermis (VII), granular layer	FOTUgr
Pyramus (VIII)	PYR
Pyramus (VIII), molecular layer	PYRmo
Pyramus (VIII), Purkinje layer	PYRpu
Pyramus (VIII), granular layer	PYRgr
Uvula (IX)	UVU
Uvula (IX), molecular layer	UVUmo
Uvula (IX), Purkinje layer	UVUpu
Uvula (IX), granular layer	UVUgr
Nodulus (X)	NOD
Nodulus (X), molecular layer	NODmo
Nodulus (X), Purkinje layer	NODpu
Nodulus (X), granular layer	NODgr
Hemispheric regions	HEM
Simple lobule	SIM
Simple lobule, molecular layer	SIMmo
Simple lobule, Purkinje layer	SIMpu
Simple lobule, granular layer	SIMgr
Ansiform lobule	AN
Crus 1	ANcr1
Crus 1, molecular layer	ANcr1mo
Crus 1, Purkinje layer	ANcr1pu
Crus 1, granular layer	ANcr1gr
Crus 2	ANcr2
Crus 2, molecular layer	ANcr2mo
Crus 2, Purkinje layer	ANcr2pu
Crus 2, granular layer	ANcr2gr
Paramedian lobule	PRM
Paramedian lobule, molecular layer	PRMmo
Paramedian lobule, Purkinje layer	PRMpu
Paramedian lobule, granular layer	PRMgr
Copula pyramidis	COPY
Copula pyramidis, molecular layer	COPYmo
Copula pyramidis, Purkinje layer	COPYpu
Copula pyramidis, granular layer	COPYgr
Paraflocculus	PFL
Paraflocculus, molecular layer	PFLmo
Paraflocculus, Purkinje layer	PFLpu

Paraflocculus, granular layer	PFLgr
Flocculus	FL
Flocculus, molecular layer	FLmo
Flocculus, Purkinje layer	FLpu
Flocculus, granular layer	FLgr
Cerebellar cortex, molecular layer	CBXmo
Cerebellar cortex, Purkinje layer	CBXpu
Cerebellar cortex, granular layer	CBXgr
Cerebellar nuclei	CBN
Fastigial nucleus	FN
Interposed nucleus	IP
Dentate nucleus	DN
Brain stem	BS
Interbrain	IB
Thalamus	TH
Thalamus, sensory-motor cortex related	DORsm
Ventral group of the dorsal thalamus	VENT
Ventral anterior-lateral complex of the thalamus	VAL
Ventral medial nucleus of the thalamus	VM
Ventral posterior complex of the thalamus	VP
Ventral posterolateral nucleus of the thalamus	VPL
Ventral posterolateral nucleus of the thalamus, parvicellular part	VPLpc
Ventral posteromedial nucleus of the thalamus	VPM
Ventral posteromedial nucleus of the thalamus, parvicellular part	VPMpc
Subparafascicular nucleus	SPF
Subparafascicular nucleus, magnocellular part	SPFm
Subparafascicular nucleus, parvicellular part	SPFp
Subparafascicular area	SPA
Peripeduncular nucleus	PP
Geniculate group, dorsal thalamus	GENd
Medial geniculate complex	MG
Medial geniculate complex, dorsal part	MGd
Medial geniculate complex, ventral part	MGv
Medial geniculate complex, medial part	MGm
Dorsal part of the lateral geniculate complex	LGd
Thalamus, polymodal association cortex related	DORpm
Lateral group of the dorsal thalamus	LAT
Lateral posterior nucleus of the thalamus	LP
Posterior complex of the thalamus	PO
Posterior limiting nucleus of the thalamus	POL
Suprageniculate nucleus	SGN
Anterior group of the dorsal thalamus	ATN
Anteroventral nucleus of thalamus	AV
Anteromedial nucleus	AM
Anteromedial nucleus, dorsal part	AMd
Anteromedial nucleus, ventral part	AMv
Anterodorsal nucleus	AD
Interanteromedial nucleus of the thalamus	IAM
Interanterodorsal nucleus of the thalamus	IAD

Lateral dorsal nucleus of thalamus	LD
Medial group of the dorsal thalamus	MED
Intermediodorsal nucleus of the thalamus	IMD
Mediodorsal nucleus of thalamus	MD
Mediodorsal nucleus of the thalamus, central part	MDc
Mediodorsal nucleus of the thalamus, lateral part	MDl
Mediodorsal nucleus of the thalamus, medial part	MDm
Submedial nucleus of the thalamus	SMT
Perireunensis nucleus	PR
Midline group of the dorsal thalamus	MTN
Paraventricular nucleus of the thalamus	PVT
Parataenial nucleus	PT
Nucleus of reunions	RE
Intralaminar nuclei of the dorsal thalamus	ILM
Rhomboid nucleus	RH
Central medial nucleus of the thalamus	CM
Paracentral nucleus	PCN
Central lateral nucleus of the thalamus	CL
Parafascicular nucleus	PF
Reticular nucleus of the thalamus	RT
Geniculate group, ventral thalamus	GENv
Intergeniculate leaflet of the lateral geniculate complex	IGL
Ventral part of the lateral geniculate complex	LGv
Ventral part of the lateral geniculate complex, lateral zone	LGvl
Ventral part of the lateral geniculate complex, medial zone	LGvm
Subgeniculate nucleus	SubG
Epithalamus	EPI
Medial habenula	MH
Lateral habenula	LH
Pineal body	PIN
Hypothalamus	HY
Periventricular zone	PVZ
Supraoptic nucleus	SO
Accessory supraoptic group	ASO
Nucleus circularis	NC
Paraventricular hypothalamic nucleus	PVH
Paraventricular hypothalamic nucleus, magnocellular division	PVHm
Paraventricular hypothalamic nucleus, magnocellular division, anterior magnocellular part	PVHam
Paraventricular hypothalamic nucleus, magnocellular division, medial magnocellular part	PVHmm
Paraventricular hypothalamic nucleus, magnocellular division, posterior magnocellular part	PVHpm
Paraventricular hypothalamic nucleus, magnocellular division, posterior magnocellular part, lateral zone	PVHpml
Paraventricular hypothalamic nucleus, magnocellular division, posterior magnocellular part, medial zone	PVHpmm
Paraventricular hypothalamic nucleus, parvicellular division	PVHp
Paraventricular hypothalamic nucleus, parvicellular division, anterior parvicellular part	PVHap

Paraventricular hypothalamic nucleus, parvicellular division, medial parvicellular part, dorsal zone	PVHmpd
Paraventricular hypothalamic nucleus, parvicellular division, periventricular part	PVHpv
Periventricular hypothalamic nucleus, anterior part	PVa
Periventricular hypothalamic nucleus, intermediate part	PVi
Arcuate hypothalamic nucleus	ARH
Periventricular region	PVR
Anterodorsal preoptic nucleus	ADP
Anterior hypothalamic area	AHA
Anteroventral preoptic nucleus	AVP
Anteroventral periventricular nucleus	AVPV
Dorsomedial nucleus of the hypothalamus	DMH
Dorsomedial nucleus of the hypothalamus, anterior part	DMHa
Dorsomedial nucleus of the hypothalamus, posterior part	DMHp
Dorsomedial nucleus of the hypothalamus, ventral part	DMHv
Median preoptic nucleus	MEPO
Medial preoptic area	MPO
Vascular organ of the lamina terminalis	OV
Posterodorsal preoptic nucleus	PD
Parastrial nucleus	PS
Suprachiasmatic preoptic nucleus	PSCH
Periventricular hypothalamic nucleus, posterior part	PVp
Periventricular hypothalamic nucleus, preoptic part	PVpo
Subparaventricular zone	SBPV
Suprachiasmatic nucleus	SCH
Subfornical organ	SFO
Ventrolateral preoptic nucleus	VLPO
Hypothalamic medial zone	MEZ
Anterior hypothalamic nucleus	AHN
Anterior hypothalamic nucleus, anterior part	AHNa
Anterior hypothalamic nucleus, central part	AHNc
Anterior hypothalamic nucleus, dorsal part	AHNd
Anterior hypothalamic nucleus, posterior part	AHNp
Mammillary body	MBO
Lateral mammillary nucleus	LM
Medial mammillary nucleus	MM
Medial mammillary nucleus, median part	Mmme
Supramammillary nucleus	SUM
Supramammillary nucleus, lateral part	SUMl
Supramammillary nucleus, medial part	SUMm
Tuberomammillary nucleus	TM
Tuberomammillary nucleus, dorsal part	TMd
Tuberomammillary nucleus, ventral part	TMv
Medial preoptic nucleus	MPN
Medial preoptic nucleus, central part	MPNc
Medial preoptic nucleus, lateral part	MPNl
Medial preoptic nucleus, medial part	MPNm
Dorsal premammillary nucleus	PMd
Ventral premammillary nucleus	PMv

Paraventricular hypothalamic nucleus, descending division	PVHd
Paraventricular hypothalamic nucleus, descending division, dorsal parvicellular part	PVHdp
Paraventricular hypothalamic nucleus, descending division, forniceal part	PVHf
Paraventricular hypothalamic nucleus, descending division, lateral parvicellular part	PVHlp
Paraventricular hypothalamic nucleus, descending division, medial parvicellular part, ventral zone	PVHmpv
Ventromedial hypothalamic nucleus	VMH
Ventromedial hypothalamic nucleus, anterior part	VMHa
Ventromedial hypothalamic nucleus, central part	VMHc
Ventromedial hypothalamic nucleus, dorsomedial part	VMHdm
Ventromedial hypothalamic nucleus, ventrolateral part	VMHvl
Posterior hypothalamic nucleus	PH
Hypothalamic lateral zone	LZ
Lateral hypothalamic area	LHA
Lateral preoptic area	LPO
Preparasubthalamic nucleus	PST
Parasubthalamic nucleus	PSTN
Retrochiasmatic area	RCH
Subthalamic nucleus	STN
Tuberal nucleus	TU
Zona incerta	ZI
Dopaminergic A13 group	A13
Fields of Forel	FF
Median eminence	ME
Midbrain	MB
Midbrain, sensory related	MBsen
Superior colliculus, sensory related	SCs
Superior colliculus, optic layer	SCop
Superior colliculus, superficial gray layer	SCsg
Superior colliculus, zonal layer	SCzo
Inferior colliculus	IC
Inferior colliculus, central nucleus	ICc
Inferior colliculus, dorsal nucleus	ICd
Inferior colliculus, external nucleus	ICe
Nucleus of the brachium of the inferior colliculus	NB
Nucleus sagulum	SAG
Parabigeminal nucleus	PBG
Midbrain trigeminal nucleus	MEV
Midbrain, motor related	MBmot
Substantia nigra, reticular part	SNr
Ventral tegmental area	VTA
Midbrain reticular nucleus, retrorubral area	RR
Midbrain reticular nucleus	MRN
Midbrain reticular nucleus, magnocellular part	MRNm
Midbrain reticular nucleus, magnocellular part, general	MRNmg
Midbrain reticular nucleus, parvicellular part	MRNp
Superior colliculus, motor related	SCm

Superior colliculus, motor related, deep gray layer	SCdg
Superior colliculus, motor related, deep white layer	SCdw
Superior colliculus, motor related, intermediate white layer	SCiw
Superior colliculus, motor related, intermediate gray layer	SCig
Superior colliculus, motor related, intermediate gray layer, sublayer a	SCig-a
Superior colliculus, motor related, intermediate gray layer, sublayer b	SCig-b
Superior colliculus, motor related, intermediate gray layer, sublayer c	SCig-c
Periaqueductal gray	PAG
Precommissural nucleus	PRC
Interstitial nucleus of Cajal	INC
Nucleus of Darkschewitsch	ND
Pretectal region	PRT
Anterior pretectal nucleus	APN
Medial pretectal area	MPT
Nucleus of the optic tract	NOT
Nucleus of the posterior commissure	NPC
Olivary pretectal nucleus	OP
Posterior pretectal nucleus	PPT
Cuneiform nucleus	CUN
Red nucleus	RN
Oculomotor nucleus	III
Edinger-Westphal nucleus	EW
Trochlear nucleus	IV
Ventral tegmental nucleus	VTN
Anterior tegmental nucleus	AT
Lateral terminal nucleus of the accessory optic tract	LT
Dorsal terminal nucleus of the accessory optic tract	DT
Medial terminal nucleus of the accessory optic tract	MT
Substantia nigra, lateral part	SNl
Midbrain, behavioral state related	MBsta
Substantia nigra, compact part	SNc
Pedunculopontine nucleus	PPN
Midbrain raphÈ nuclei	RAmb
Interfascicular nucleus raphÈ	IF
Interpeduncular nucleus	IPN
Rostral linear nucleus raphÈ	RL
Central linear nucleus raphÈ	CLI
Dorsal nucleus raphÈ	DR
Hindbrain	HB
Pons	P
Pons, sensory related	P-sen
Nucleus of the lateral lemniscus	NLL
Nucleus of the lateral lemniscus, dorsal part	NLLd
Nucleus of the lateral lemniscus, horizontal part	NLLh
Nucleus of the lateral lemniscus, ventral part	NLLv
Principal sensory nucleus of the trigeminal	PSV
Parabrachial nucleus	PB
Kolliker-Fuse subnucleus	KF
Parabrachial nucleus, lateral division	PBl

Parabrachial nucleus, lateral division, central lateral part	PBlc
Parabrachial nucleus, lateral division, dorsal lateral part	PBld
Parabrachial nucleus, lateral division, external lateral part	PBle
Parabrachial nucleus, lateral division, superior lateral part	PBls
Parabrachial nucleus, lateral division, ventral lateral part	PBlv
Parabrachial nucleus, medial division	PBm
Parabrachial nucleus, medial division, external medial part	PBme
Parabrachial nucleus, medial division, medial medial part	PBmm
Parabrachial nucleus, medial division, ventral medial part	PBmv
Superior olivary complex	SOC
Superior olivary complex, periolivary region	POR
Superior olivary complex, medial part	SOCm
Superior olivary complex, lateral part	SOCl
Pons, motor related	P-mot
Barrington's nucleus	B
Dorsal tegmental nucleus	DTN
Lateral tegmental nucleus	LTN
Pontine central gray	PCG
Pontine gray	PG
Pontine reticular nucleus, caudal part	PRNc
Pontine reticular nucleus, ventral part	PRNv
Supragenual nucleus	SG
Superior salivatory nucleus	SSN
Supratrigeminal nucleus	SUT
Tegmental reticular nucleus	TRN
Motor nucleus of trigeminal	V
Pons, behavioral state related	P-sat
Superior central nucleus raphÈ	CS
Superior central nucleus raphÈ, lateral part	CSl
Superior central nucleus raphÈ, medial part	CSm
Locus ceruleus	LC
Laterodorsal tegmental nucleus	LDT
Nucleus incertus	NI
Pontine reticular nucleus	PRNr
Nucleus raphÈ pontis	RPO
Subceruleus nucleus	SLC
Sublaterodorsal nucleus	SLD
Medulla	MY
Medulla, sensory related	MY-sen
Area postrema	AP
Cochlear nuclei	CN
Granular lamina of the cochlear nuclei	CNlam
Cochlear nucleus, subpedunclular granular region	CNspg
Dorsal cochlear nucleus	DCO
Ventral cochlear nucleus	VCO
Dorsal column nuclei	DCN
Cuneate nucleus	CU
Gracile nucleus	GR
External cuneate nucleus	ECU

Nucleus of the trapezoid body	NTB
Nucleus of the solitary tract	NTS
Nucleus of the solitary tract, central part	NTSce
Nucleus of the solitary tract, commissural part	NTSco
Nucleus of the solitary tract, gelatinous part	NTSge
Nucleus of the solitary tract, lateral part	NTSl
Nucleus of the solitary tract, medial part	NTSm
Spinal nucleus of the trigeminal, caudal part	SPVC
Spinal nucleus of the trigeminal, interpolar part	SPVI
Spinal nucleus of the trigeminal, oral part	SPVO
Spinal nucleus of the trigeminal, oral part, caudal dorsomedial part	SPVOcdm
Spinal nucleus of the trigeminal, oral part, middle dorsomedial part, dorsal zone	SPVOmdmd
Spinal nucleus of the trigeminal, oral part, middle dorsomedial part, ventral zone	SPVOmdmv
Spinal nucleus of the trigeminal, oral part, rostral dorsomedial part	SPVOrdm
Spinal nucleus of the trigeminal, oral part, ventrolateral part	SPVOvl
Nucleus z	z
Medulla, motor related	MY-mot
Abducens nucleus	VI
Accessory abducens nucleus	ACVI
Facial motor nucleus	VII
Accessory facial motor nucleus	ACVII
Efferent vestibular nucleus	EV
Nucleus ambiguus	AMB
Nucleus ambiguus, dorsal division	AMBd
Nucleus ambiguus, ventral division	AMBv
Dorsal motor nucleus of the vagus nerve	DMX
Efferent cochlear group	ECO
Gigantocellular reticular nucleus	GRN
Infracerebellar nucleus	ICB
Inferior olivary complex	IO
Intermediate reticular nucleus	IRN
Inferior salivatory nucleus	ISN
Linear nucleus of the medulla	LIN
Lateral reticular nucleus	LRN
Lateral reticular nucleus, magnocellular part	LRNm
Lateral reticular nucleus, parvicellular part	LRNp
Magnocellular reticular nucleus	MARN
Medullary reticular nucleus	MDRN
Medullary reticular nucleus, dorsal part	MDRNd
Medullary reticular nucleus, ventral part	MDRNv
Parvicellular reticular nucleus	PARN
Parasolitary nucleus	PAS
Paragigantocellular reticular nucleus	PGRN
Paragigantocellular reticular nucleus, dorsal part	PGRNd
Paragigantocellular reticular nucleus, lateral part	PGRNl
Perihypoglossal nuclei	PHY
Nucleus intercalatus	NIS
Nucleus of Roller	NR

Nucleus prepositus	PRP
Paramedian reticular nucleus	PMR
Parapyramidal nucleus	PPY
Parapyramidal nucleus, deep part	PPYd
Parapyramidal nucleus, superficial part	PPYs
Vestibular nuclei	VNC
Lateral vestibular nucleus	LAV
Medial vestibular nucleus	MV
Spinal vestibular nucleus	SPIV
Superior vestibular nucleus	SUV
Nucleus x	x
Hypoglossal nucleus	XII
Nucleus y	y
Interstitial nucleus of the vestibular nerve	INV
Medulla, behavioral state related	MY-sat
Nucleus raphÈ magnus	RM
Nucleus raphÈ pallidus	RPA
Nucleus raphÈ obscurus	RO

References

Adalsteinsson, B.T., and Ferguson-Smith, A.C. (2014). Epigenetic control of the genome-lessons from genomic imprinting. Genes (Basel) *5*, 635-655.

Adhikari, A., Lerner, T.N., Finkelstein, J., Pak, S., Jennings, J.H., Davidson, T.J., Ferenczi, E., Gunaydin, L.A., Mirzabekov, J.J., Ye, L.*, et al.* (2015). Basomedial amygdala mediates top-down control of anxiety and fear. Nature *527*, 179-185.

Allen, N.D., Logan, K., Lally, G., Drage, D.J., Norris, M.L., and Keverne, E.B. (1995). Distribution of parthenogenetic cells in the mouse brain and their influence on brain development and behavior. Proc Natl Acad Sci U S A *92*, 10782-10786.

Alvarez-Mora, M.I., Rodriguez-Revenga, L., Feliu, A., Badenas, C., Madrigal, I., and Mila, M. (2016). Skewed X Inactivation in Women Carrying the FMR1 Premutation and Its Relation with Fragile-X-Associated Tremor/Ataxia Syndrome. Neurodegener Dis *16*, 290-292.

Amat, J., Baratta, M.V., Paul, E., Bland, S.T., Watkins, L.R., and Maier, S.F. (2005). Medial prefrontal cortex determines how stressor controllability affects behavior and dorsal raphe nucleus. Nat Neurosci *8*, 365-371.

Amir, R.E., Van den Veyver, I.B., Schultz, R., Malicki, D.M., Tran, C.Q., Dahle, E.J., Philippi, A., Timar, L., Percy, A.K., Motil, K.J.*, et al.* (2000). Influence of mutation type and X chromosome inactivation on Rett syndrome phenotypes. Ann Neurol *47*, 670-679.

Arsenault, J., Gholizadeh, S., Niibori, Y., Pacey, L.K., Halder, S.K., Koxhioni, E., Konno, A., Hirai, H., and Hampson, D.R. (2016). FMRP Expression Levels in Mouse Central Nervous System Neurons Determine Behavioral Phenotype. Hum Gene Ther *27*, 982-996.

Bacher, C.P., Guggiari, M., Brors, B., Augui, S., Clerc, P., Avner, P., Eils, R., and Heard, E. (2006). Transient colocalization of X-inactivation centres accompanies the initiation of X inactivation. Nat Cell Biol *8*, 293-299.

Baker, K.B., Wray, S.P., Ritter, R., Mason, S., Lanthorn, T.H., and Savelieva, K.V. (2010). Male and female Fmr1 knockout mice on C57 albino background exhibit spatial learning and memory impairments. Genes Brain Behav *9*, 562-574.

Bakker, C.E., Verheij, C., Willemsen, R., van der Helm, R., Oerlemans, F., Vermey, M., Bygrave, A., Hoogeveen, A.T., and Oostra, B.A. (1994). Fmr1 knockout mice: a model to study fragile X mental retardation. The Dutch-Belgian Fragile X Consortium. Cell *78*, 23-33.

Barr, M.L., and Bertram, E.G. (1949). A morphological distinction between neurones of the male and female, and the behaviour of the nucleolar satellite during accelerated nucleoprotein synthesis. Nature *163*, 676.

Bartolomei, M.S., and Ferguson-Smith, A.C. (2011). Mammalian genomic imprinting. Cold Spring Harb Perspect Biol *3*.

Bayless, D.W., and Shah, N.M. (2016). Genetic dissection of neural circuits underlying sexually dimorphic social behaviours. Philos Trans R Soc Lond B Biol Sci *371*, 20150109.

Belzung, C., and Griebel, G. (2001). Measuring normal and pathological anxiety-like behaviour in mice: a review. Behav Brain Res *125*, 141-149.

Bennetto, L., Pennington, B.F., Porter, D., Taylor, A.K., and Hagerman, R.J. (2001). Profile of cognitive functioning in women with the fragile X mutation. Neuropsychology *15*, 290-299.

Bittel, D.C., Theodoro, M.F., Kibiryeva, N., Fischer, W., Talebizadeh, Z., and Butler, M.G. (2008). Comparison of X-chromosome inactivation patterns in multiple tissues from human females. J Med Genet *45*, 309-313.

Bland, B.H., and Oddie, S.D. (2001). Theta band oscillation and synchrony in the hippocampal formation and associated structures: the case for its role in sensorimotor integration. Behav Brain Res *127*, 119-136.

Bokor, H., Frere, S.G., Eyre, M.D., Slezia, A., Ulbert, I., Luthi, A., and Acsady, L. (2005). Selective GABAergic control of higher-order thalamic relays. Neuron *45*, 929-940.

Brandao, M.L., Rees, H., Witt, S., and Roberts, M.H. (1991). Central antiaversive and antinociceptive effects of anterior pretectal nucleus stimulation: attenuation of autonomic and aversive effects of medial hypothalamic stimulation. Brain Res *542*, 266-272.

Brown, C.J., Ballabio, A., Rupert, J.L., Lafreniere, R.G., Grompe, M., Tonlorenzi, R., and Willard, H.F. (1991a). A gene from the region of the human X inactivation centre is expressed exclusively from the inactive X chromosome. Nature *349*, 38-44.

Brown, C.J., Lafreniere, R.G., Powers, V.E., Sebastio, G., Ballabio, A., Pettigrew, A.L., Ledbetter, D.H., Levy, E., Craig, I.W., and Willard, H.F. (1991b).

Localization of the X inactivation centre on the human X chromosome in Xq13. Nature *349*, 82-84.

Brown, K., Selfridge, J., Lagger, S., Connelly, J., De Sousa, D., Kerr, A., Webb, S., Guy, J., Merusi, C., Koerner, M.V.*, et al.* (2016). The molecular basis of variable phenotypic severity among common missense mutations causing Rett syndrome. Hum Mol Genet *25*, 558-570.

Butler, M.G. (2002). Imprinting disorders: non-Mendelian mechanisms affecting growth. J Pediatr Endocrinol Metab *15 Suppl 5*, 1279-1288.

Butt, S.J., Fuccillo, M., Nery, S., Noctor, S., Kriegstein, A., Corbin, J.G., and Fishell, G. (2005). The temporal and spatial origins of cortical interneurons predict their physiological subtype. Neuron *48*, 591-604.

Buzsaki, G. (2002). Theta oscillations in the hippocampus. Neuron *33*, 325-340.

Cassidy, S.B., Dykens, E., and Williams, C.A. (2000). Prader-Willi and Angelman syndromes: sister imprinted disorders. Am J Med Genet *97*, 136-146.

Cetin, A., Komai, S., Eliava, M., Seeburg, P.H., and Osten, P. (2006). Stereotaxic gene delivery in the rodent brain. Nat Protoc *1*, 3166-3173.

Charalambous, M., Cowley, M., Geoghegan, F., Smith, F.M., Radford, E.J., Marlow, B.P., Graham, C.F., Hurst, L.D., and Ward, A. (2010). Maternally-inherited Grb10 reduces placental size and efficiency. Dev Biol *337*, 1-8.

Chaste, P., Betancur, C., Gerard-Blanluet, M., Bargiacchi, A., Kuzbari, S., Drunat, S., Leboyer, M., Bourgeron, T., and Delorme, R. (2012). High-functioning autism spectrum disorder and fragile X syndrome: report of two affected sisters. Mol Autism *3*, 5.

Chen, E., Sharma, M.R., Shi, X., Agrawal, R.K., and Joseph, S. (2014). Fragile X mental retardation protein regulates translation by binding directly to the ribosome. Mol Cell *54*, 407-417.

Christianson, A.L., Stevenson, R.E., van der Meyden, C.H., Pelser, J., Theron, F.W., van Rensburg, P.L., Chandler, M., and Schwartz, C.E. (1999). X linked severe mental retardation, craniofacial dysmorphology, epilepsy, ophthalmoplegia, and cerebellar atrophy in a large South African kindred is localised to Xq24-q27. J Med Genet *36*, 759-766.

Clifford, S., Dissanayake, C., Bui, Q.M., Huggins, R., Taylor, A.K., and Loesch, D.Z. (2007). Autism spectrum phenotype in males and females with fragile X full mutation and premutation. J Autism Dev Disord *37*, 738-747.

Cordeiro, L., Ballinger, E., Hagerman, R., and Hessl, D. (2011). Clinical assessment of DSM-IV anxiety disorders in fragile X syndrome: prevalence and characterization. J Neurodev Disord *3*, 57-67.

Crespi, B. (2008). Genomic imprinting in the development and evolution of psychotic spectrum conditions. Biol Rev Camb Philos Soc *83*, 441-493.

Curley, J.P. (2011). Is there a genomically imprinted social brain? Bioessays *33*, 662-668.

Davies, W. (2010). Genomic imprinting on the X chromosome: implications for brain and behavioral phenotypes. Ann N Y Acad Sci *1204 Suppl*, E14-19.

Davis, T.L., Trasler, J.M., Moss, S.B., Yang, G.J., and Bartolomei, M.S. (1999). Acquisition of the H19 methylation imprint occurs differentially on the parental alleles during spermatogenesis. Genomics *58*, 18-28.

de Vries, B.B., Wiegers, A.M., Smits, A.P., Mohkamsing, S., Duivenvoorden, H.J., Fryns, J.P., Curfs, L.M., Halley, D.J., Oostra, B.A., van den Ouweland, A.M.*, et al.* (1996). Mental status of females with an FMR1 gene full mutation. Am J Hum Genet *58*, 1025-1032.

Deacon, R.M., and Rawlins, J.N. (2006). T-maze alternation in the rodent. Nat Protoc *1*, 7-12.

Echevarria, L., Benistan, K., Toussaint, A., Dubourg, O., Hagege, A.A., Eladari, D., Jabbour, F., Beldjord, C., De Mazancourt, P., and Germain, D.P. (2016). X-chromosome inactivation in female patients with Fabry disease. Clin Genet *89*, 44-54.

Engreitz, J.M., Pandya-Jones, A., McDonel, P., Shishkin, A., Sirokman, K., Surka, C., Kadri, S., Xing, J., Goren, A., Lander, E.S.*, et al.* (2013). The Xist lncRNA exploits three-dimensional genome architecture to spread across the X chromosome. Science *341*, 1237973.

Fanselow, M.S., and Dong, H.W. (2010). Are the dorsal and ventral hippocampus functionally distinct structures? Neuron *65*, 7-19.

Ferron, L., Nieto-Rostro, M., Cassidy, J.S., and Dolphin, A.C. (2014). Fragile X mental retardation protein controls synaptic vesicle exocytosis by modulating N-type calcium channel density. Nat Commun *5*, 3628.

Fieremans, N., Van Esch, H., Holvoet, M., Van Goethem, G., Devriendt, K., Rosello, M., Mayo, S., Martinez, F., Jhangiani, S., Muzny, D.M.*, et al.* (2016). Identification of Intellectual Disability Genes in Female Patients with a Skewed X-Inactivation Pattern. Hum Mutat *37*, 804-811.

Frankland, P.W., Wang, Y., Rosner, B., Shimizu, T., Balleine, B.W., Dykens, E.M., Ornitz, E.M., and Silva, A.J. (2004). Sensorimotor gating abnormalities in young males with fragile X syndrome and Fmr1-knockout mice. Mol Psychiatry *9*, 417-425.

Freeman, M.E., Kanyicska, B., Lerant, A., and Nagy, G. (2000). Prolactin: structure, function, and regulation of secretion. Physiol Rev *80*, 1523-1631.

Freund, L.S., Reiss, A.L., and Abrams, M.T. (1993). Psychiatric disorders associated with fragile X in the young female. Pediatrics *91*, 321-329.

Fyhn, M., Molden, S., Witter, M.P., Moser, E.I., and Moser, M.B. (2004). Spatial representation in the entorhinal cortex. Science *305*, 1258-1264.

Gale, R.E., Mein, C.A., and Linch, D.C. (1996). Quantification of X-chromosome inactivation patterns in haematological samples using the DNA PCR-based HUMARA assay. Leukemia *10*, 362-367.

Gao, Q., and Horvath, T.L. (2008). Neuronal control of energy homeostasis. FEBS Lett *582*, 132-141.

Garcia-Palmero, I., Pompas-Veganzones, N., Villalobo, E., Gioria, S., Haiech, J., and Villalobo, A. (2017). The adaptors Grb10 and Grb14 are calmodulin-binding proteins. FEBS Lett.

Garfield, A.S., Cowley, M., Smith, F.M., Moorwood, K., Stewart-Cox, J.E., Gilroy, K., Baker, S., Xia, J., Dalley, J.W., Hurst, L.D.*, et al.* (2011). Distinct physiological and behavioural functions for parental alleles of imprinted Grb10. Nature *469*, 534-538.

Gaszner, B., Kormos, V., Kozicz, T., Hashimoto, H., Reglodi, D., and Helyes, Z. (2012). The behavioral phenotype of pituitary adenylate-cyclase activating polypeptide-deficient mice in anxiety and depression tests is accompanied by blunted c-Fos expression in the bed nucleus of the stria terminalis, central projecting Edinger-Westphal nucleus, ventral lateral septum, and dorsal raphe nucleus. Neuroscience *202*, 283-299.

Gholizadeh, S., Arsenault, J., Xuan, I.C., Pacey, L.K., and Hampson, D.R. (2014). Reduced phenotypic severity following adeno-associated virus-mediated Fmr1 gene delivery in fragile X mice. Neuropsychopharmacology *39*, 3100-3111.

Gibson, J.H., Williamson, S.L., Arbuckle, S., and Christodoulou, J. (2005). X chromosome inactivation patterns in brain in Rett syndrome: implications for the disease phenotype. Brain Dev *27*, 266-270.

Gontan, C., Achame, E.M., Demmers, J., Barakat, T.S., Rentmeester, E., van, I.W., Grootegoed, J.A., and Gribnau, J. (2012). RNF12 initiates X-chromosome inactivation by targeting REX1 for degradation. Nature *485*, 386-390.

Gould, T.J., Keith, R.A., and Bhat, R.V. (2001). Differential sensitivity to lithium's reversal of amphetamine-induced open-field activity in two inbred strains of mice. Behav Brain Res *118*, 95-105.

Gregg, C., Zhang, J., Butler, J.E., Haig, D., and Dulac, C. (2010). Sex-specific parent-of-origin allelic expression in the mouse brain. Science *329*, 682-685.

Hadjantonakis, A.K., Cox, L.L., Tam, P.P., and Nagy, A. (2001). An X-linked GFP transgene reveals unexpected paternal X-chromosome activity in trophoblastic giant cells of the mouse placenta. Genesis *29*, 133-140.

Hagerman, R.J., Hills, J., Scharfenaker, S., and Lewis, H. (1999). Fragile X syndrome and selective mutism. Am J Med Genet *83*, 313-317.

Hajkova, P. (2011). Epigenetic reprogramming in the germline: towards the ground state of the epigenome. Philos Trans R Soc Lond B Biol Sci *366*, 2266-2273.

Hayashi, K., Ohta, H., Kurimoto, K., Aramaki, S., and Saitou, M. (2011). Reconstitution of the mouse germ cell specification pathway in culture by pluripotent stem cells. Cell *146*, 519-532.

Heine-Suner, D., Torres-Juan, L., Morla, M., Busquets, X., Barcelo, F., Pico, G., Bonilla, L., Govea, N., Bernues, M., and Rosell, J. (2003). Fragile-X syndrome and skewed X-chromosome inactivation within a family: a female member with complete inactivation of the functional X chromosome. Am J Med Genet A *122A*, 108-114.

Hirata, T., Suda, Y., Nakao, K., Narimatsu, M., Hirano, T., and Hibi, M. (2004). Zinc finger gene fez-like functions in the formation of subplate neurons and thalamocortical axons. Dev Dyn *230*, 546-556.

Hoerder-Suabedissen, A., and Molnar, Z. (2015). Development, evolution and pathology of neocortical subplate neurons. Nat Rev Neurosci *16*, 133-146.

Huynh, K.D., and Lee, J.T. (2003). Inheritance of a pre-inactivated paternal X chromosome in early mouse embryos. Nature *426*, 857-862.

Isles, A.R., Davies, W., and Wilkinson, L.S. (2006). Genomic imprinting and the social brain. Philos Trans R Soc Lond B Biol Sci *361*, 2229-2237.

Jelinic, P., and Shaw, P. (2007). Loss of imprinting and cancer. J Pathol *211*, 261-268.

Jiang, Y.H., Armstrong, D., Albrecht, U., Atkins, C.M., Noebels, J.L., Eichele, G., Sweatt, J.D., and Beaudet, A.L. (1998). Mutation of the Angelman ubiquitin ligase in mice causes increased cytoplasmic p53 and deficits of contextual learning and long-term potentiation. Neuron *21*, 799-811.

Johansen, J.P., Tarpley, J.W., LeDoux, J.E., and Blair, H.T. (2010). Neural substrates for expectation-modulated fear learning in the amygdala and periaqueductal gray. Nat Neurosci *13*, 979-986.

Kazdoba, T.M., Leach, P.T., Silverman, J.L., and Crawley, J.N. (2014). Modeling fragile X syndrome in the Fmr1 knockout mouse. Intractable Rare Dis Res *3*, 118-133.

Kernohan, K.D., and Berube, N.G. (2010). Genetic and epigenetic dysregulation of imprinted genes in the brain. Epigenomics *2*, 743-763.

Keverne, E.B., Fundele, R., Narasimha, M., Barton, S.C., and Surani, M.A. (1996). Genomic imprinting and the differential roles of parental genomes in brain development. Brain research Developmental brain research *92*, 91-100.

Kielinen, M., Rantala, H., Timonen, E., Linna, S.L., and Moilanen, I. (2004). Associated medical disorders and disabilities in children with autistic disorder: a population-based study. Autism *8*, 49-60.

Kim, J.H., Lee, S.R., Li, L.H., Park, H.J., Park, J.H., Lee, K.Y., Kim, M.K., Shin, B.A., and Choi, S.Y. (2011). High cleavage efficiency of a 2A peptide derived from porcine teschovirus-1 in human cell lines, zebrafish and mice. PLoS One *6*, e18556.

Kim, Y., Venkataraju, K.U., Pradhan, K., Mende, C., Taranda, J., Turaga, S.C., Arganda-Carreras, I., Ng, L., Hawrylycz, M.J., Rockland, K.S*., et al.* (2015). Mapping social behavior-induced brain activation at cellular resolution in the mouse. Cell Rep *10*, 292-305.

Klein, S., Staring, M., Murphy, K., Viergever, M.A., and Pluim, J.P. (2010). elastix: a toolbox for intensity-based medical image registration. IEEE Trans Med Imaging *29*, 196-205.

Kojima, Y., Tam, O.H., and Tam, P.P. (2014). Timing of developmental events in the early mouse embryo. Semin Cell Dev Biol *34*, 65-75.

Koutsikou, S., Crook, J.J., Earl, E.V., Leith, J.L., Watson, T.C., Lumb, B.M., and Apps, R. (2014). Neural substrates underlying fear-evoked freezing: the periaqueductal grey-cerebellar link. J Physiol *592*, 2197-2213.

Kuwajima, T., Nishimura, I., and Yoshikawa, K. (2006). Necdin promotes GABAergic neuron differentiation in cooperation with Dlx homeodomain proteins. J Neurosci *26*, 5383-5392.

Larsen, C.M., and Grattan, D.R. (2012). Prolactin, neurogenesis, and maternal behaviors. Brain Behav Immun *26*, 201-209.

LeDoux, J.E., Iwata, J., Cicchetti, P., and Reis, D.J. (1988). Different projections of the central amygdaloid nucleus mediate autonomic and behavioral correlates of conditioned fear. J Neurosci *8*, 2517-2529.

Lee, H.Y., Ge, W.P., Huang, W., He, Y., Wang, G.X., Rowson-Baldwin, A., Smith, S.J., Jan, Y.N., and Jan, L.Y. (2011). Bidirectional regulation of dendritic voltage-gated potassium channels by the fragile X mental retardation protein. Neuron *72*, 630-642.

Lee, J.T., and Bartolomei, M.S. (2013). X-inactivation, imprinting, and long noncoding RNAs in health and disease. Cell *152*, 1308-1323.

Lepage, J.F., Hong, D.S., Mazaika, P.K., Raman, M., Sheau, K., Marzelli, M.J., Hallmayer, J., and Reiss, A.L. (2013). Genomic imprinting effects of the X chromosome on brain morphology. J Neurosci *33*, 8567-8574.

Li, L., Keverne, E.B., Aparicio, S.A., Ishino, F., Barton, S.C., and Surani, M.A. (1999). Regulation of maternal behavior and offspring growth by paternally expressed Peg3. Science *284*, 330-333.

Lim, M.A., Riedel, H., and Liu, F. (2004). Grb10: more than a simple adaptor protein. Front Biosci *9*, 387-403.

Linhoff, M.W., Garg, S.K., and Mandel, G. (2015). A high-resolution imaging approach to investigate chromatin architecture in complex tissues. Cell *163*, 246-255.

Liu, M., Bai, J., He, S., Villarreal, R., Hu, D., Zhang, C., Yang, X., Liang, H., Slaga, T.J., Yu, Y.*, et al.* (2014). Grb10 promotes lipolysis and thermogenesis by phosphorylation-dependent feedback inhibition of mTORC1. Cell Metab *19*, 967-980.

Loesch, D.Z., and Hay, D.A. (1988). Clinical features and reproductive patterns in fragile X female heterozygotes. J Med Genet *25*, 407-414.

Loesch, D.Z., Hay, D.A., Sutherland, G.R., Halliday, J., Judge, C., and Webb, G.C. (1987). Phenotypic variation in male-transmitted fragile X: genetic inferences. Am J Med Genet *27*, 401-417.

Lossi, A.M., Millan, J.M., Villard, L., Orellana, C., Cardoso, C., Prieto, F., Fontes, M., and Martinez, F. (1999). Mutation of the XNP/ATR-X gene in a family with severe mental retardation, spastic paraplegia and skewed pattern of X inactivation: demonstration that the mutation is involved in the inactivation bias. Am J Hum Genet *65*, 558-562.

Lyon, M.F. (1961). Gene action in the X-chromosome of the mouse (Mus musculus L.). Nature *190*, 372-373.

Lyons, J.I., Kerr, G.R., and Mueller, P.W. (2015). Fragile X Syndrome: Scientific Background and Screening Technologies. J Mol Diagn *17*, 463-471.

Lyst, M.J., Ekiert, R., Ebert, D.H., Merusi, C., Nowak, J., Selfridge, J., Guy, J., Kastan, N.R., Robinson, N.D., de Lima Alves, F.*, et al.* (2013). Rett syndrome mutations abolish the interaction of MeCP2 with the NCoR/SMRT co-repressor. Nat Neurosci *16*, 898-902.

M., C.n., G., K., and W., R. (2004). Resourceful Imprinting. Nature *432*, 53-57.

Maier, S.F., Amat, J., Baratta, M.V., Paul, E., and Watkins, L.R. (2006). Behavioral control, the medial prefrontal cortex, and resilience. Dialogues Clin Neurosci *8*, 397-406.

Marahrens, Y., Panning, B., Dausman, J., Strauss, W., and Jaenisch, R. (1997). Xist-deficient mice are defective in dosage compensation but not spermatogenesis. Genes Dev *11*, 156-166.

Marco, E.J., and Skuse, D.H. (2006). Autism-lessons from the X chromosome. Soc Cogn Affect Neurosci *1*, 183-193.

Markram, H., Toledo-Rodriguez, M., Wang, Y., Gupta, A., Silberberg, G., and Wu, C. (2004). Interneurons of the neocortical inhibitory system. Nat Rev Neurosci *5*, 793-807.

Marner, L., Nyengaard, J.R., Tang, Y., and Pakkenberg, B. (2003). Marked loss of myelinated nerve fibers in the human brain with age. J Comp Neurol *462*, 144-152.

Mattes, D., Haynor, D.R., Vesselle, H., Lewellen, T.K., and Eubank, W. (2003). PET-CT image registration in the chest using free-form deformations. IEEE Trans Med Imaging *22*, 120-128.

McDannald, M.A. (2010). Contributions of the amygdala central nucleus and ventrolateral periaqueductal grey to freezing and instrumental suppression in Pavlovian fear conditioning. Behav Brain Res *211*, 111-117.

McHenry, J.A., Otis, J.M., Rossi, M.A., Robinson, J.E., Kosyk, O., Miller, N.W., McElligott, Z.A., Budygin, E.A., Rubinow, D.R., and Stuber, G.D. (2017). Hormonal gain control of a medial preoptic area social reward circuit. Nat Neurosci *20*, 449-458.

McLeod, F., Ganley, R., Williams, L., Selfridge, J., Bird, A., and Cobb, S.R. (2013). Reduced seizure threshold and altered network oscillatory properties in a mouse model of Rett syndrome. Neuroscience *231*, 195-205.

McMahon, A., Fosten, M., and Monk, M. (1983). X-chromosome inactivation mosaicism in the three germ layers and the germ line of the mouse embryo. J Embryol Exp Morphol *74*, 207-220.

McMahon, A., and Monk, M. (1983). X-chromosome activity in female mouse embryos heterozygous for Pgk-1 and Searle's translocation, T(X; 16) 16H. Genet Res *41*, 69-83.

McNally, G.P., Johansen, J.P., and Blair, H.T. (2011). Placing prediction into the fear circuit. Trends Neurosci *34*, 283-292.

Miller, N.L., Wevrick, R., and Mellon, P.L. (2009). Necdin, a Prader-Willi syndrome candidate gene, regulates gonadotropin-releasing hormone neurons during development. Hum Mol Genet *18*, 248-260.

Motta, S.C., Guimaraes, C.C., Furigo, I.C., Sukikara, M.H., Baldo, M.V., Lonstein, J.S., and Canteras, N.S. (2013). Ventral premammillary nucleus as a critical sensory relay to the maternal aggression network. Proc Natl Acad Sci U S A *110*, 14438-14443.

Namekawa, S.H., Park, P.J., Zhang, L.F., Shima, J.E., McCarrey, J.R., Griswold, M.D., and Lee, J.T. (2006). Postmeiotic sex chromatin in the male germline of mice. Curr Biol *16*, 660-667.

Namekawa, S.H., Payer, B., Huynh, K.D., Jaenisch, R., and Lee, J.T. (2010). Two-step imprinted X inactivation: repeat versus genic silencing in the mouse. Mol Cell Biol *30*, 3187-3205.

Nelson, R.J., and Trainor, B.C. (2007). Neural mechanisms of aggression. Nat Rev Neurosci *8*, 536-546.

Neske, G.T., Patrick, S.L., and Connors, B.W. (2015). Contributions of diverse excitatory and inhibitory neurons to recurrent network activity in cerebral cortex. J Neurosci *35*, 1089-1105.

Nguyen, D.K., and Disteche, C.M. (2006). High expression of the mammalian X chromosome in brain. Brain Res *1126*, 46-49.

Nielsen, D.M., Derber, W.J., McClellan, D.A., and Crnic, L.S. (2002). Alterations in the auditory startle response in Fmr1 targeted mutant mouse models of fragile X syndrome. Brain Res *927*, 8-17.

Nolin, S.L., Lewis, F.A., 3rd, Ye, L.L., Houck, G.E., Jr., Glicksman, A.E., Limprasert, P., Li, S.Y., Zhong, N., Ashley, A.E., Feingold, E.*, et al.* (1996). Familial transmission of the FMR1 CGG repeat. Am J Hum Genet *59*, 1252-1261.

Okamoto, H., and Aizawa, H. (2013). Fear and anxiety regulation by conserved affective circuits. Neuron *78*, 411-413.

Okamoto, I., Otte, A.P., Allis, C.D., Reinberg, D., and Heard, E. (2004). Epigenetic dynamics of imprinted X inactivation during early mouse development. Science *303*, 644-649.

Penzo, M.A., Robert, V., Tucciarone, J., De Bundel, D., Wang, M., Van Aelst, L., Darvas, M., Parada, L.F., Palmiter, R.D., He, M.*, et al.* (2015). The paraventricular thalamus controls a central amygdala fear circuit. Nature *519*, 455-459.

Pereira, A.G., and Moita, M.A. (2016). Is there anybody out there? Neural circuits of threat detection in vertebrates. Curr Opin Neurobiol *41*, 179-187.

Peron, S.P., Freeman, J., Iyer, V., Guo, C., and Svoboda, K. (2015). A Cellular Resolution Map of Barrel Cortex Activity during Tactile Behavior. Neuron *86*, 783-799.

Plagge, A., Gordon, E., Dean, W., Boiani, R., Cinti, S., Peters, J., and Kelsey, G. (2004). The imprinted signaling protein XL alpha s is required for postnatal adaptation to feeding. Nat Genet *36*, 818-826.

Plagge, A., Isles, A.R., Gordon, E., Humby, T., Dean, W., Gritsch, S., Fischer-Colbrie, R., Wilkinson, L.S., and Kelsey, G. (2005). Imprinted Nesp55 influences behavioral reactivity to novel environments. Molecular and cellular biology *25*, 3019-3026.

Plasschaert, R.N., and Bartolomei, M.S. (2015). Tissue-specific regulation and function of Grb10 during growth and neuronal commitment. Proc Natl Acad Sci U S A *112*, 6841-6847.

Plenge, R.M., Stevenson, R.A., Lubs, H.A., Schwartz, C.E., and Willard, H.F. (2002). Skewed X-chromosome inactivation is a common feature of X-linked mental retardation disorders. Am J Hum Genet *71*, 168-173.

Pollex, T., and Heard, E. (2012). Recent advances in X-chromosome inactivation research. Curr Opin Cell Biol *24*, 825-832.

Poulin, J.F., Zou, J., Drouin-Ouellet, J., Kim, K.Y., Cicchetti, F., and Awatramani, R.B. (2014). Defining midbrain dopaminergic neuron diversity by single-cell gene expression profiling. Cell Rep *9*, 930-943.

Quirk, G.J., Likhtik, E., Pelletier, J.G., and Pare, D. (2003). Stimulation of medial prefrontal cortex decreases the responsiveness of central amygdala output neurons. J Neurosci *23*, 8800-8807.

Raefski, A.S., and O'Neill, M.J. (2005). Identification of a cluster of X-linked imprinted genes in mice. Nat Genet *37*, 620-624.

Ragan, T., Kadiri, L.R., Venkataraju, K.U., Bahlmann, K., Sutin, J., Taranda, J., Arganda-Carreras, I., Kim, Y., Seung, H.S., and Osten, P. (2012). Serial two-photon tomography for automated ex vivo mouse brain imaging. Nat Methods *9*, 255-258.

Raymond, F.L. (2006). X linked mental retardation: a clinical guide. J Med Genet *43*, 193-200.

Reik, W., and Walter, J. (2001). Genomic imprinting: parental influence on the genome. Nat Rev Genet *2*, 21-32.

Rinehart, N.J., Cornish, K.M., and Tonge, B.J. (2011). Gender differences in neurodevelopmental disorders: autism and fragile x syndrome. Curr Top Behav Neurosci *8*, 209-229.

Roberts, W.W., and Nagel, J. (1996). First-order projections activated by stimulation of hypothalamic sites eliciting attack and flight in rats. Behav Neurosci *110*, 509-527.

Rougeulle, C., Glatt, H., and Lalande, M. (1997). The Angelman syndrome candidate gene, UBE3A/E6-AP, is imprinted in brain. Nat Genet *17*, 14-15.

Sahara, S., Yanagawa, Y., O'Leary, D.D., and Stevens, C.F. (2012). The fraction of cortical GABAergic neurons is constant from near the start of cortical neurogenesis to adulthood. J Neurosci *32*, 4755-4761.

Sanz, L.A., Chamberlain, S., Sabourin, J.C., Henckel, A., Magnuson, T., Hugnot, J.P., Feil, R., and Arnaud, P. (2008). A mono-allelic bivalent chromatin domain controls tissue-specific imprinting at Grb10. EMBO J *27*, 2523-2532.

Schenberg, L.C., Povoa, R.M., Costa, A.L., Caldellas, A.V., Tufik, S., and Bittencourt, A.S. (2005). Functional specializations within the tectum defense systems of the rat. Neurosci Biobehav Rev *29*, 1279-1298.

Schmid, R.S., Tsujimoto, N., Qu, Q., Lei, H., Li, E., Chen, T., and Blaustein, C.S. (2008). A methyl-CpG-binding protein 2-enhanced green fluorescent protein reporter mouse model provides a new tool for studying the neuronal basis of Rett syndrome. Neuroreport *19*, 393-398.

Schulz, E.G., and Heard, E. (2013). Role and control of X chromosome dosage in mammalian development. Curr Opin Genet Dev *23*, 109-115.

Shimshek, D.R., Kim, J., Hubner, M.R., Spergel, D.J., Buchholz, F., Casanova, E., Stewart, A.F., Seeburg, P.H., and Sprengel, R. (2002). Codon-improved Cre recombinase (iCre) expression in the mouse. Genesis *32*, 19-26.

Shiura, H., Nakamura, K., Hikichi, T., Hino, T., Oda, K., Suzuki-Migishima, R., Kohda, T., Kaneko-ishino, T., and Ishino, F. (2009). Paternal deletion of Meg1/Grb10 DMR causes maternalization of the Meg1/Grb10 cluster in mouse proximal Chromosome 11 leading to severe pre- and postnatal growth retardation. Hum Mol Genet *18*, 1424-1438.

Simon, P., Dupuis, R., and Costentin, J. (1994). Thigmotaxis as an index of anxiety in mice. Influence of dopaminergic transmissions. Behav Brain Res *61*, 59-64.

Skuse, D.H. (2005). X-linked genes and mental functioning. Hum Mol Genet *14 Spec No 1*, R27-32.

Spencer, C.M., Alekseyenko, O., Serysheva, E., Yuva-Paylor, L.A., and Paylor, R. (2005). Altered anxiety-related and social behaviors in the Fmr1 knockout mouse model of fragile X syndrome. Genes Brain Behav *4*, 420-430.

Spowart-Manning, L., and van der Staay, F.J. (2004). The T-maze continuous alternation task for assessing the effects of putative cognition enhancers in the mouse. Behav Brain Res *151*, 37-46.

Stembalska, A., Laczmanska, I., Gil, J., and Pesz, K.A. (2016). Fragile X syndrome in females - a familial case report and review of the literature. Dev Period Med *20*, 99-104.

Summers, J.A., and Feldman, M.A. (1999). Distinctive pattern of behavioral functioning in Angelman syndrome. Am J Ment Retard *104*, 376-384.

Super, H., Soriano, E., and Uylings, H.B. (1998). The functions of the preplate in development and evolution of the neocortex and hippocampus. Brain Res Brain Res Rev *27*, 40-64.

Sved, A.F., Cano, G., Passerin, A.M., and Rabin, B.S. (2002). The locus coeruleus, Barrington's nucleus, and neural circuits of stress. Physiol Behav *77*, 737-742.

Szymczak-Workman, A.L., Vignali, K.M., and Vignali, D.A. (2012). Design and construction of 2A peptide-linked multicistronic vectors. Cold Spring Harb Protoc *2012*, 199-204.

Tada, T., Obata, Y., Tada, M., Goto, Y., Nakatsuji, N., Tan, S., Kono, T., and Takagi, N. (2000). Imprint switching for non-random X-chromosome inactivation during mouse oocyte growth. Development *127*, 3101-3105.

Tan, S.S., Williams, E.A., and Tam, P.P. (1993). X-chromosome inactivation occurs at different times in different tissues of the post-implantation mouse embryo. Nat Genet *3*, 170-174.

Tang, W., Ehrlich, I., Wolff, S.B., Michalski, A.M., Wolfl, S., Hasan, M.T., Luthi, A., and Sprengel, R. (2009). Faithful expression of multiple proteins via 2A-peptide self-processing: a versatile and reliable method for manipulating brain circuits. J Neurosci *29*, 8621-8629.

Tang, Y., Nyengaard, J.R., Pakkenberg, B., and Gundersen, H.J. (1997). Age-induced white matter changes in the human brain: a stereological investigation. Neurobiol Aging *18*, 609-615.

Taniguchi, H., He, M., Wu, P., Kim, S., Paik, R., Sugino, K., Kvitsiani, D., Fu, Y., Lu, J., Lin, Y.*, et al.* (2011). A resource of Cre driver lines for genetic targeting of GABAergic neurons in cerebral cortex. Neuron *71*, 995-1013.

Tian, D., Sun, S., and Lee, J.T. (2010). The long noncoding RNA, Jpx, is a molecular switch for X chromosome inactivation. Cell *143*, 390-403.

Tovote, P., Esposito, M.S., Botta, P., Chaudun, F., Fadok, J.P., Markovic, M., Wolff, S.B., Ramakrishnan, C., Fenno, L., Deisseroth, K.*, et al.* (2016). Midbrain circuits for defensive behaviour. Nature *534*, 206-212.

Tovote, P., Fadok, J.P., and Luthi, A. (2015). Neuronal circuits for fear and anxiety. Nat Rev Neurosci *16*, 317-331.

Turaga, S.C., Murray, J.F., Jain, V., Roth, F., Helmstaedter, M., Briggman, K., Denk, W., and Seung, H.S. (2010). Convolutional networks can learn to generate affinity graphs for image segmentation. Neural Comput *22*, 511-538.

Ubeda, F., and Gardner, A. (2011). A model for genomic imprinting in the social brain: adults. Evolution *65*, 462-475.

Van der Werf, Y.D., Witter, M.P., and Groenewegen, H.J. (2002). The intralaminar and midline nuclei of the thalamus. Anatomical and functional evidence for participation in processes of arousal and awareness. Brain Res Brain Res Rev *39*, 107-140.

Vazna, A., Musova, Z., Vlckova, M., Novotna, D., Dvorakova, L., Hrdlicka, M., Havlovicova, M., and Sedlacek, Z. (2010). FMR1 gene expansion, large deletion of Xp, and skewed X-inactivation in a girl with mental retardation and autism. Am J Med Genet A *152A*, 1273-1277.

Vianna, D.M., and Brandao, M.L. (2003). Anatomical connections of the periaqueductal gray: specific neural substrates for different kinds of fear. Braz J Med Biol Res *36*, 557-566.

Visootsak, J., Warren, S.T., Anido, A., and Graham, J.M., Jr. (2005). Fragile X syndrome: an update and review for the primary pediatrician. Clin Pediatr (Phila) *44*, 371-381.

Wang, L., Balas, B., Christ-Roberts, C.Y., Kim, R.Y., Ramos, F.J., Kikani, C.K., Li, C., Deng, C., Reyna, S., Musi, N.*, et al.* (2007). Peripheral disruption of the Grb10 gene enhances insulin signaling and sensitivity in vivo. Mol Cell Biol *27*, 6497-6505.

Wang, Q., Sporns, O., and Burkhalter, A. (2012). Network analysis of corticocortical connections reveals ventral and dorsal processing streams in mouse visual cortex. J Neurosci *32*, 4386-4399.

Wang, X., Soloway, P.D., and Clark, A.G. (2010). Paternally biased X inactivation in mouse neonatal brain. Genome Biol *11*, R79.

Warden, M.R., Selimbeyoglu, A., Mirzabekov, J.J., Lo, M., Thompson, K.R., Kim, S.Y., Adhikari, A., Tye, K.M., Frank, L.M., and Deisseroth, K. (2012). A prefrontal cortex-brainstem neuronal projection that controls response to behavioural challenge. Nature *492*, 428-432.

Weaving, L.S., Ellaway, C.J., Gecz, J., and Christodoulou, J. (2005). Rett syndrome: clinical review and genetic update. J Med Genet *42*, 1-7.

Wilkinson, L.S., Davies, W., and Isles, A.R. (2007). Genomic imprinting effects on brain development and function. Nat Rev Neurosci *8*, 832-843.

Williams, R.W., and Rakic, P. (1988). Three-dimensional counting: an accurate and direct method to estimate numbers of cells in sectioned material. J Comp Neurol *278*, 344-352.

Williams, T.A., Langdon, R., and Porter, M.A. (2013). Hyper-reactivity in fragile X syndrome females: generalised or specific to socially-salient stimuli? A skin conductance study. Int J Psychophysiol *88*, 26-34.

Williams, T.A., Porter, M.A., and Langdon, R. (2014). Social approach and emotion recognition in fragile X syndrome. Am J Intellect Dev Disabil *119*, 133-150.

Winchester, B., Young, E., Geddes, S., Genet, S., Hurst, J., Middleton-Price, H., Williams, N., Webb, M., Habel, A., and Malcolm, S. (1992). Female twin with Hunter disease due to nonrandom inactivation of the X-chromosome: a consequence of twinning. Am J Med Genet *44*, 834-838.

Wu, H., Luo, J., Yu, H., Rattner, A., Mo, A., Wang, Y., Smallwood, P.M., Erlanger, B., Wheelan, S.J., and Nathans, J. (2014). Cellular resolution maps of X chromosome inactivation: implications for neural development, function, and disease. Neuron *81*, 103-119.

Yamasaki-Ishizaki, Y., Kayashima, T., Mapendano, C.K., Soejima, H., Ohta, T., Masuzaki, H., Kinoshita, A., Urano, T., Yoshiura, K., Matsumoto, N.*, et al.* (2007).

Role of DNA methylation and histone H3 lysine 27 methylation in tissue-specific imprinting of mouse Grb10. Mol Cell Biol *27*, 732-742.

Yang, C.F., Chiang, M.C., Gray, D.C., Prabhakaran, M., Alvarado, M., Juntti, S.A., Unger, E.K., Wells, J.A., and Shah, N.M. (2013). Sexually dimorphic neurons in the ventromedial hypothalamus govern mating in both sexes and aggression in males. Cell *153*, 896-909.

Yang, H., Yang, J., Xi, W., Hao, S., Luo, B., He, X., Zhu, L., Lou, H., Yu, Y.Q., Xu, F.*, et al.* (2016). Laterodorsal tegmentum interneuron subtypes oppositely regulate olfactory cue-induced innate fear. Nat Neurosci *19*, 283-289.

Zeesman, S., Zwaigenbaum, L., Whelan, D.T., Hagerman, R.J., Tassone, F., and Taylor, S.A. (2004). Paternal transmission of fragile X syndrome. Am J Med Genet A *129A*, 184-189.

Zhao, J., Ohsumi, T.K., Kung, J.T., Ogawa, Y., Grau, D.J., Sarma, K., Song, J.J., Kingston, R.E., Borowsky, M., and Lee, J.T. (2010). Genome-wide identification of polycomb-associated RNAs by RIP-seq. Mol Cell *40*, 939-953.

Zhao, J., Sun, B.K., Erwin, J.A., Song, J.J., and Lee, J.T. (2008). Polycomb proteins targeted by a short repeat RNA to the mouse X chromosome. Science *322*, 750-756.

Zingg, B., Chou, X.L., Zhang, Z.G., Mesik, L., Liang, F., Tao, H.W., and Zhang, L.I. (2017). AAV-Mediated Anterograde Transsynaptic Tagging: Mapping Corticocollicular Input-Defined Neural Pathways for Defense Behaviors. Neuron *93*, 33-47.